

Common Limitations of Image Processing Metrics: A Picture Story

ANNIKA REINKE*, German Cancer Research Center (DKFZ) Heidelberg, Division of Intelligent Medical Systems and HI Helmholtz Imaging, Germany and Faculty of Mathematics and Computer Science, Heidelberg University, Heidelberg, Germany

MINU D. TIZABI†, German Cancer Research Center (DKFZ) Heidelberg, Division of Intelligent Medical Systems, Germany and National Center for Tumor Diseases (NCT), NCT Heidelberg, a partnership between DKFZ and University Medical Center Heidelberg, Germany

CAROLE H. SUDRE, MRC Unit for Lifelong Health and Ageing at UCL and Centre for Medical Image Computing, Department of Computer Science, University College London, London, UK and School of Biomedical Engineering and Imaging Science, King's College London, London, UK

MATTHIAS EISENMANN, German Cancer Research Center (DKFZ) Heidelberg, Division of Intelligent Medical Systems, Germany

TIM RÄDSCH, German Cancer Research Center (DKFZ) Heidelberg, Division of Intelligent Medical Systems and HI Helmholtz Imaging, Germany

MICHAEL BAUMGARTNER, German Cancer Research Center (DKFZ) Heidelberg, Division of Medical Image Computing, Germany

LAURA ACION, Instituto de Cálculo, CONICET – Universidad de Buenos Aires, Buenos Aires, Argentina

MICHELA ANTONELLI, School of Biomedical Engineering and Imaging Science, King's College London, London, UK and Centre for Medical Image Computing, University College London, London, UK

TAL ARBEL, Centre for Intelligent Machines and MILA (Québec Artificial Intelligence Institute), McGill University, Montréal, Canada

SPYRIDON BAKAS, Division of Computational Pathology, Dept of Pathology & Laboratory Medicine, Indiana University School of Medicine, IU Health Information and Translational Sciences Building, Indianapolis, USA and Center for Biomedical Image Computing and Analytics (CBICA), University of Pennsylvania, Richards Medical Research Laboratories FL7, Philadelphia, PA, USA

PETER BANKHEAD, Institute of Genetics and Cancer, University of Edinburgh, Edinburgh, UK

ARRIEL BENIS, Department of Digital Medical Technologies, Holon Institute of Technology, Holon, Israel and European Federation for Medical Informatics, Le Mont-sur-Lausanne, Switzerland

MATTHEW BLASCHKO, Center for Processing Speech and Images, Department of Electrical Engineering, KU Leuven, Kasteelpark Arenberg 10 - box 2441, 3001 Leuven, Belgium

FLORIAN BUETTNER, German Cancer Consortium (DKTK), partner site Frankfurt/Mainz, a partnership between DKFZ and UCT Frankfurt-Marburg, Germany, German Cancer Research Center (DKFZ) Heidelberg, Germany, Goethe University Frankfurt, Department of Medicine, Germany, Goethe University Frankfurt, Department of Informatics, Germany, and Frankfurt Cancer Institute, Germany

M. JORGE CARDOSO, School of Biomedical Engineering and Imaging Science, King's College London, London, UK

JIANXU CHEN, Leibniz-Institut für Analytische Wissenschaften – ISAS – e.V., Dortmund, Germany

VERONIKA CHEPLYGINA, Department of Computer Science, IT University of Copenhagen, Copenhagen, Denmark

EVANGELIA CHRISTODOULOU, German Cancer Research Center (DKFZ) Heidelberg, Division of Intelligent Medical Systems, Germany

BETH A. CIMINI, Imaging Platform, Broad Institute of MIT and Harvard, Cambridge, MA, USA

GARY S. COLLINS, Centre for Statistics in Medicine, University of Oxford, Oxford, UK

SANDY ENGELHARDT, Department of Internal Medicine III and Department of Cardiac Surgery, Heidelberg University Hospital, Heidelberg, Germany

KEYVAN FARAHANI, Center for Biomedical Informatics and Information Technology, National Cancer Institute, Bethesda, MD, USA

LUCIANA FERRER, Instituto de Investigación en Ciencias de la Computación (ICC), CONICET-UBA, Ciudad Universitaria, Ciudad Autónoma de Buenos Aires, Argentina

ADRIAN GALDRAN, Universitat Pompeu Fabra, Barcelona, Spain and University of Adelaide, Adelaide, Australia

BRAM VAN GINNEKEN, Fraunhofer MEVIS, Bremen, Germany and Radboud Institute for Health Sciences, Radboud University Medical Center, Nijmegen, The Netherlands

BEN GLOCKER, Department of Computing, Imperial College London, London, UK

PATRICK GODAU, German Cancer Research Center (DKFZ) Heidelberg, Division of Intelligent Medical Systems, Germany, Faculty of Mathematics and Computer Science, Heidelberg University, Heidelberg, Germany, and National Center for Tumor Diseases (NCT), NCT Heidelberg, a partnership between DKFZ and University Medical Center Heidelberg, Germany

ROBERT HAASE, Now with: Center for Scalable Data Analytics and Artificial Intelligence (ScaDS.AI), Leipzig University, Leipzig, Germany, Technische Universität (TU) Dresden, DFG Cluster of Excellence "Physics of Life", Dresden, Germany, and Center for Systems Biology, Dresden, Germany

FRED HAMPRECHT, Heidelberg Collaboratory for Image Processing (HCI), Interdisciplinary Center for Scientific Computing (IWR) Heidelberg University, Heidelberg, Germany

DANIEL A. HASHIMOTO, Department of Surgery, Perelman School of Medicine, Philadelphia, PA, USA and General Robotics Automation Sensing and Perception Laboratory, School of Engineering and Applied Science, University of Pennsylvania, Philadelphia, PA, USA

DOREEN HECKMANN-NÖTZEL, German Cancer Research Center (DKFZ) Heidelberg, Division of Intelligent Medical Systems, Germany and National Center for Tumor Diseases (NCT), NCT Heidelberg, a partnership between DKFZ and University Medical Center Heidelberg, Germany

PETER HIRSCH, Max-Delbrück Center for Molecular Medicine, Regensburg, Germany

MICHAEL M. HOFFMAN, Princess Margaret Cancer Centre, University Health Network, Toronto, Canada, Department of Medical Biophysics, University of Toronto, Toronto, Canada, Department of Computer Science, University of Toronto, Toronto, Canada, and Vector Institute for Artificial Intelligence, Toronto, Canada

MEREL HUISMAN, Department of Radiology and Nuclear Medicine, Radboud University Medical Center, Nijmegen, The Netherlands

FABIAN ISENSEE, German Cancer Research Center (DKFZ) Heidelberg, Division of Medical Image Computing and HI Applied Computer Vision Lab, Germany

PIERRE JANNIN, Laboratoire Traitement du Signal et de l'Image – UMR_S 1099, Université de Rennes 1, Rennes, France and INSERM, Paris Cedex, France

CHARLES E. KAHN, Department of Radiology and Institute for Biomedical Informatics, University of Pennsylvania, Philadelphia, PA, USA

DAGMAR KAINMUELLER, Max-Delbrück Center for Molecular Medicine in the Helmholtz Association (MDC), Biomedical Image Analysis and HI Helmholtz Imaging, Berlin, Germany and University of Potsdam, Digital Engineering Faculty, Potsdam, Germany

BERNHARD KAINZ, Department of Computing, Faculty of Engineering, Imperial College London, London, UK and Department AIBE, Friedrich-Alexander-Universität (FAU), Erlangen-Nürnberg, Germany

ALEXANDROS KARARGYRIS, IHU Strasbourg, Strasbourg, France

ALAN KARTHIKESALINGAM, Google Health DeepMind, London, UK

A. EMRE KAVUR, German Cancer Research Center (DKFZ) Heidelberg, Division of Intelligent Medical Systems, Division of Medical Image Computing, HI Applied Computer Vision Lab, Germany

HANNES KENNGOTT, Department of General, Visceral and Transplantation Surgery, Heidelberg University Hospital, Heidelberg, Germany

JENS KLEESIEK, Institute for AI in Medicine, University Medicine Essen, Essen, Germany

ANDREAS KLEPPE, Institute for Cancer Genetics and Informatics, Oslo University Hospital, Oslo, Norway and Department of Informatics, University of Oslo, Oslo, Norway

SVEN KOEHLER, Department of Internal Medicine III and Department of Cardiac Surgery, Heidelberg University Hospital, Heidelberg, Germany

FLORIAN KOFLER, Helmholtz AI, München, Germany

ANNETTE KOPP-SCHNEIDER, German Cancer Research Center (DKFZ) Heidelberg, Division of Biostatistics, Germany

THIJS KOOI, Lunit Inc, Seoul, South Korea

MICHAL KOZUBEK, Centre for Biomedical Image Analysis and Faculty of Informatics, Masaryk University, Brno, Czech Republic

ANNA KRESHUK, Cell Biology and Biophysics Unit, European Molecular Biology Laboratory (EMBL), Heidelberg, Germany

TAHSIN KURC, Department of Biomedical Informatics, Stony Brook University, Stony Brook, NY, USA
BENNETT A. LANDMAN, Electrical Engineering, Vanderbilt University, Nashville, TN, USA
GEERT LITJENS, Department of Pathology, Radboud University Medical Center, Nijmegen, The Netherlands
AMIN MADANI, Department of Surgery, University Health Network, Philadelphia, PA, Canada
KLAUS MAIER-HEIN, German Cancer Research Center (DKFZ) Heidelberg, Division of Medical Image Computing and HI Helmholtz Imaging, Germany and Pattern Analysis and Learning Group, Department of Radiation Oncology, Heidelberg University Hospital, Heidelberg, Germany
ANNE L. MARTEL, Physical Sciences, Sunnybrook Research Institute, Toronto, Canada and Department of Medical Biophysics, University of Toronto, Toronto, Canada
PETER MATTSON, Google, Mountain View, CA 94043, USA
ERIK MEIJERING, School of Computer Science and Engineering, University of New South Wales, Sydney, Kensington, Australia
BJOERN MENZE, Department of Quantitative Biomedicine, University of Zurich, Zurich, Switzerland
DAVID MOHER, Centre for Journalology, Clinical Epidemiology Program, Ottawa Hospital Research Institute, Ottawa, Canada and School of Epidemiology and Public Health, Faculty of Medicine, University of Ottawa, Ottawa, Canada
KAREL G.M. MOONS, Julius Center for Health Sciences and Primary Care, UMC Utrecht, Utrecht University, Utrecht, The Netherlands
HENNING MÜLLER, Information Systems Institute, University of Applied Sciences Western Switzerland (HES-SO), Sierre, Switzerland and Medical Faculty, University of Geneva, Geneva, Switzerland
BRENNAN NICHYPORUK, MILA (Québec Artificial Intelligence Institute), Montréal, Canada
FELIX NICKEL, Department of General, Visceral and Thoracic Surgery, University Medical Center Hamburg-Eppendorf, Hamburg, Germany
M. ALICAN NOYAN, Ipsium, Eindhoven, The Netherlands
JENS PETERSEN, German Cancer Research Center (DKFZ) Heidelberg, Division of Medical Image Computing, Germany
GORKEM POLAT, Graduate School of Informatics, Middle East Technical University, Ankara, Turkey
SUSANNE M. RAFELSKI, Allen Institute for Cell Science, Seattle, WA, USA
NASIR RAJPOOT, Tissue Image Analytics Laboratory, Department of Computer Science, University of Warwick, Coventry, UK
MAURICIO REYES, ARTORG Center for Biomedical Engineering Research, University of Bern, Bern, Switzerland and Department of Radiation Oncology, University Hospital Bern, University of Bern, Bern, Switzerland
NICOLA RIEKE, NVIDIA GmbH, München, Germany
MICHAEL A. RIEGLER, Simula Metropolitan Center for Digital Engineering, Oslo, Norway and UiT The Arctic University of Norway, Tromsø, Norway
HASSAN RIVAZ, Department of Electrical and Computer Engineering, Concordia University, Montreal, Canada
JULIO SAEZ-RODRIGUEZ, Institute for Computational Biomedicine, Heidelberg University, Heidelberg, Germany and Faculty of Medicine, Heidelberg University Hospital, Heidelberg, Germany
CLARA I. SÁNCHEZ, Informatics Institute, Faculty of Science, University of Amsterdam, Amsterdam, The Netherlands
JULIEN SCHROETER, Centre for Intelligent Machines, McGill University, Montreal, Canada
ANINDO SAHA, Diagnostic Image Analysis Group, Radboud University Medical Center, Nijmegen, The Netherlands
M. ALPER SELVER, Electrical and Electronics Engineering Dept, Dokuz Eylül University, Izmir, Turkey
LALITH SHARAN, Department of Internal Medicine III and Department of Cardiac Surgery, Heidelberg University Hospital, Germany
SHRAVYA SHETTY, Google Health, Google, Palo Alto, CA, USA
MAARTEN VAN SMEDEN, Julius Center for Health Sciences and Primary Care, University Medical Center Utrecht, Utrecht, The Netherlands
BRAM STIELTJES, Department of Radiology, University Hospital of Basel, Basel, Switzerland
RONALD M. SUMMERS, National Institutes of Health Clinical Center, Bethesda, MD, USA
ABDEL A. TAHA, Institute of Information Systems Engineering, TU Wien, Vienna, Austria
ALEKSEI TIULPIN, Research Unit of Health Sciences and Technology, Faculty of Medicine, University of Oulu, Oulu, Finland and Neurocenter Oulu, Oulu University Hospital, Oulu, Finland
SOTIRIOS A. TSAFTARIS, School of Engineering, The University of Edinburgh, Edinburgh, Scotland

BEN VAN CALSTER, Department of Development and Regeneration and EPI-centre, KU Leuven, Leuven, Belgium and Department of Biomedical Data Sciences, Leiden University Medical Center, Leiden, The Netherlands

GAËL VAROQUAUX, Parietal project team, INRIA Saclay-Île de France, Palaiseau, France

MANUEL WIESENFARTH, German Cancer Research Center (DKFZ) Heidelberg, Division of Biostatistics, Germany

ZIV R. YANIV, Bethesda, Maryland, USA

PAUL JÄGER, German Cancer Research Center (DKFZ) Heidelberg, Interactive Machine Learning Group and HI Helmholtz Imaging, Germany

LENA MAIER-HEIN, German Cancer Research Center (DKFZ) Heidelberg, Division of Intelligent Medical Systems and HI Helmholtz Imaging, Germany, Faculty of Mathematics and Computer Science and Medical Faculty, Heidelberg University, Heidelberg, Germany, and National Center for Tumor Diseases (NCT), NCT Heidelberg, a partnership between DKFZ and University Medical Center Heidelberg, Germany

Abstract: While the importance of automatic image analysis is continuously increasing, recent meta-research revealed major flaws with respect to algorithm validation. Performance metrics are particularly key for meaningful, objective, and transparent performance assessment and validation of the used automatic algorithms, but relatively little attention has been given to the practical pitfalls when using specific metrics for a given image analysis task. These are typically related to (1) the disregard of inherent metric properties, such as the behaviour in the presence of class imbalance or small target structures, (2) the disregard of inherent data set properties, such as the non-independence of the test cases, and (3) the disregard of the actual biomedical domain interest that the metrics should reflect. This living dynamically document has the purpose to illustrate important limitations of performance metrics commonly applied in the field of image analysis. In this context, it focuses on biomedical image analysis problems that can be phrased as image-level classification, semantic segmentation, instance segmentation, or object detection task. The current version is based on a Delphi process on metrics conducted by an international consortium of image analysis experts from more than 60 institutions worldwide.

Keywords: Good Scientific Practice, Validation, Metrics, Image Processing, Image Analysis, Segmentation, Classification, Detection, Medical Imaging

CONTENTS

1	Purpose	5
2	Fundamentals	11
2.1	Image-level Classification	13
2.2	Semantic Segmentation	21
2.3	Object Detection	28
2.4	Instance Segmentation	36
3	Pitfalls due to category-metric mismatch	41
4	Pitfalls related to image-level classification	46
5	Pitfalls related to segmentation	78
6	Pitfalls related to object detection	100
7	Pitfalls related to analyses and post-processing	121
8	Conclusion	132
9	Acknowledgements	132
A	Acronyms	137

*Shared first authors.

1 PURPOSE

Validation of biological and medical image analysis algorithms is of the utmost importance for making scientific progress and for translating methodological research into practice. Validation metrics¹, the measures according to which performance of algorithms is quantified, constitute a core component of validation design. While metrics can measure various quantities of interest, including speed, memory consumption or carbon footprint, most metrics applied today are *reference-based metrics*, which have the purpose of measuring the agreement of an algorithm prediction with a given reference. The reference, in turn, serves as an approximation of the (typically unknown) ground truth.

Knowing the properties of metrics in use and making educated choices is essential for meaningful and reliable validation in image analysis. Although several papers highlight specific strengths and weaknesses of common metrics [30, 49, 50, 58, 84], an international survey [56] revealed the choice of inappropriate metrics as one of the core problems related to performance assessment in medical image analysis. Similar problems are present in other imaging domains [19, 38]. Under the umbrella of Helmholtz Imaging (HI)², three international initiatives have now joined forces to address these issues: the Biomedical Image Analysis Challenges (BIAS) initiative³, the Medical Image Computing and Computer Assisted Interventions (MICCAI) Society's special interest group on challenges⁴, as well as the benchmarking working group of the MONAI framework⁵. A core mission is to provide researchers with guidelines and tools to choose the performance metrics in a problem- and context-aware manner. This dynamically updated document aims to illustrate important pitfalls and drawbacks of metrics commonly applied in the field of image analysis. The current version is based on a Delphi process on metrics conducted with an international consortium of medical image analysis experts. A Delphi process is a multi-stage survey process designed to pool the knowledge of several experts to arrive at a consensus decision [8].

The Delphi consortium focused on problems reporting biomedical research that can be phrased as **image-level classification**, **semantic segmentation**, **instance segmentation** or **object detection** (Figure 1). Essentially, these can all be interpreted as a classification task at different scales and thus share many aspects in terms of validation (Figure 2). For example, an object detection task can be interpreted as an object-/instance-level classification task, while a segmentation task can be interpreted as a pixel-level classification task. We will refer to these four different task types as *problem categories*. Please note that we will use the term "pixel" even for three-dimensional (or n-dimensional) images for increased readability instead of referring to "pixels/voxels". Most of the examples are shown for two-dimensional images and can be translated to the n-dimensional case.

The manuscript is structured as follows. As a foundation, we first review the most commonly applied metrics for the problem categories addressed in this paper (Sec. 2). Since a common problem in the biomedical image analysis community is the selection of metrics from the wrong problem category, Sec. 3 highlights pitfalls relevant in this context. The following sections then present pitfalls for image-level classification (Sec. 4), image segmentation, including semantic and instance segmentation (Sec. 5), and object detection, including instance segmentation (Sec. 6). Finally, cross-topic pitfalls are highlighted (Sec. 7). An overview of all figures is presented in Table 1.

¹not to be confused with distance metrics in the strict mathematical sense

²<https://www.helmholtz-imaging.de/>

³<https://www.dkfz.de/en/cami/research/topics/biasInitiative.html>

⁴<https://miccai.org/index.php/special-interest-groups/challenges/>

⁵<https://monai.io/>

Problem categories addressed by this paper

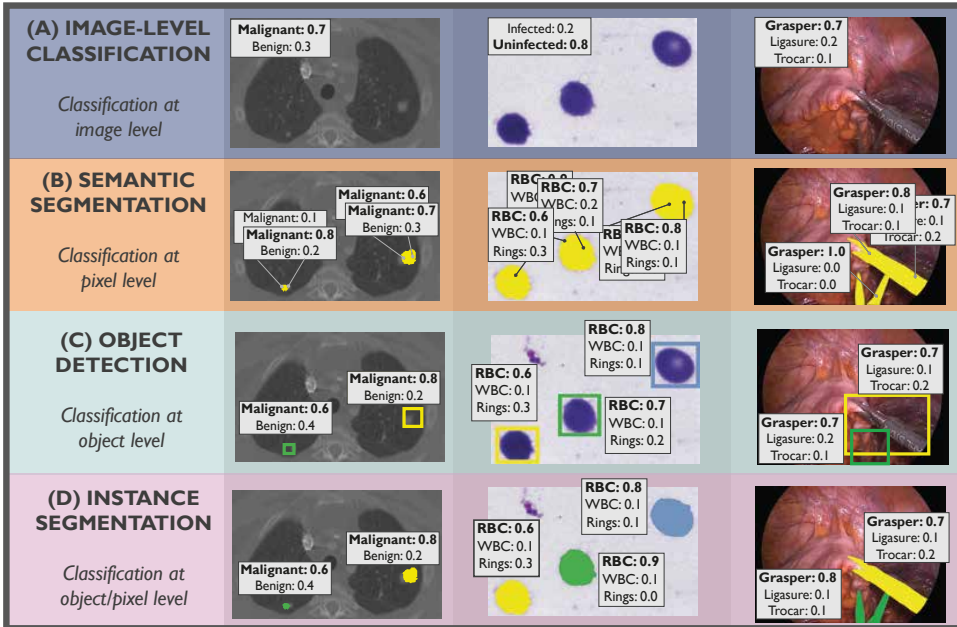


Fig. 1. Problem categories covered in this paper and illustrated for three different application domains: radiology (left), cell biology (middle), surgery (right). The common denominator of the underlying research problems is the fact that they can be interpreted as classification tasks. The classification occurs at various scales, image level, object level and/or pixel level. Each of these tasks assigns a class label to the image or (multiple) components of it. (A) The **image-level classification** task involves assigning a class label to the whole image. (B) The **semantic segmentation** task involves assigning a class label to each individual pixel. (C) The **object detection** task assigns a class label to identified objects. (D) The **instance segmentation** task assigns a label to identified objects made up of multiple pixels. Gray boxes show the predicted class probabilities on image level, pixel level or object level. The class with the highest probability is shown in bold. Further abbreviations: Red Blood Cell (RBC), White Blood Cell (WBC).

Table 1. Overview of figures on pitfalls related to metrics classified into (1) pitfalls due to category-metric mismatch, (2) category-specific pitfalls and (3) cross-topic pitfalls. For each illustration, the corresponding figure and page number is given. Please note that the pitfalls are typically illustrated for only one or two problem categories but often also apply to other problem categories, as indicated in the table.

Source of potential pitfall	Figure(s)
<i>Pitfalls due to category-metric mismatch</i>	
Mismatch: Semantic segmentation ↔ object detection	Fig. 21 (Page 41)
Mismatch: Semantic ↔ instance segmentation	Fig. 22 (Page 42)
Mismatch: Image-level classification ↔ object detection	Fig. 23 (Page 44)
No matching problem category	Fig. 24 (Page 45)
<i>Pitfalls in image-level classification</i>	
High class imbalance	Fig. 25 (Page 48) Fig. 26 (Page 49) Fig. 27 (Page 50)
More than two classes available	Fig. 28 (Page 51)
Unequal importance of class confusions	Fig. 29 (Page 52)
Unequal importance of classes	Fig. 30 (Page 53)
Interdependencies between classes	Fig. 31 (Page 54)
Stratification based on meta-information	Fig. 32 (Page 55)
Importance of cost-benefit analysis	Fig. 33 (Page 57)
Definition of class labels	Fig. 34 (Page 58)
Prevalence dependency	Fig. 35 (Page 59) Fig. 36 (Page 60) Fig. 37 (Page 62)
Importance of confidence awareness	Fig. 38 (Page 63) Fig. 39 (Page 64) Fig. 40 (Page 65) Fig. 41 (Page 66)
Presence of ordinal classes	Fig. 42 (Page 67) Fig. 43 (Page 68)
Same metric scores for different confusion matrices	Fig. 44 (Page 70)
Upper and lower bounds not equally obtainable	Fig. 45 (Page 72) Fig. 46 (Page 73)
Determination of a global threshold for all classes	Fig. 47 (Page 74)
Model bias	Fig. 48 (Page 76)
Small sample sizes	Fig. 49 (Page 77)
Multi-threshold metric-related properties (<i>here: pitfalls illustrated for object detection problems</i>)	Fig. 79 (Page 116) Fig. 80 (Page 117) Fig. 81 (Page 118)
<i>Pitfalls in semantic segmentation</i>	
Small size of structures relative to pixel size	Fig. 50 (Page 80) Fig. 51 (Page 81)
(<i>here: pitfall illustrated for object detection problems</i>)	Fig. 74 (Page 109)
High variability of structure sizes	Fig. 52 (Page 82) Fig. 53 (Page 83)
Complex shape of structures	Fig. 54 (Page 84) Fig. 55 (Page 85) Fig. 56 (Page 86)

Particular importance of structure volume	Fig. 57 (Page 87)
Particular importance of structure center	Fig. 58 (Page 88)
Particular importance of structure boundaries	Fig. 59 (Page 90)
	Fig. 60 (Page 91)
<i>(here: pitfall illustrated for object detection problems)</i>	Fig. 74 (Page 109)
<i>(here: pitfall illustrated for object detection problems)</i>	Fig. 75 (Page 110)
Possibility of multiple labels per unit	Fig. 61 (Page 92)
Noisy reference standard	Fig. 62 (Page 93)
Possibility of outliers in reference annotation	Fig. 63 (Page 94)
Possibility of reference or prediction without target structure(s)	Fig. 64 (Page 96)
Dependency on image resolution	Fig. 65 (Page 97)
Over- vs. undersegmentation	Fig. 66 (Page 98)
Choice of global decision threshold	Fig. 67 (Page 99)
High class imbalance <i>(here: pitfall illustrated for image-level classification problems)</i>	Fig. 25 (Page 48)
	Fig. 26 (Page 49)
	Fig. 27 (Page 50)
More than two classes available <i>(here: pitfall illustrated for image-level classification problems)</i>	Fig. 28 (Page 51)
Unequal importance of class confusions <i>(here: pitfall illustrated for image-level classification problems)</i>	Fig. 29 (Page 52)
Unequal importance of classes <i>(here: pitfall illustrated for image-level classification problems)</i>	Fig. 30 (Page 53)
Interdependencies between classes <i>(here: pitfall illustrated for image-level classification problems)</i>	Fig. 31 (Page 54)

Pitfalls in object detection

Mathematical implications of center-based localization criteria	Fig. 68 (Page 101)
	Fig. 69 (Page 102)
Mathematical implications of <i>IoU</i> -based localization criterion	Fig. 70 (Page 104)
Mathematical implications of the choice of assignment strategies	Fig. 71 (Page 106)
	Fig. 72 (Page 107)
Type of the provided annotations	Fig. 73 (Page 108)
Effect of small structures on localization criterion	Fig. 74 (Page 109)
<i>(here: pitfall illustrated for semantic segmentation problems)</i>	Fig. 50 (Page 80)
Perfect <i>Boundary IoU</i> for imperfect prediction	Fig. 75 (Page 110)
Possibility of reference or prediction without target structure(s)	Fig. 76 (Page 112)
<i>(here: pitfall illustrated for semantic segmentation problems)</i>	Fig. 64 (Page 96)
<i>Average Precision vs. Free-response ROC score</i>	Fig. 77 (Page 113)
<i>Free-response ROC score</i> is not standardized	Fig. 78 (Page 114)
Multi-threshold metric-related properties	Fig. 79 (Page 116)
	Fig. 80 (Page 117)
	Fig. 81 (Page 118)
High class imbalance <i>(here: pitfall illustrated for image-level classification problems)</i>	Fig. 25 (Page 48)
	Fig. 26 (Page 49)
	Fig. 27 (Page 50)
More than two classes available <i>(here: pitfall illustrated for image-level classification problems)</i>	Fig. 28 (Page 51)
Unequal importance of class confusions <i>(here: pitfall illustrated for image-level classification problems)</i>	Fig. 29 (Page 52)
Unequal importance of classes <i>(here: pitfall illustrated for image-level classification problems)</i>	Fig. 30 (Page 53)
Interdependencies between classes <i>(here: pitfall illustrated for image-level classification problems)</i>	Fig. 31 (Page 54)
Particular importance of structure center <i>(here: pitfall illustrated for semantic segmentation problems)</i>	Fig. 58 (Page 88)
High variability of structure sizes <i>(here: pitfall illustrated for semantic segmentation problems)</i>	Fig. 52 (Page 82)
<i>(here: pitfall illustrated for semantic segmentation problems)</i>	Fig. 53 (Page 83)
Complex shape of structures <i>(here: pitfall illustrated for semantic segmentation problems)</i>	Fig. 54 (Page 84)
	Fig. 55 (Page 85)
	Fig. 56 (Page 86)
Possibility of multiple labels per unit <i>(here: pitfall illustrated for semantic segmentation problems)</i>	Fig. 61 (Page 92)

Noisy reference standard (<i>here: pitfall illustrated for semantic segmentation problems</i>)	Fig. 62 (Page 93)
Possibility of outliers in reference annotation (<i>here: pitfall illustrated for semantic segmentation problems</i>)	Fig. 63 (Page 94)
Choice of global decision threshold (<i>here: pitfall illustrated for semantic segmentation problems</i>)	Fig. 67 (Page 99)
<i>Pitfalls in instance segmentation</i>	
Segmentation quality vs. detection quality	Fig. 19 (Page 39)
Small size of structures relative to pixel size	Fig. 50 (Page 80) Fig. 51 (Page 81) Fig. 74 (Page 109)
High variability of structure sizes	Fig. 52 (Page 82) Fig. 53 (Page 83)
Complex shape of structures	Fig. 54 (Page 84) Fig. 55 (Page 85) Fig. 56 (Page 86)
Particular importance of structure volume	Fig. 57 (Page 87)
Particular importance of structure center	Fig. 58 (Page 88)
Particular importance of structure boundaries	Fig. 74 (Page 109) Fig. 75 (Page 110) Fig. 59 (Page 90) Fig. 60 (Page 91)
Possibility of multiple labels per unit	Fig. 61 (Page 92)
Noisy reference standard	Fig. 62 (Page 93)
Possibility of outliers in reference annotation	Fig. 63 (Page 94)
Possibility of reference or prediction without target structure(s)	Fig. 64 (Page 96) Fig. 76 (Page 112)
Dependency on image resolution	Fig. 65 (Page 97)
Over- vs. undersegmentation	Fig. 66 (Page 98)
Choice of global decision threshold	Fig. 67 (Page 99)
Mathematical implications of center-based localization criteria	Fig. 68 (Page 101) Fig. 69 (Page 102)
Mathematical implications of <i>IoU</i> -based localization criterion	Fig. 70 (Page 104)
Mathematical implications of the choice of assignment strategies	Fig. 71 (Page 106) Fig. 72 (Page 107)
Effect of small structures on localization criterion	Fig. 74 (Page 109) Fig. 50 (Page 80)
Perfect <i>Boundary IoU</i> for imperfect prediction	Fig. 75 (Page 110)
<i>Average Precision</i> vs. <i>Free-response ROC</i> score	Fig. 77 (Page 113)
<i>Free-response ROC</i> score is not standardized	Fig. 78 (Page 114)
Multi-threshold metric-related properties	Fig. 79 (Page 116) Fig. 80 (Page 117) Fig. 81 (Page 118)
High class imbalance (<i>here: pitfall illustrated for image-level classification problems</i>)	Fig. 25 (Page 48) Fig. 26 (Page 49) Fig. 27 (Page 50)
More than two classes available (<i>here: pitfall illustrated for image-level classification problems</i>)	Fig. 28 (Page 51)
Unequal importance of class confusions (<i>here: pitfall illustrated for image-level classification problems</i>)	Fig. 29 (Page 52)
Unequal importance of classes (<i>here: pitfall illustrated for image-level classification problems</i>)	Fig. 30 (Page 53)
Interdependencies between classes (<i>here: pitfall illustrated for image-level classification problems</i>)	Fig. 31 (Page 54)
<i>Cross-topic pitfalls</i>	
Uninformative visualization	Fig. 83 (Page 122)

Metric aggregation for invalid algorithm output (e.g. NaNs)	Fig. 84 (Page 123)
	Fig. 85 (Page 124)
Hierarchical data aggregation	Fig. 86 (Page 125)
Aggregation per class	Fig. 87 (Page 126)
Metric combination	Fig. 88 (Page 127)
Ranking uncertainty	Fig. 89 (Page 129)
Insufficient biomedical relevance of metric score differences	Fig. 90 (Page 130)
Non-determinism of algorithms	Fig. 91 (Page 131)

2 FUNDAMENTALS

The present work focuses on biomedical image analysis problems that can be interpreted as a classification task at image, object or pixel level. The vast majority of metrics for these problem categories is directly or indirectly based on epidemiological principles of True Positive (TP), False Negative (FN), False Positive (FP), True Negative (TN), i.e. the *cardinalities* of the so-called confusion matrix, depicted in Figure 2. The TP/FN/FP/TN, from now on referred to as cardinalities. In the case of more than two classes C we also refer to the entries of the $C \times C$ confusion matrix as cardinalities. For simplicity and clarity in notation, we restrict ourselves to the binary case in most examples. Cardinalities can be computed for image (segment), object or pixel level. They are typically computed by comparing the prediction of the algorithm to a reference annotation. Modern neural network-based approaches typically require a threshold to be set in order to convert the algorithm output comprising predicted class scores (also referred to as continuous class scores) to a confusion matrix, as illustrated in Figure 2. For the purpose of metric recommendation, the available metrics can be broadly classified as follows (see also [11]):

- **Counting metrics** operate directly on the confusion matrix and express the metric value as a function of the cardinalities (see Figs. 4, 5 and 7). In the context of segmentation, they have typically been referred to as **overlap-based** metrics [81]. We distinguish **multi-class counting metrics**, which are defined for an arbitrary number of classes, from **per-class counting metrics**, which are computed by treating one class as foreground/positive class and all other classes as background. Popular examples for the former include *Matthews Correlation Coefficient (MCC)*, *Accuracy*, and *Cohen's Kappa κ* , while examples for the latter are *Sensitivity*, *Specificity*, *Positive Predictive Value (PPV)*, *Dice Similarity Coefficient (DSC)* and *Intersection over Union (IoU)*.
- **Multi-threshold metrics** operate on a dynamic confusion matrix, reflecting the conflicting properties of interest, such as high *Sensitivity* and high *Specificity*. Popular examples include the *Area under the Receiver Operating Characteristic curve (AUROC)* (see Figure 6) and *Average Precision (AP)* (see Figure 15).
- **Distance-based metrics** have been designed for semantic and instance segmentation tasks. They operate exclusively on the TP and rely on the explicit definition of object boundaries (see Figs. 8 and 10). Popular examples are the *Hausdorff Distance (HD)* and the *Normalized Surface Distance (NSD)* (see Figure 10).

Depending on the context (e.g. image-level classification vs. semantic segmentation task) and the community (e.g. medical imaging community vs. computer vision community), identical metrics are referred to with different terminology. For example, *Sensitivity*, *True Positive Rate (TPR)* and *Recall* refer to the same concept. The same holds true for the *DSC* and the *F₁ Score*. The most relevant metrics for the problem categories in the scope of this paper are introduced in the following.

Most metrics are recommended to be applied per class (except the multi-class counting metrics), meaning that a potential multi-class problem is converted to multiple binary classification problems, such that each relevant class serves as the positive class once. This results in different confusion matrices depending on which class is used as the positive class.

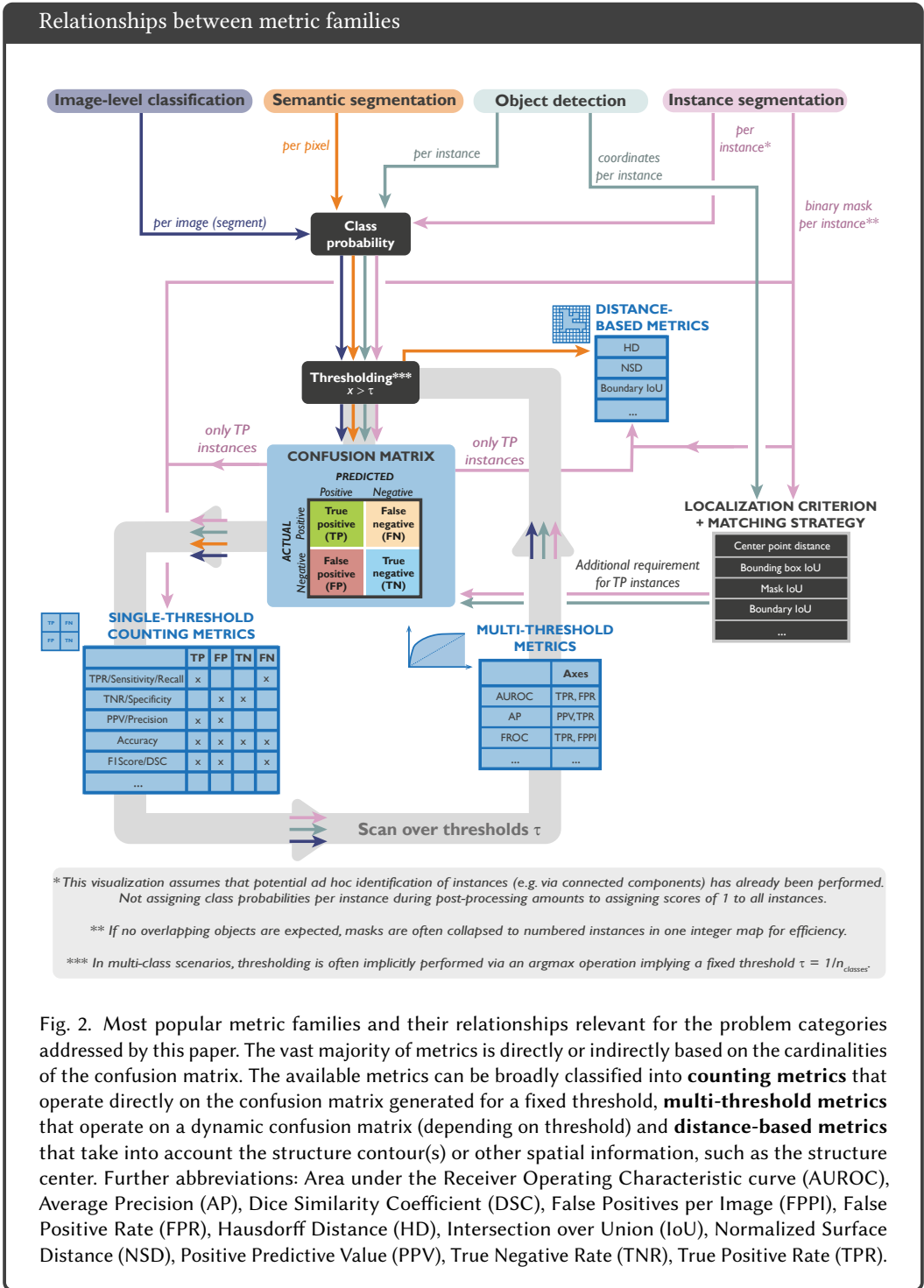


Fig. 2. Most popular metric families and their relationships relevant for the problem categories addressed by this paper. The vast majority of metrics is directly or indirectly based on the cardinalities of the confusion matrix. The available metrics can be broadly classified into **counting metrics** that operate directly on the confusion matrix generated for a fixed threshold, **multi-threshold metrics** that operate on a dynamic confusion matrix (depending on threshold) and **distance-based metrics** that take into account the structure contour(s) or other spatial information, such as the structure center. Further abbreviations: Area under the Receiver Operating Characteristic curve (AUROC), Average Precision (AP), Dice Similarity Coefficient (DSC), False Positives per Image (FPPI), False Positive Rate (FPR), Hausdorff Distance (HD), Intersection over Union (IoU), Normalized Surface Distance (NSD), Positive Predictive Value (PPV), True Negative Rate (TNR), True Positive Rate (TPR).

2.1 Image-level Classification

Image-level classification refers to the process of assigning one or multiple labels, or *classes*, to an image. If there is only one class of interest (e.g. cancer vs. no cancer), we speak of *binary classification*, otherwise of *categorical classification*. Modern algorithms usually output **predicted class probabilities** (or continuous class scores) between 0 and 1 for every image and class, indicating the probability of the image belonging to a specific class. By introducing a threshold (e.g. 0.5), predictions are considered as positive (e.g. cancer = true) if they are above the threshold or negative if they are below the threshold. Afterwards, predictions are assigned to the cardinalities (e.g. a cancer patient with prediction cancer = true is considered as TP) [20]. The most popular classification metrics are counting metrics, operating on a confusion matrix with fixed threshold on the class probabilities, and multi-threshold metrics, as detailed in the following.

Counting metrics. The most common binary counting metrics used for image-level classification are presented in Figs. 4 (per-class) and 5 (multi-class). Please note that these metrics are also commonly used in segmentation and object detection tasks. For segmentation tasks, they are often referred to as overlap-based metrics. Each of the presented metrics covers specific properties.

The *Sensitivity* (also referred to as *Recall*, *TPR* or *Hit rate*) focuses on the actual positives (TP and FN) and represents the fraction of positives that were correctly detected as such. In contrast, *PPV* (or *Precision*) divides the TP by the total number of predicted positive cases, thus aiming to represent the probability of a positive prediction corresponding to an actual positive. A value of 1 would imply that all positive predicted cases are actually positives, but it might still be the case that positive cases were missed. Please note that the term *Precision* has multiple meanings. In the context of computer assisted interventions, for example, it typically refers to the measured variance. Hence, the usage of its synonym *PPV* may be preferred.

In analogy to the *Sensitivity* for positives, *Specificity* (also referred to as *Selectivity* or *TNR*) focuses on the negative cases by computing the fraction of negatives that were correctly detected as such. Similarly to the *PPV*, the *Negative Predictive Value (NPV)* divides the TN by the total number of predicted negative cases and measures how many of the predicted negative samples were actually negative. *Specificity* and *NPV* require the definition of TN cases, which is not always possible. In object detection tasks, for example (see Sec. 2.3), TN are typically ill-defined and not provided. Therefore, these measures can not be computed in those cases.

PPV and *NPV* provide quantities of direct interest to the medical practitioner, namely the probability of a certain event given the prediction of the classifier. However, unlike *Sensitivity* and *Specificity*, they are not only functions of the classifier but also of the study population. Hence, one cannot extrapolate from one population to another, e.g. from a case-control study to the general population without correcting for prevalence. In the case of the prevalence being unequal to 0.5, prevalence correction should be applied (see Figure 35):

$$PPV = \frac{Sensitivity \cdot Prevalence}{Sensitivity \cdot Prevalence + (1 - Specificity) \cdot (1 - Prevalence)} \quad (1)$$

$$NPV = \frac{Specificity \cdot (1 - Prevalence)}{Specificity \cdot (1 - Prevalence) + (1 - Sensitivity) \cdot Prevalence} \quad (2)$$

As illustrated in Figure 25, reporting of a single metric such as *Sensitivity*, *PPV* or *Specificity* can be highly misleading because, for example, non-informative classifiers can achieve high values on imbalanced classes. The F_1 Score (also known as *DSC* in the context of segmentation), overcomes

this issue by representing the harmonic mean of *PPV* and *Sensitivity* and therefore penalizing extreme values of either metric [36], while being relatively robust against imbalanced data sets [80]. The F_1 Score is a specification of the $F\beta$ score, which adds a weighting between *PPV* and *Sensitivity*. For higher values of β , *Sensitivity* is given a higher weight over *PPV*, which might be desired depending on the application. More specifically, the $F\beta$ Score weights between FP and FN samples. Another metric which combines the metrics above is the Positive Likelihood Ratio (LR+), which is the ratio of the *Sensitivity* and $1 - \text{Specificity}$ (*FPR*). This metric is described as the "probability that a positive test would be expected in a patient divided by the probability that a positive test would be expected in a patient without a disease" [76]. It is defined as odds ratio and therefore invariant to the prevalence [77].

All of the metrics presented so far are bounded between 0 and 1 with 1 representing a perfect value and 0 the worst possible prediction of this metric. However, all of them rely on the definition of the positive class, which may be straightforward in some cases but can be based on a rather arbitrary choice in others. Notably, metric values may be completely different depending on the choice of positive class [70].

To overcome the need for selecting one class as the positive class, other metrics have been suggested that can be based on all entries of a *multi-class* confusion matrix, in which each class is assigned a row and a column of the matrix. The *Accuracy* is one of the most commonly used metrics and measures the ratio between all correct predictions (TP and TN) and the total number of samples. *Accuracy* is not robust against imbalanced data sets (see Figure 25), and is therefore often replaced by the more robust *Balanced Accuracy* (*BA*) that averages the *Sensitivity* over all classes [32]. For two classes, the metric averages *Sensitivity* and *Specificity*. An alternative is *Youden's Index J* or *Bookmaker Informedness* (*BM*), similarly summing up *Sensitivity* per class (or for two classes, summing up *Sensitivity* and *Specificity*). Note that *Youden's Index J* and *BA* are closely related and can directly be calculated from the other as $J = 2BA - 1$ and $BA = (J + 1)/2$. Both *BA* and *Youden's Index J* are invariant to the prevalence.

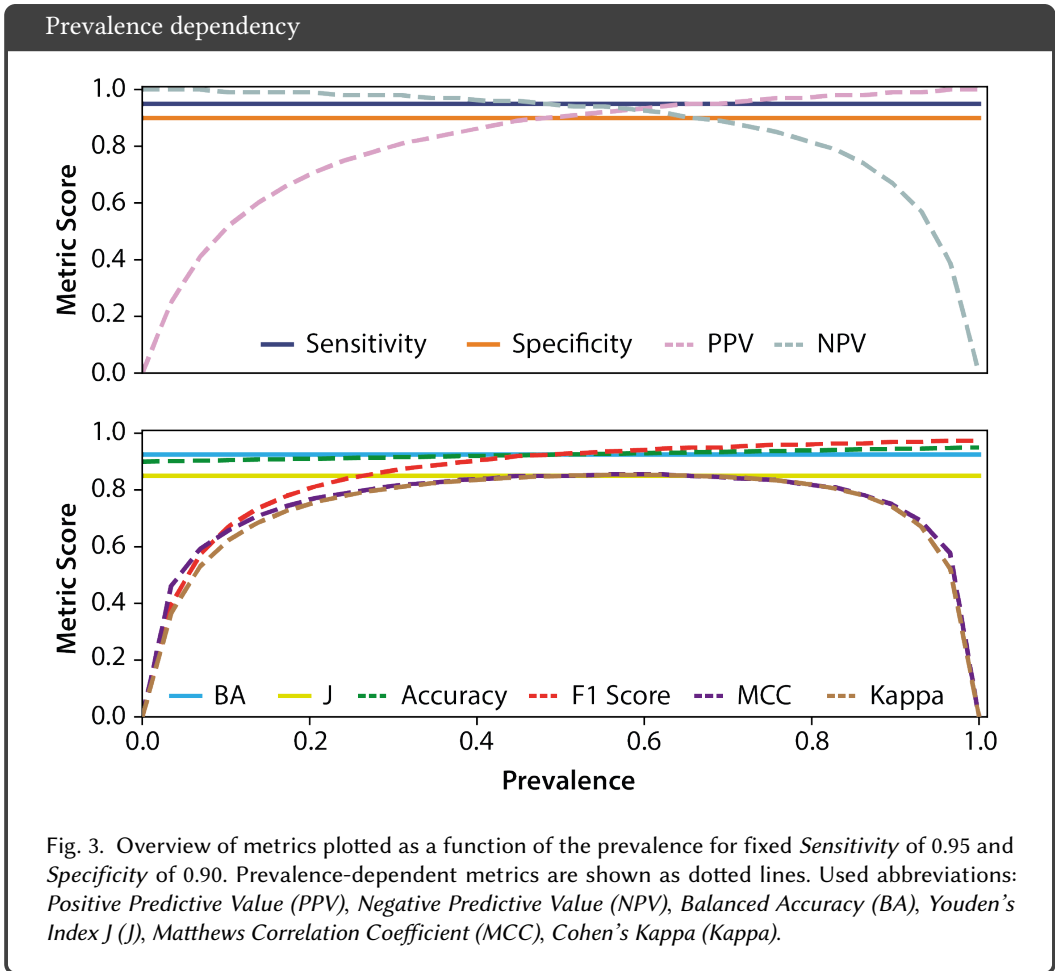
The *MCC*, also known as *Phi Coefficient*, measures the correlation between the actual and predicted class. The metric is bounded between -1 and 1, with high positive values referring to a good prediction which can only be achieved when all cardinalities are good, i.e. with a low number of FP/FN and high TP/TN. Another popular metric is *Cohen's Kappa* κ , which calculates the agreement between the reference and prediction while incorporating information on the agreement by chance. It is therefore a form of chance-corrected *Accuracy*. Similarly to *MCC*, it incorporates all values of the confusion matrix and is bounded between -1 and 1. In contrast to *MCC*, negative values do not indicate anti-correlation, but less agreement than expected by chance. *Cohen's Kappa* κ can be generalized by introducing a weighting scheme for the cardinalities in the *Weighted Cohen's Kappa* κ metric. For those three metrics, a value of 0 refers to a prediction which is not better than random guessing.

All of the presented binary counting metrics can be transferred to the multi-class case [32, 39], where *MCC* and (*Weighted*) *Cohen's Kappa* κ have explicit definitions, whereas the others become the implicit result of an aggregation across a rotating one-versus-the-rest binary perspective for each of the classes.

The *Expected Cost* (*EC*) is a generalization of the probability of error (which, in turn, is $1 - \text{Accuracy}$) for cases in which errors cannot all be considered to have equally severe consequences. It is defined as the expectation of the cost, where the cost incurred on a certain sample depends on the sample's class and the decision made for that sample. In practice, the expectation can be

estimated as a simple average of the costs over the validation samples. *EC* describes the weighted sum of error rates. It can also be used to measure discrimination and calibration in one score. A variant of *EC* normalizes *EC* by the *EC* of a naive system.

Many of the presented metrics depend on the prevalence. Figure 3 illustrates how their values change based on the prevalence.



Multi-threshold metrics. The classical counting metrics presented above rely on fixed thresholds to be set on the predicted class probabilities (if available), resulting in them being based on the cardinalities of the confusion matrix. **Multi-threshold metrics** overcome this limitation by calculating metric scores based on multiple thresholds. For instance, to emphasize how well a prediction distinguishes between the positive and negative class, the *AUROC* can be utilized. The *Receiver Operating Characteristic (ROC)* curve plots the *FPR*, which is equal to $1 - \textit{Specificity}$, against the *Sensitivity* for multiple thresholds of the predicted class probabilities, contrarily to just choosing one fixed threshold. For computation of the ROC curve, the class scores can be ordered in

descending order and each score regarded as a potential threshold. For each threshold, the resulting *Sensitivity* and *Specificity* are computed, and the resulting tuple is added to the *ROC* curve as one point (cf. Figure 6); note that the lower the threshold, the higher the *Sensitivity* but the lower (potentially) the *Specificity*. This leads to a monotonic increase of the curve. To interpolate between all points, i.e. to approximate the values between the calculated *Sensitivity* and *Specificity* tuples, a simple linear interpolation can be employed by drawing a line between each pair of points [20]. An optimal classifier would lead to *Sensitivity* and *Specificity* of 1 (1-*Specificity* of 0), therefore corresponding to a single point (0, 1) on the *ROC* curve. In contrast, a classifier with no skill level (random guessing) would result in a diagonal line from (0, 0) to (1, 1) (dashed line in Figure 6). The area under the *ROC* curve is referred to as *AUROC*, also called *AUC ROC* or simply *AUC*.

AUROC comes with two advantages: threshold and scale invariance. *AUROC* measures the quality of the predictions regardless of the threshold, as it is calculated over a number of thresholds. Furthermore, *AUROC* does not focus on the absolute values of predictions, but rather on how well they are ranked. However, those properties are not always desired. If a specific penalization of FP or FN is desired (cf. Figure 30), *AUROC* is not the best metric choice as it is invariant to the threshold. If the predicted class probabilities are intended to be well calibrated, the scale invariance feature will prevent from doing so.

Per definition, *AUROC* measures the complete area under the *ROC* curve. If only a specific range is of interest, a partial or ranged *AUROC* can also be computed [55]. Similarly, metrics can be assessed at a certain point of the *ROC* curve, for example the *Sensitivity* value at a specific score of the *Specificity* (e.g. 0.9), also referred to as *Sensitivity@Specificity*. This approach can similarly be used for other curve measures, e.g. the *Precision-Recall (PR)* curve, introduced in Sec. 2.3, and is illustrated in Figure 6. Please note that we will use the synonyms *Precision* instead of *PPV* and *Recall* instead of *Sensitivity* in the case of the *PR* curve, given the common use of these terms.

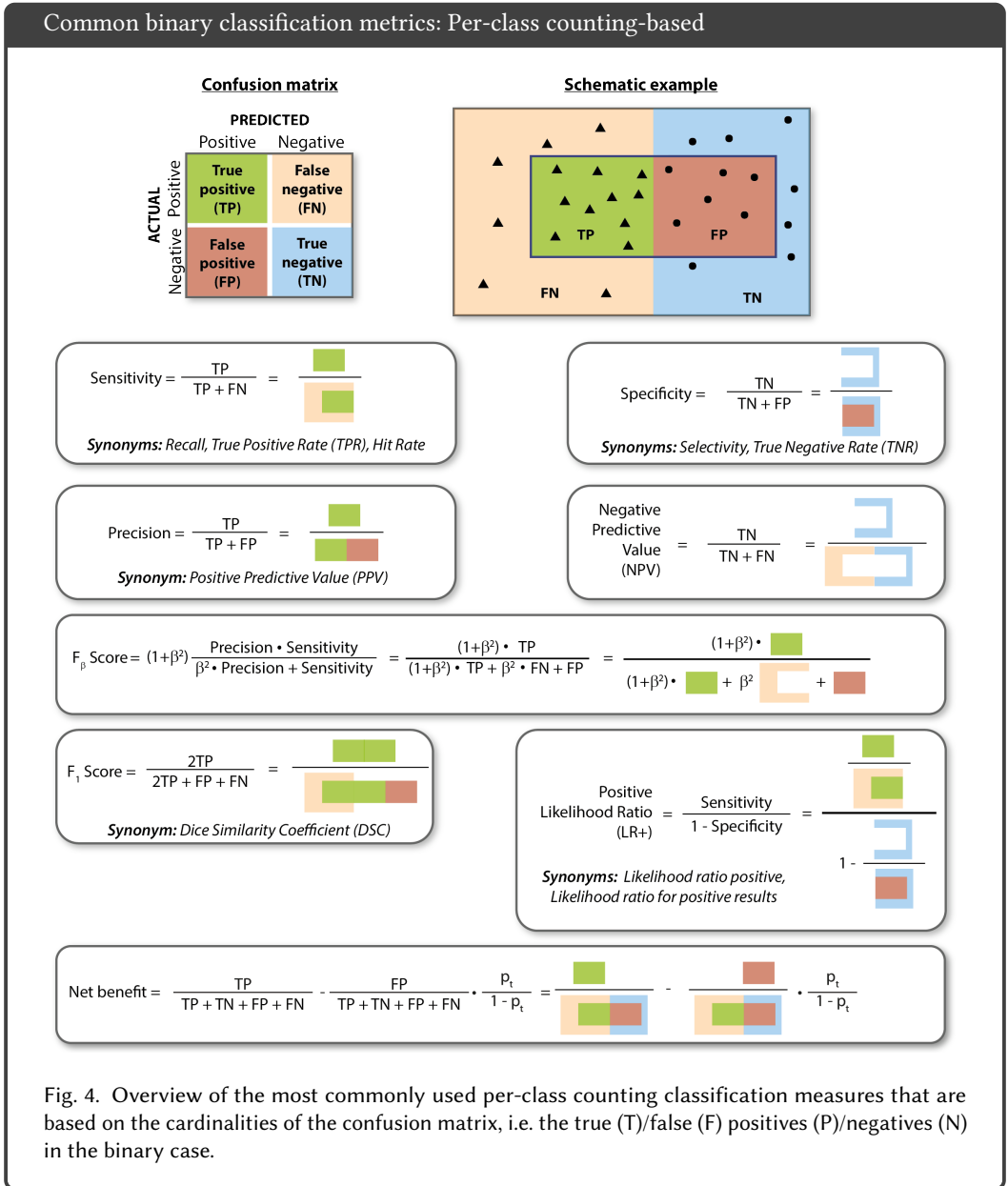
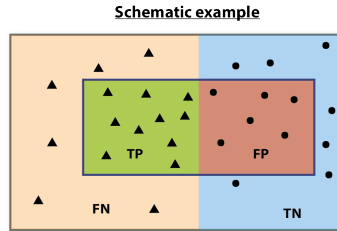


Fig. 4. Overview of the most commonly used per-class counting classification measures that are based on the cardinalities of the confusion matrix, i.e. the true (T)/false (F) positives (P)/negatives (N) in the binary case.

Common binary classification metrics: Multi-class counting-based

Confusion matrix

		PREDICTED	
		Positive	Negative
ACTUAL	Positive	True positive (TP)	False negative (FN)
	Negative	False positive (FP)	True negative (TN)



$$\text{Accuracy} = \frac{TP + TN}{TP + TN + FP + FN} = \frac{\text{TP} + \text{TN}}{\text{TP} + \text{TN} + \text{FP} + \text{FN}}$$

$$\text{Balanced Accuracy} = \frac{1}{2} (\text{Sensitivity} + \text{Specificity}) = \frac{1}{2} \left(\frac{TP}{TP + FN} + \frac{TN}{TN + FP} \right) = \frac{1}{2} \left(\frac{\text{TP}}{\text{TP} + \text{FN}} + \frac{\text{TN}}{\text{TN} + \text{FP}} \right)$$

$$\text{Youden's Index (J)} = \text{Sensitivity} + \text{Specificity} - 1 = \frac{TP}{TP + FN} + \frac{TN}{TN + FP} - 1 = \frac{\text{TP}}{\text{TP} + \text{FN}} + \frac{\text{TN}}{\text{TN} + \text{FP}} - 1$$

Synonym: Youdens' J

$$\text{Matthews Correlation Coefficient (MCC)} = \frac{TP \cdot TN - FP \cdot FN}{\sqrt{(TP + FP)(TP + FN)(TN + FP)(TN + FN)}} = \frac{TP \cdot TN - FP \cdot FN}{\sqrt{(TP + FP)(TP + FN)(TN + FP)(TN + FN)}}$$

Synonym: Phi Coefficient

$$\text{Cohen's Kappa} = \frac{p_0 - p_e}{1 - p_e} = \frac{2(TP \cdot TN - FN \cdot FP)}{(TP + FP)(FP + TN) + (TP + FN)(FN + TN)} = \frac{2(TP \cdot TN - FN \cdot FP)}{(TP + FP)(FP + TN) + (TP + FN)(FN + TN)}$$

$p_0 = \text{Accuracy}$

$$p_e = \frac{(TP + FP)(TP + FN)}{TP + TN + FP + FN} + \frac{(TN + FP)(TN + FN)}{TP + TN + FP + FN} = \frac{(TP + FP)(TP + FN)}{TP + TN + FP + FN} + \frac{(TN + FP)(TN + FN)}{TP + TN + FP + FN}$$

Synonyms: Cohen's Kappa Coefficient, Kappa Statistic, Kappa Score

$$\text{Weighted Cohen's Kappa} = \frac{p_0^w - p_e^w}{1 - p_e^w}, p_0^w = \frac{w_{TP} \cdot TP + w_{TN} \cdot TN + w_{FP} \cdot FP + w_{FN} \cdot FN}{TP + TN + FP + FN} = \frac{w_{TP} \cdot TP + w_{TN} \cdot TN + w_{FP} \cdot FP + w_{FN} \cdot FN}{TP + TN + FP + FN}$$

$$p_e^w = w_{TP} \frac{(TP + FP)(TP + FN)}{TP + TN + FP + FN} + w_{TN} \frac{(TN + FP)(TN + FN)}{TP + TN + FP + FN} + w_{FN} \frac{(FN + FP)(FN + TN)}{TP + TN + FP + FN} + w_{FP} \frac{(FP + TP)(FP + TN)}{TP + TN + FP + FN}$$

$$= w_{TP} \frac{(TP + FP)(TP + FN)}{TP + TN + FP + FN} + w_{TN} \frac{(TN + FP)(TN + FN)}{TP + TN + FP + FN} + w_{FN} \frac{(FN + FP)(FN + TN)}{TP + TN + FP + FN} + w_{FP} \frac{(FP + TP)(FP + TN)}{TP + TN + FP + FN}$$

Synonyms: Weighted Cohen's Kappa Coefficient, Weighted Kappa Statistic, Weighted Kappa Score

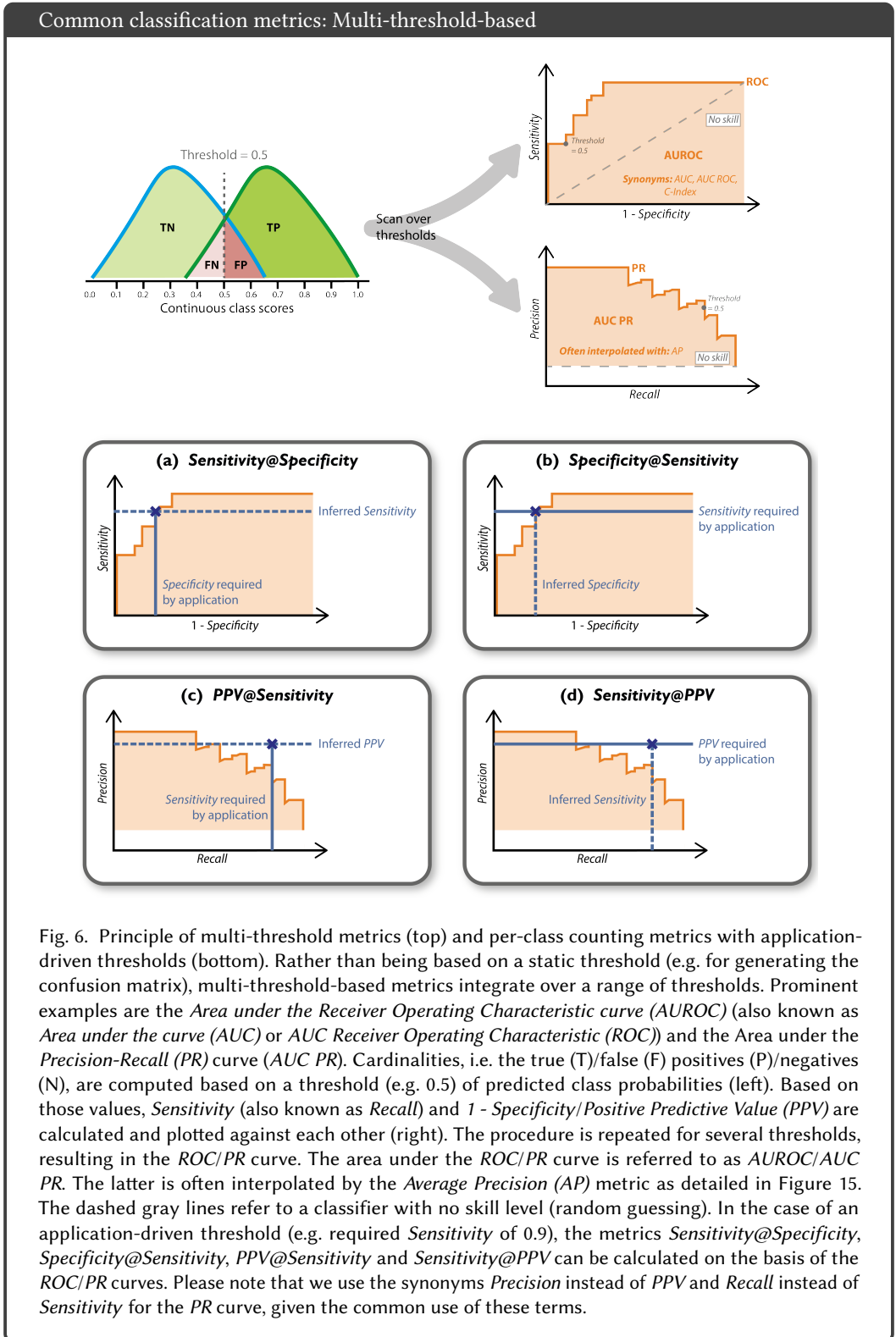
$$\text{EC} = w_{\text{miss}} \frac{FN}{TP + FN} + w_{\text{tar}} \frac{TP + FN}{TP + TN + FP + FN} + w_{\text{fa}} \frac{FP}{TN + FP} + w_{\text{tar}} \frac{TP + FN}{TP + TN + FP + FN}$$

$$= w_{\text{miss}} \frac{FN}{TP + FN} + w_{\text{tar}} \frac{TP + FN}{TP + TN + FP + FN} + w_{\text{fa}} \frac{FP}{TN + FP} + w_{\text{tar}} \frac{TP + FN}{TP + TN + FP + FN}$$

Fig. 5. Overview of the most commonly used multi-class counting classification measures that are based on the cardinalities of the confusion matrix, i.e. the true (T)/false (F) positives (P)/negatives (N) in the binary case.

Calibration metrics. While most research in biomedical image analysis focuses on the discrimination capabilities of classifiers, a complementary property of relevance is the *calibration* of predicted class scores (also known as *confidence scores*). Intuitively speaking, a system is well-calibrated if the predicted class scores (i.e., the output of the model) reflect the true probabilities of the outcome. In practice, this means that calibrated scores match the empirical success rate of associated predictions. For a binary classification task, calibration implies that of all the data samples assigned a predicted score of, for example, 0.8 for the positive class, empirically, 80% belong to this class [57].

Calibration is typically assessed by either calculating calibration errors (for example as done for the *Expected Calibration Error (ECE)* or *Maximum Calibration Error (MCE)* [63]) or by proper scoring rules (also referred to as *overall performance measures* [78]), which measure discrimination and calibration in a single score (for example the *Brier Score (BS)*). A detailed overview of calibration metrics is given in [57].



2.2 Semantic Segmentation

Semantic segmentation is commonly defined as the process of partitioning an image into multiple segments/regions. To this end, one or multiple labels are assigned to every pixel such that pixels with the same label share certain characteristics. Semantic segmentation can therefore also be regarded as pixel-level classification. As in image-classification problems, predicted class probabilities are typically calculated for each pixel deciding on the class affiliation based on a threshold over the class scores [2]. In semantic segmentation problems, the pixel-level classification is typically followed by a post-processing step, in which connected components are defined as objects, and object boundaries are created accordingly. Semantic segmentation metrics can roughly be classified into three classes: (1) counting metrics or overlap-based metrics, for measuring the overlap between the reference annotation and the prediction of the algorithm, (2) distance-based metrics, for measuring the distance between object boundaries, and (3) problem-specific metrics, measuring, for example, the volume of objects.

Counting metrics. The most frequently used segmentation metrics are **counting metrics**. In the context of segmentation they are also referred to as **overlap metrics**, as they essentially measure the overlap between a reference mask and the algorithm prediction. According to a comprehensive analysis of biomedical image analysis challenges [56], the *DSC* [24] is the by far most widely used metric in the field of medical image analysis. As illustrated in Figure 7, it yields a value between 0 (no overlap) and 1 (full overlap). The *DSC* is identical to the *F₁ Score* and closely related to the *IoU*, which is identical to the *Jaccard Index*:

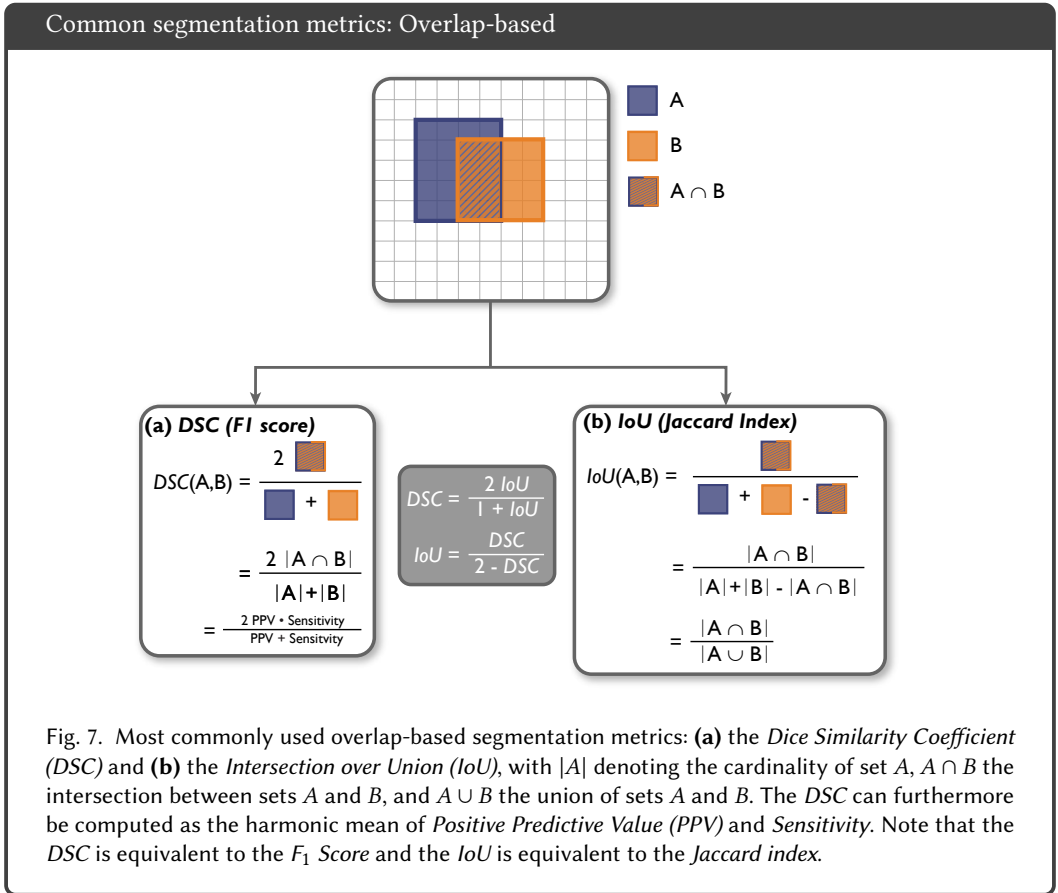
$$IoU = \frac{DSC}{2 - DSC} \quad (3) \qquad DSC = \frac{2IoU}{1 + IoU} \quad (4)$$

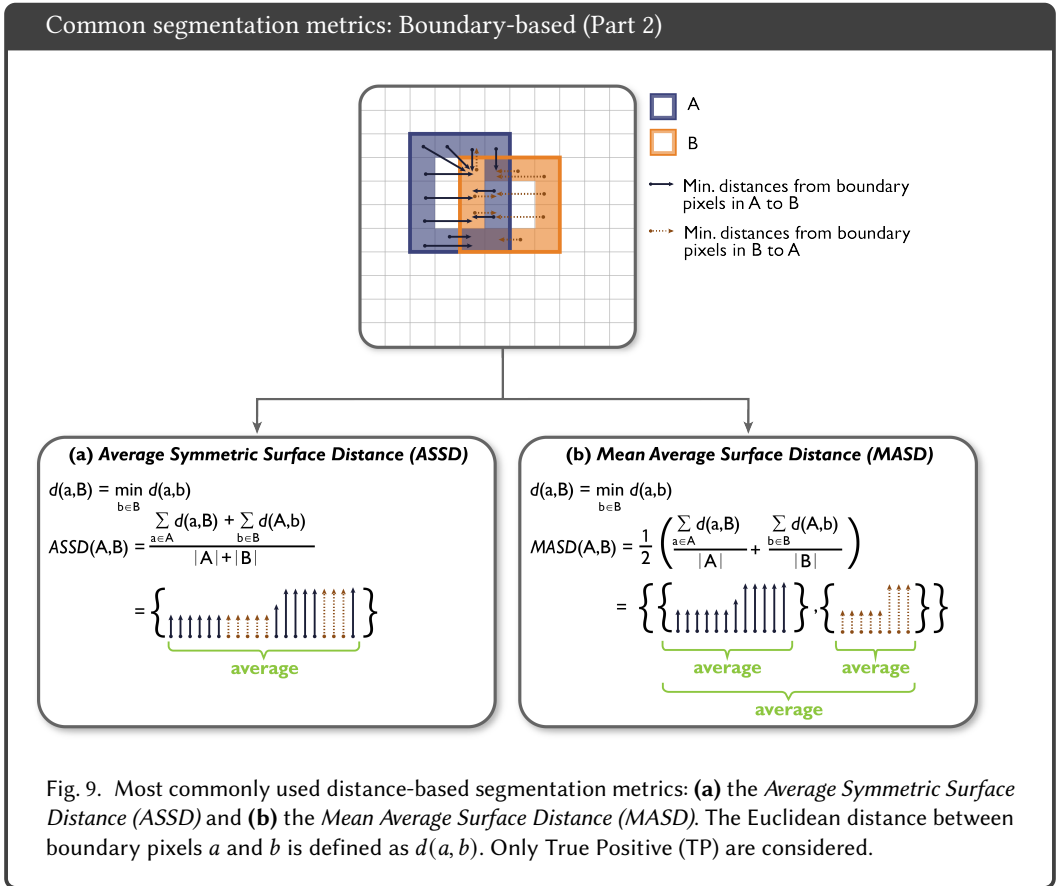
Distance-based metrics. Overlap-based metrics are often complemented by **distance-based metrics** that operate exclusively on the TP and compute one or several distances between the reference and the prediction. Apart from a few exceptions, distance-based metrics are often **boundary-based metrics** which focus on assessing the accuracy of object boundaries. According to [56], the *HD* and its 95% percentile variant (*Hausdorff Distance 95% Percentile (HD95)*) [40] are the most commonly used boundary-based metrics. The *HD* calculates the maximum of all shortest distances for all points from one object boundary to the other, which is why it is also known as the *Maximum Symmetric Surface Distance* [92]. The *HD95* calculates the 95% percentile instead of the maximum, therefore disregarding outliers (see Figure 8). Another popular metric is the *Average Symmetric Surface Distance (ASSD)*, measuring the average of all distances for every point from one object to the other and vice versa [86, 92]. However, if one boundary is much larger than the other, it will impact the score much more. This is avoided by the *Mean Average Surface Distance (MASD)* [6], which treats both structures equally by computing the average distance from structure *A* to structure *B* and the average distance from structure *B* to structure *A* and averaging both (see Figure 9). For the *HD(95)*, *MASD* and *ASSD* metrics, a value of 0 refers to a perfect prediction (distance of 0 to the reference boundary), while there exists no fixed upper bound. The *Boundary IoU* (cf. Figure 12) is another option for measuring the boundary quality of a prediction. It measures the overlap between prediction and reference up to a certain width (which is controlled by the width parameter *d*) (see Sec. 2.3 for details) and is bounded between 0 and 1.

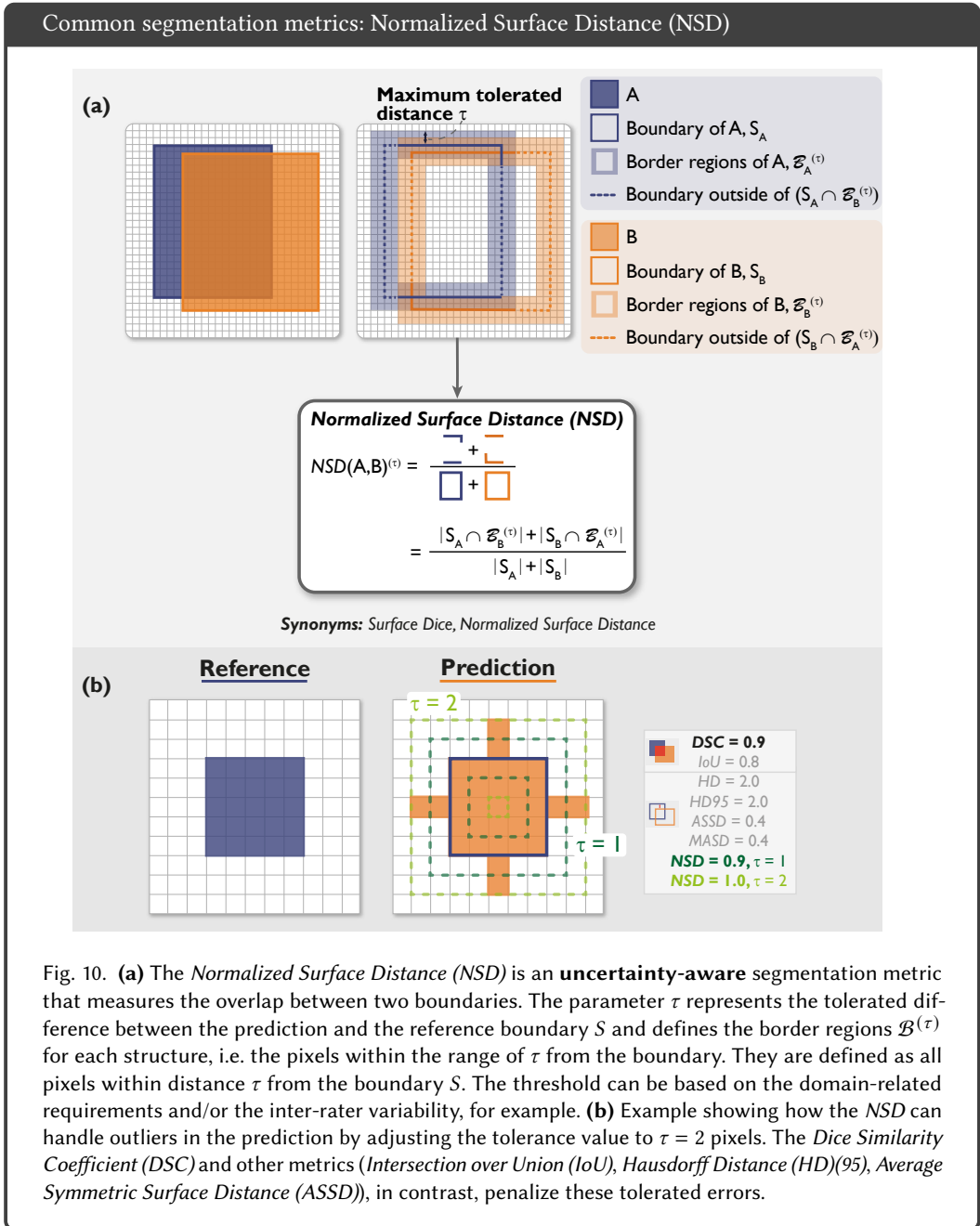
A major problem related to boundary-based metrics are the error-prone reference annotations (see Figs. 62 and 63). In fact, domain experts often disagree on the definition and annotation of objects and their boundaries [44]. While the *HD(95)* and *ASSD* are not robust with respect to uncertain reference annotations, the *NSD* was explicitly designed for this purpose as a hybrid metric between

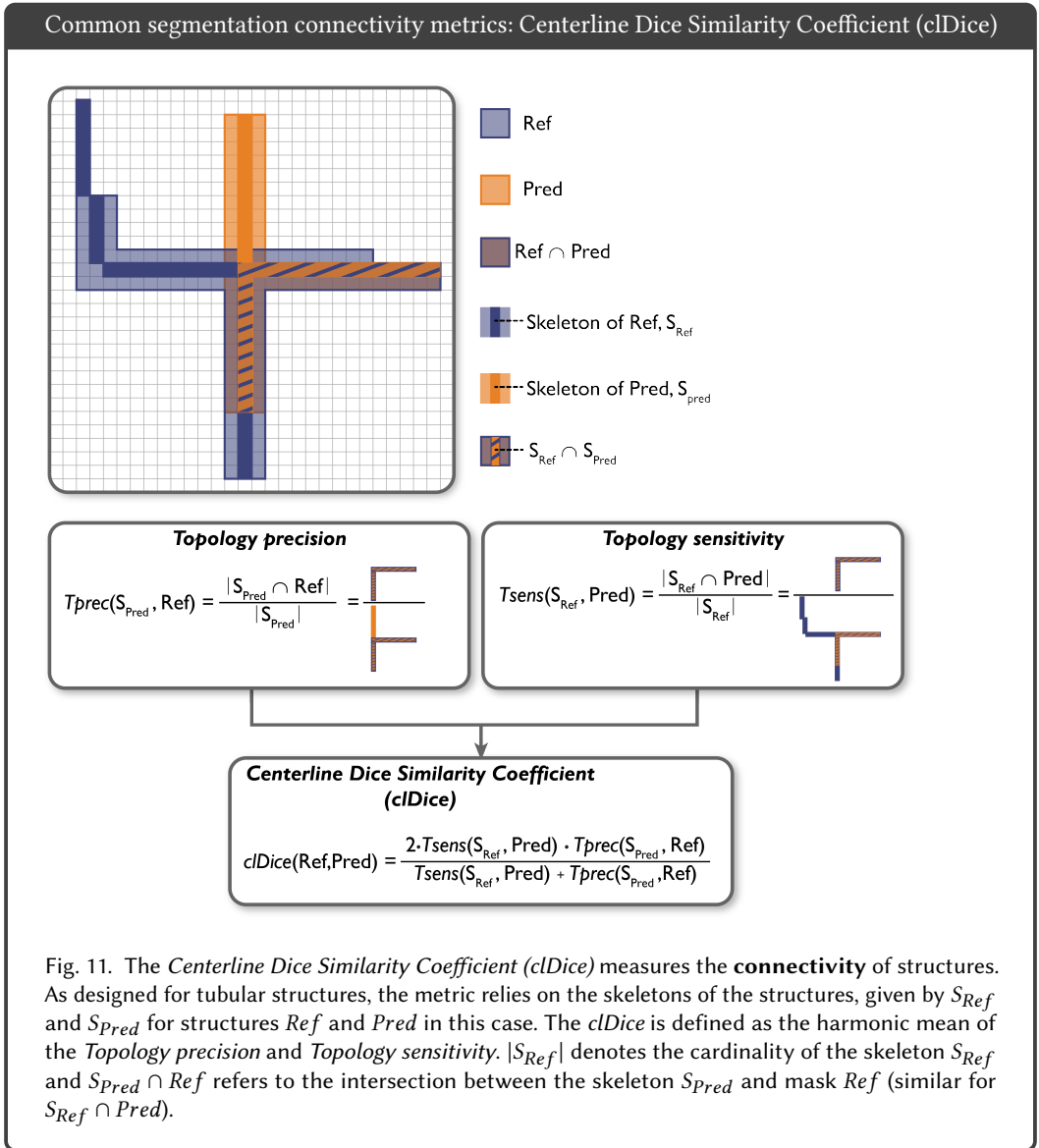
boundary-based and counting-based approaches. Known uncertainties in the reference as well as acceptable deviations of the predicted boundary from the reference are captured by a threshold τ [67], as shown in Figure 10. Only boundary parts within the border regions defined by τ are counted as TP. The metric is bounded between 0 (no boundary overlap) and 1 (full boundary overlap), so that it can be interpreted similarly to the classical *DSC* (though restricted to the boundary). Please note that τ is another important hyperparameter which should be chosen wisely, based on inter-rater agreement, for example.

Problem-specific segmentation metrics. While overlap-based metrics and distance-based metrics are the standard metrics used by the general computer vision community, biomedical applications often have special domain-specific requirements. In medical imaging, for example, the actual volume of an object may be of particular interest (for example tumor volume). In this case, **volume metrics** such as the *Absolute* or *Relative Volume Error* and the *Symmetric Relative Volume Difference* can be computed [64]. However, they are less common than overlap metrics, as the location of objects is not considered at all (see Figure 58). If the structure center or center line is of particular interest (e.g. in cells or vessels), **connectivity metrics** come into play, which measure the agreement of the center line between two objects. This is of special interest if linear or tube-like objects are present in a data set, for example in brain vascular analysis. In these cases, over- or undersegmentation are typically not of special interest, with the focus rather being on connectivity or network topology. For this purpose, the *Centerline Dice Similarity Coefficient (clDice)* [75] has been designed. For computation, the reference and prediction skeletons need to be extracted from the binary masks. Multiple approaches have been proposed, as described in [75]. As shown in Figure 11, the *clDice* is then defined as the harmonic mean of *Topology Precision* and *Topology Sensitivity*. The *Topology Precision* measures the ratio of the overlap of the skeleton of the prediction skeleton and the reference mask and the skeleton of the prediction. Similarly to *Precision*, it measures the FP samples. On the other hand, *Topology Sensitivity* incorporates FN samples by measuring the ratio of the overlap of the skeleton of the reference and the prediction mask and the reference skeleton.









2.3 Object Detection

Object detection refers to the detection of one or multiple objects (or: instances) of a particular class (e.g. lesion) in an image [54]. The following description assumes single-class problems, but translation to multi-class problems is straightforward, as validation for multiple classes on object level is performed individually per class. Notably, as multiple predictions and reference instances may be present in one image, the predictions need to include localization information, such that a matching between reference and predicted objects can be performed. Important design choices with respect to the validation of object detection methods include:

- (1) *How to represent an object?* Representation is typically composed of location information and a class affiliation. The former may take the form of a bounding box (i.e. a list of coordinates), a pixel mask, or the object's center point. Additionally, modern algorithms typically assign a confidence value to each object, representing the probability of a prediction corresponding to an actual object of the respective class. Note that a confusion matrix is later computed for a fixed threshold on the predicted class probabilities.⁶
- (2) *How to decide whether a reference instance was correctly detected?* This step is achieved by applying the *localization criterion*. This may, for example, be based on comparing the object centers of the reference and prediction or computing their overlap (Figs. 68 and 70).
- (3) *How to resolve assignment ambiguities?* The above step might lead to ambiguous matchings, such as two predictions being assigned to the same reference object. Several strategies exist for resolving such cases.

The following sections provide details on (1) applying the localization criterion, (2) applying the assignment strategy and (3) computing the actual performance metrics.

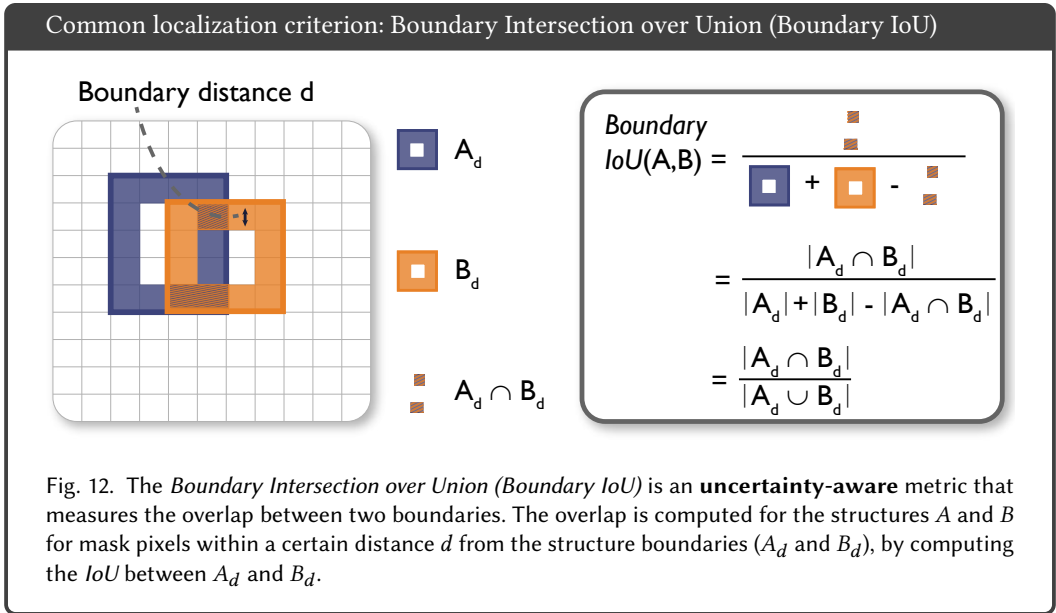
Localization criterion. As one image may contain multiple objects or no object at all, the **localization criterion** or **hit criterion** measures the (spatial) similarity between a prediction (represented by a bounding box, pixel mask, center point or similar) and a reference object. It defines whether the prediction *hit/detected* (TP) or *missed* (FP) the reference. Any reference object not detected by the algorithm is defined as FN. Please note that TN are not defined for object detection tasks, which has several implications on the applicable metrics, as detailed below.

There are multiple ways to define the localization or hit criterion (see Figs. 7, 12 and 68). Popular center-based localization criteria are (a) *the center-cover criterion*, for which the reference object is considered hit if the center of the reference object is inside the predicted detection, (b) *the distance-based hit criterion*, which considers a TP if the distance d between the center of the reference and the detected object is smaller than a certain threshold τ and (c) *the center-hit criterion*, which holds true if the center of the predicted object is inside the reference bounding box or mask.

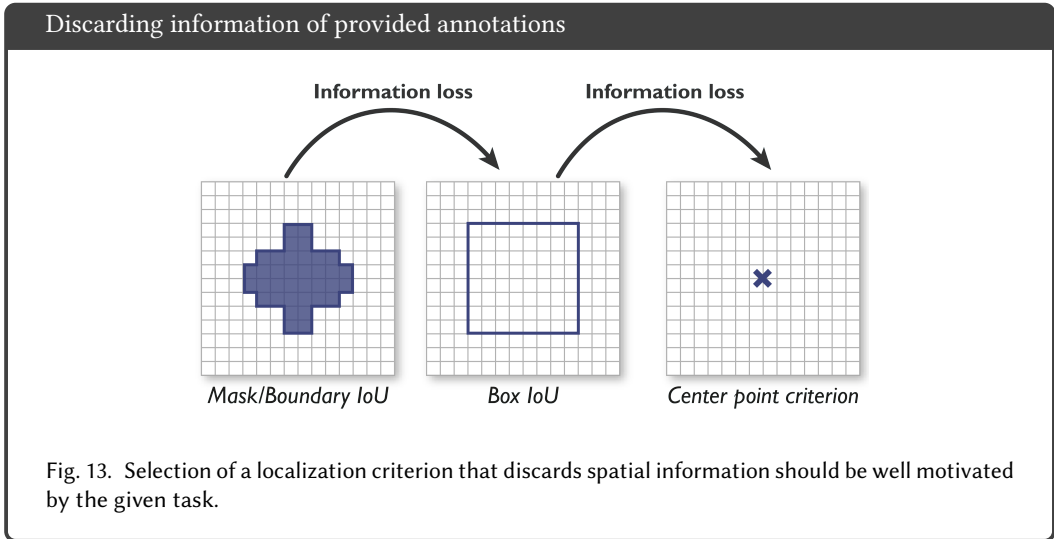
The most commonly used overlap-based hit criterion is determined by computing the *IoU* [41] (cf. Figure 7b). The prediction is considered as TP if the overlap is larger than a certain threshold (e.g. 0.3 or 0.5) and as FP otherwise. If bounding boxes are considered, the *IoU* is computed between the reference and predicted bounding boxes (*Box IoU*). For more fine-grained annotations in form of a pixel mask, the *IoU* may be computed for the complete mask (*Mask IoU*). The *Mask IoU* is less sensitive to structure boundary quality in larger objects (cf. Sec. 5). This is due to the fact that boundary pixels will increase linearly while pixels inside the structure will increase quadratically

⁶Please note that we will use the term confidence scores analogously to predicted class probabilities in the context of object detection and instance segmentation.

with an increase in structure size. The *Boundary IoU* measures the *IoU* of two structures for mask pixels within a certain distance d from the structure boundaries [14], as illustrated in Figure 12.



The localization criterion should be carefully chosen according to the underlying motivation and research question and depending on the available coarseness of annotations. However, it should be noted that annotations of a lower resolution will result in an information loss, as illustrated in Figure 13. For example, the *Box IoU* is sometimes used although pixel-mask annotations are available because algorithms are expected to output rough localization in the shape of boxes. Such a simplification might cause problems if structures are not well-approximated by a box shape, or if structures can overlap causing multi-component masks (cf. Sec. 6, Figure 73). Lastly, it should be noted that the decision for a cutoff value on the localization criterion leads to instabilities in the validation (e.g. see Figure 70). For this reason, it is common practice in the computer vision community to average metrics over multiple cutoff values (default for *IoU* criteria: 0.50:0.05:0.95 [54]). Generally speaking, the cutoff values should be chosen according to the driving biomedical question. For example, if particular interest lies on the exact outlines, higher thresholds should be chosen. On the other hand, for noisy reference standards, a low cutoff value is preferable.



Assignment strategy. The localization criterion alone is not sufficient to extract the final confusion matrix based on a fixed threshold for the predicted class probabilities (confidence scores), as ambiguities can occur. For example, two predictions may have been assigned to the same reference object in the localization step, or vice versa. These ambiguities need to be resolved in a further **assignment step**, as exemplarily shown in Figure 14.

This assignment and thus the resolving of potential assignment ambiguities can be done via different strategies. The most common strategy in the computer vision community is the *Greedy by Score* strategy [26]. All predictions in an image are ranked by their predicted class probability and iteratively (starting with the highest probability) assigned to the reference object with the highest localization criterion for this prediction. The selected reference object is subsequently removed from the process since it can not be matched to any other prediction (unless double assignments are allowed). The *Hungarian Matching* [52] is associated with a cost function, usually depending on the localization criterion, which is minimized to find the optimal assignment of predictions and reference. In the biomedical domain, more sophisticated matching strategies are often avoided by setting the localization criterion threshold to $IoU > 0.5$ and only allowing non-overlapping object predictions (which inherently avoids matching conflicts). In the case of a high ratio of touching reference objects and common non-split errors, meaning that one prediction overlaps with multiple reference objects, the Intersection over Reference (*IoR*) [59] might be considered as an alternative to *IoU* [59] (see Figure 72).

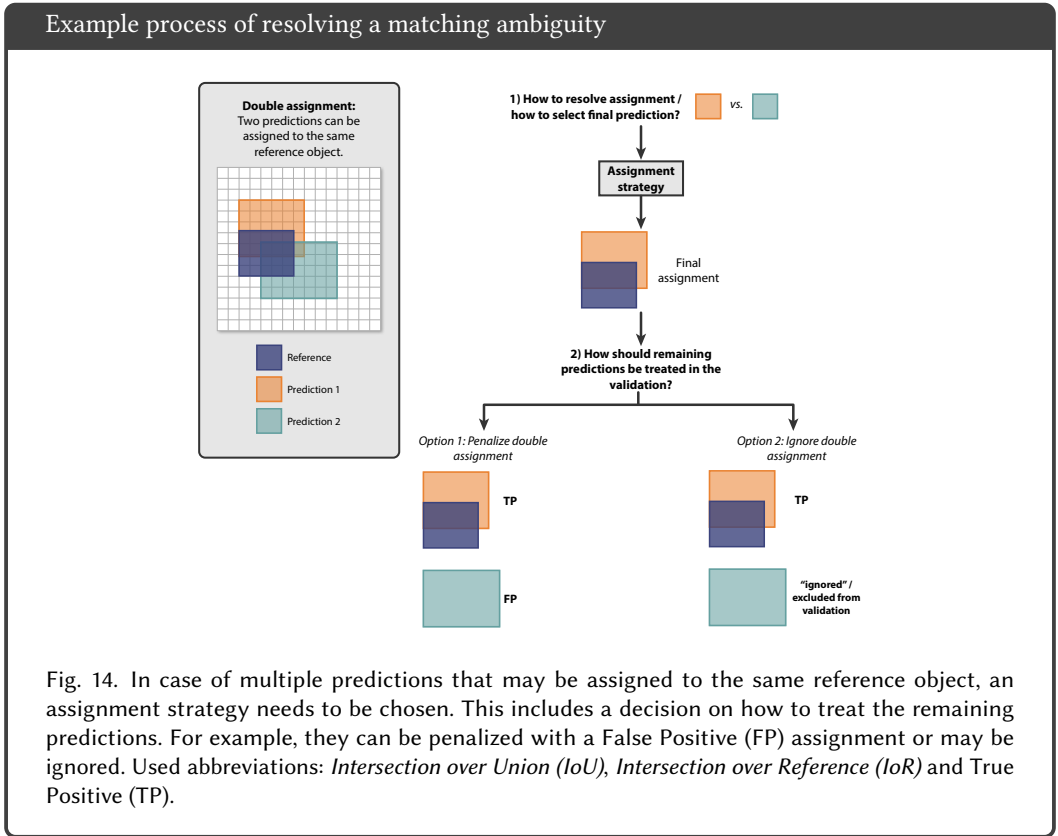


Fig. 14. In case of multiple predictions that may be assigned to the same reference object, an assignment strategy needs to be chosen. This includes a decision on how to treat the remaining predictions. For example, they can be penalized with a False Positive (FP) assignment or may be ignored. Used abbreviations: *Intersection over Union (IoU)*, *Intersection over Reference (IoR)* and True Positive (TP).

Metric computation. Similar to image-level classification and semantic segmentation algorithms, object detection algorithms are commonly assessed with counting metrics, assuming a fixed confusion matrix, (cf. Figs. 4 and 5). However, one of the most popular object detection metrics is the multi-threshold metric *Average Precision (AP)* [54], which is the area under the *Precision-Recall (PR)* curve for a certain interpolation scheme. The *PR* curve is computed similarly to the *ROC* curve by scanning over confidence thresholds and computing the *Precision (PPV)* and *Recall (Sensitivity)* for every threshold (cf. Figure 6). Note in this context that the popular *ROC* curve is not applicable in object detection tasks because *TN* are not available. Also, while the *ROC* curve is monotonically rising, this behavior may not be expected from the *PR* curve, which typically features a zigzag shape, as illustrated in Figure 15. Specifically "as the level of *Recall* varies, the *Precision* does not necessarily change linearly due to the fact that *FP* replaces *FN* in the denominator of the *Precision* metric." [20]. A linear interpolation would therefore be overly optimistic, which is why more complex interpolation is needed, as detailed in [20].

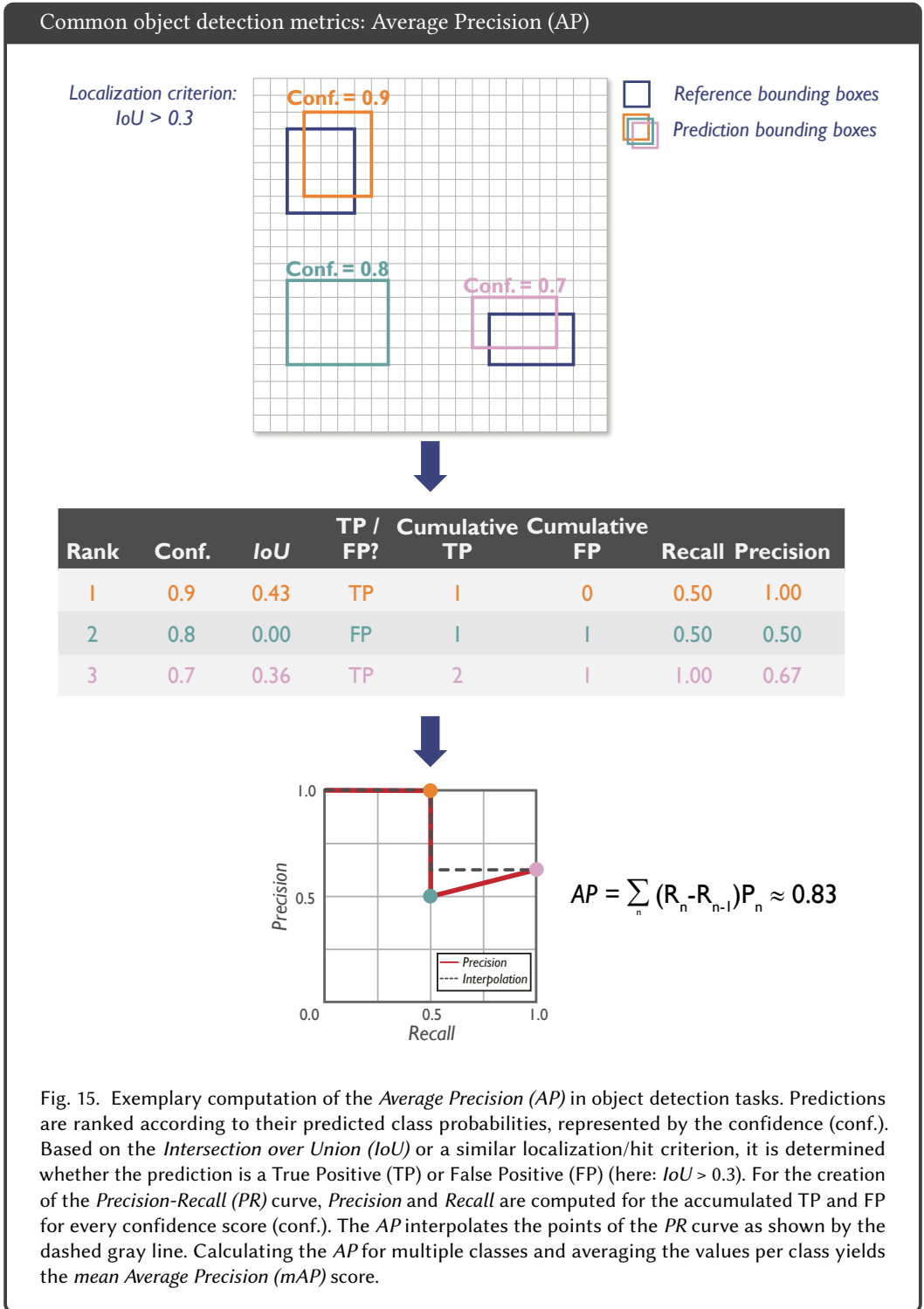
The area under the *PR* curve is typically calculated as the *AP* implying a conservative simplification of curve interpolation,

$$AP = \sum_i (R_i - R_{i-1})P_i, \quad (5)$$

with R_i and P_i denoting the *Recall* and *Precision* at the i th threshold⁷ (cf. dashed gray line in Figure 15). For the *PR* curve, an optimal model would lead to *Recall (Sensitivity)* and *Precision (PPV)* of 1, therefore being the point (1, 1) on the *PR* curve. Conversely, a model with no skill level (random guessing) would result in a horizontal line with a precision proportional to the portion of positive samples, i.e. the prevalence (dashed line in Figure 6). For computation of the metric (for a given class), the predictions are sorted in descending order of the confidence for each prediction (for that class). For each possible confidence threshold, the cardinalities are computed and the resulting tuple of *Recall (Sensitivity)* and *Precision* is added to the curve (cf. Figure 15). In the case of multiple classes, the *AP* is calculated per class and averaged to obtain the *mean Average Precision (mAP)* score.

In contrast to drawing the *PR* curve and computing the *AP*, *Free-Response Receiver Operating Characteristic (FROC)* curve is often favoured in the clinical context due to its easier interpretability. It operates at object level and plots the average number of *FPPI* (in contrast to the *FPR*) against the *Sensitivity* [13, 87] (cf. Figure 16). The *FROC Score*, measured as the area under the *FROC* curve, however, is not bounded between 0 and 1 and the employed *FPPI* scores vary across studies, such that there exists no standardized definition of an area under the respective curve. Overall, the decision between the two metrics often boils down to a decision between a standardized and technical validation versus an interpretable and application-focused validation.

⁷https://scikit-learn.org/stable/modules/generated/sklearn.metrics.average_precision_score.html



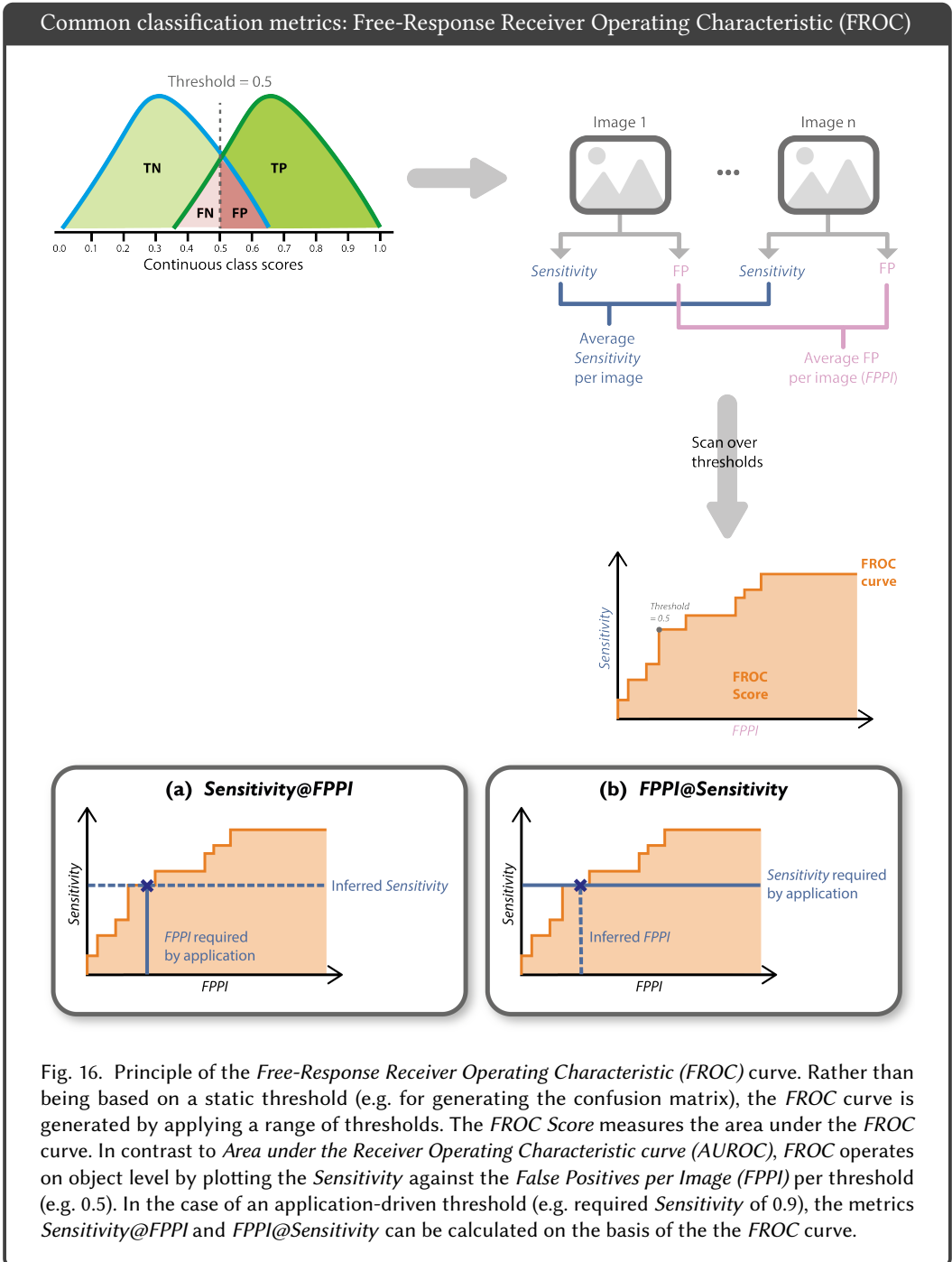
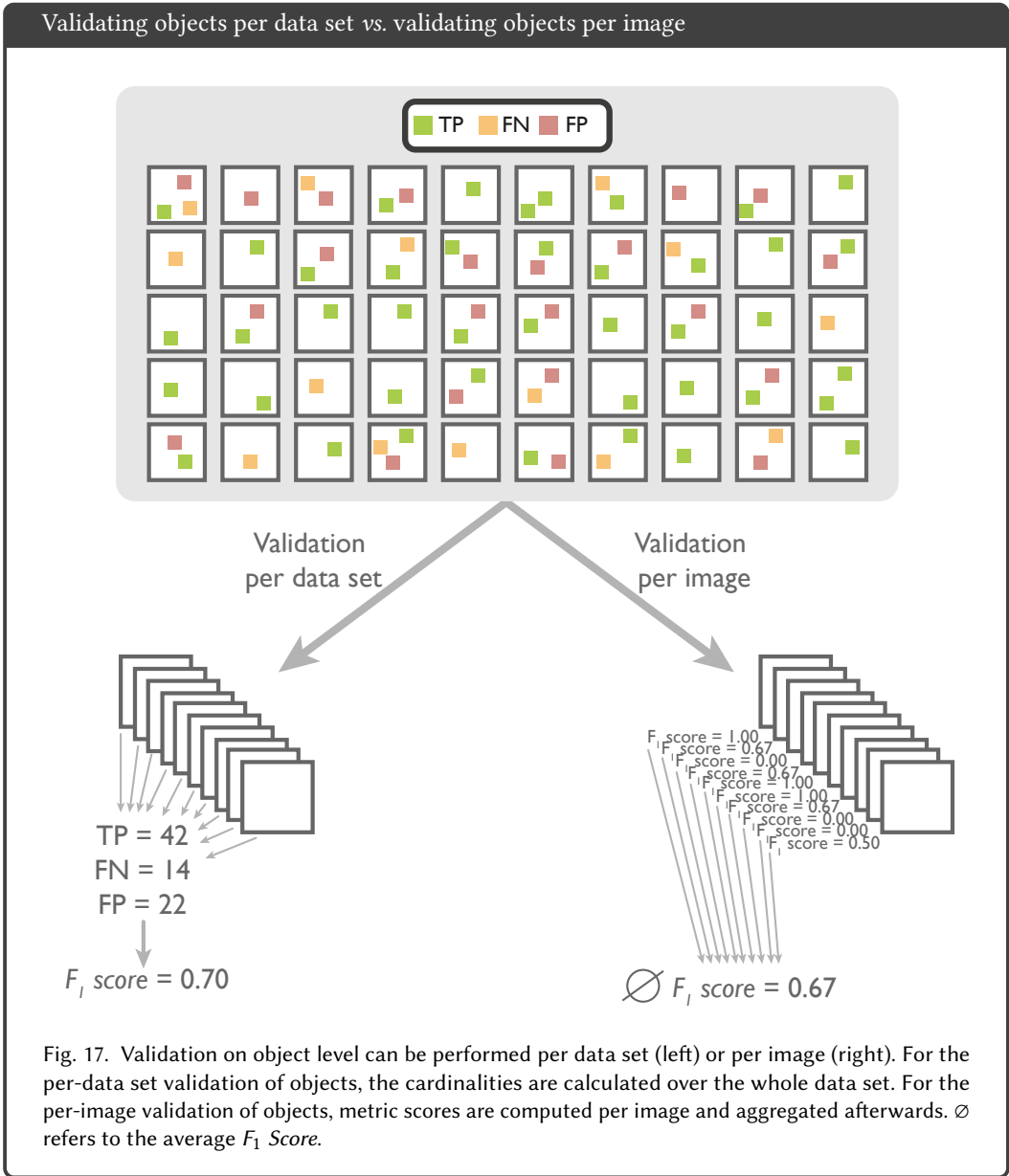


Fig. 16. Principle of the *Free-Response Receiver Operating Characteristic (FROC)* curve. Rather than being based on a static threshold (e.g. for generating the confusion matrix), the *FROC* curve is generated by applying a range of thresholds. The *FROC Score* measures the area under the *FROC* curve. In contrast to *Area under the Receiver Operating Characteristic curve (AUROC)*, *FROC* operates on object level by plotting the *Sensitivity* against the *False Positives per Image (FPPI)* per threshold (e.g. 0.5). In the case of an application-driven threshold (e.g. required *Sensitivity* of 0.9), the metrics *Sensitivity@FPPI* and *FPPI@Sensitivity* can be calculated on the basis of the the *FROC* curve.

Counting cardinalities at different scales. In image-level classification problems, validation is naturally performed on the entire data set, while segmentation typically relies on computing metrics for each image and then aggregating metric values. This latter approach is not applicable in object detection in a straightforward manner because of the relatively small number of samples per image (typically a few objects rather than thousands of pixels). Figure 17 illustrates the per-image and the per-data set validation of objects. In the per-image aggregation approach, special care needs to be taken in the case of an empty reference or prediction, as detailed in Sec. 6 (Figure 76).

A few comments on how to compute evaluation metrics while aggregating matched objects per image:

- **Counting metrics:** Computing per-class metrics such as Sensitivity, PPV, or F_1 Score (see Figure 4) works intuitively (as depicted in Figure 17) by computing a score per image and averaging scores over the data set while considering the Not A Number (NaN) conventions shown in Figure 76.
- **Multi-threshold metrics:** While scanning over all thresholds in the data set (analogously to per data set evaluation), for every threshold the Precision (PPV) and Recall (Sensitivity) scores are computed per image/patient (while considering the NaN conventions in Figure 76) and averaged over the data set. The averaged Precision and Recall score pairs per threshold form the PR curve. The AP (see Figure 15) can be computed for this curve analogously to the per-data set evaluation. The FROC curve computation works analogously while replacing Precision per image with FPPI.
- **Single working point evaluation:** A single working point (e.g. PPV@Sensitivity) can be retrieved based on the curves resulting from multi-threshold evaluation described above.



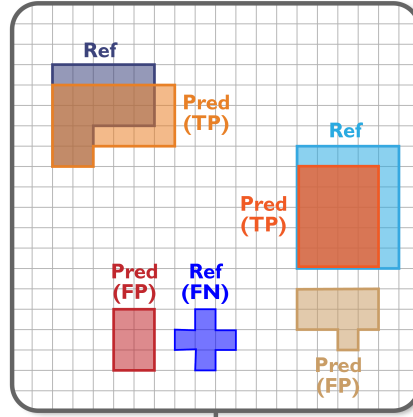
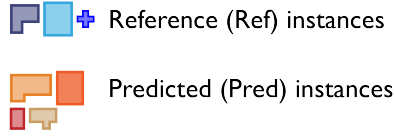
2.4 Instance Segmentation

In contrast to semantic segmentation, **instance segmentation** problems distinguish different instances of the same class (e.g. different lesions). Similarly to object detection problems, the task is to detect individual instances of the same class, but detection performance is measured by pixel-level correspondences (as in semantic segmentation problems). Optionally, instances can be applied

to one of multiple classes. Validation metrics in instance segmentation problems often combine common detection metrics with segmentation metrics applied per instance.

If detection and segmentation performance should be assessed simultaneously in a single score, the *Panoptic Quality (PQ)* metric can be utilized [46]. As shown in Figure 18, the segmentation quality is assessed by averaging the *IoU* scores for all TP instances. While this part alone would neglect FP and FN predictions, it is multiplied with the detection quality, which is equal to the *F₁ score*. For perfect segmentation results, i.e. an average *IoU* of 1, the *PQ* would simply equal the *F₁ Score*. In other words, while segmentation quality in the *F₁ Score* is merely integrated via a hard cutoff during localization (e.g. *IoU* > 0.5) affecting the counts of TP versus FP and FN, *PQ* allows for a continuous measurement of segmentation quality by 1) employing a loose prior localization criterion (e.g. *IoU* > 0, i.e. any prediction overlapping with a reference instance is treated as TP) and 2) replacing the simple counting of TP by adding up the continuous *IoU* scores per TP. *PQ* was introduced for panoptic segmentation problems that are a combination of semantic and instance segmentation [46]. It is computed per class (including background classes) and can therefore be directly used for instance segmentation problems by only assessing the foreground instances. If needed, the background quality can also be assessed.

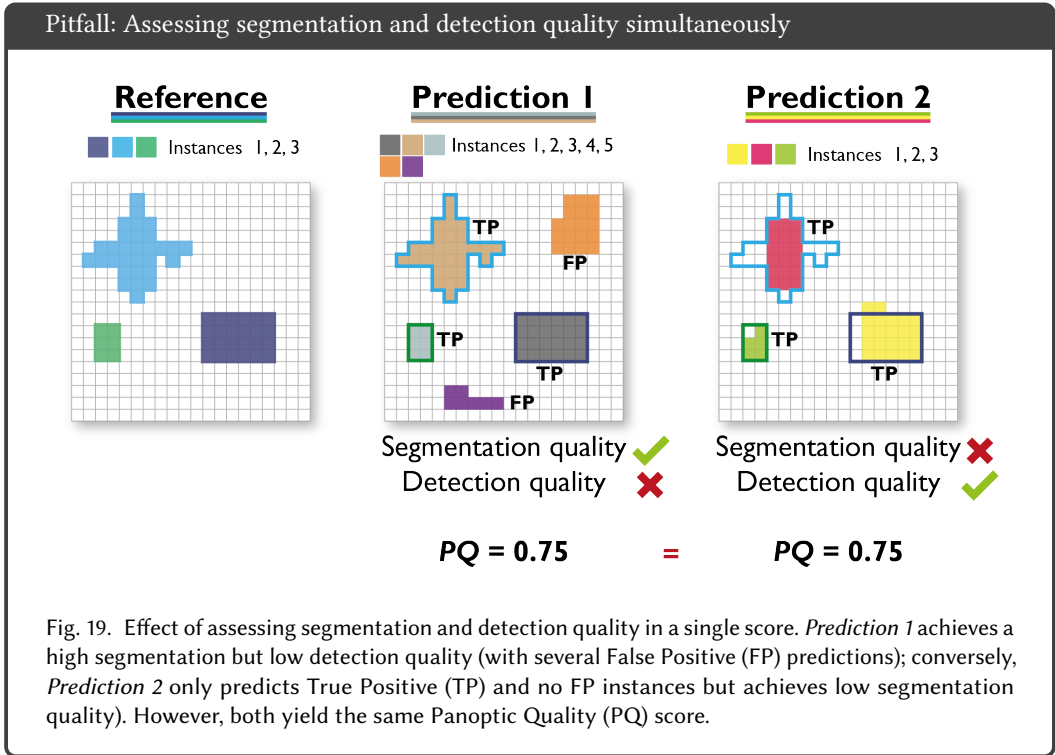
Common instance segmentation metrics: Panoptic Quality (PQ)

**Panoptic Quality (PQ)**

$$\begin{aligned}
 PQ &= \frac{\sum_{(\text{Ref}, \text{Pred}) \in \text{TP}} \text{IoU}(\text{Ref}, \text{Pred})}{|\text{TP}| + 0.5 |\text{FP}| + 0.5 |\text{FN}|} \\
 &= \underbrace{\frac{\sum_{(\text{Ref}, \text{Pred}) \in \text{TP}} \text{IoU}(\text{Ref}, \text{Pred})}{|\text{TP}|}}_{\text{Segmentation quality}} \cdot \underbrace{\frac{|\text{TP}|}{|\text{TP}| + 0.5 |\text{FP}| + 0.5 |\text{FN}|}}_{\text{Detection quality}} \\
 &= \frac{\text{IoU}(\text{blue square}, \text{orange square}) + \text{IoU}(\text{blue square}, \text{red square})}{|\{\text{orange square}, \text{red square}\}|} \cdot \frac{|\{\text{orange square}, \text{red square}\}|}{|\{\text{orange square}, \text{red square}\}| + 0.5 |\{\text{red square}, \text{light brown square}\}| + 0.5 |\{\text{blue plus}\}|}
 \end{aligned}$$

Fig. 18. The *Panoptic Quality* (PQ) measures the **segmentation and detection quality** of a prediction in one score. The segmentation quality is assessed via the *Intersection over Union* (IoU) for every predicted True Positive (TP) instance. The detection quality is measured via the F_1 score by taking into account the False Positive (FP) and False Negative (FN) predictions.

PQ covers segmentation and detection quality in a single score. However, this can be misleading, as shown in Fig. 19. *Prediction 1* with a perfect segmentation and poor detection achieves a PQ score similar to that of *Prediction 2*, which detects all objects correctly (without any FP or FN), but only provides moderate segmentation results. If segmentation and detection quality should be assessed individually, two separate metrics - one for segmentation quality and one for detection quality - should be preferred.



It should be noted that instance segmentation problems are often phrased as semantic segmentation problems with an additional post-processing step, such as connected component analysis [72]. In practice, predicted class probabilities, yielded by modern segmentation algorithms, are often discarded in the post-processing step and are thus not available for subsequent validation. Figure 20 illustrates how to overcome this potential problem.

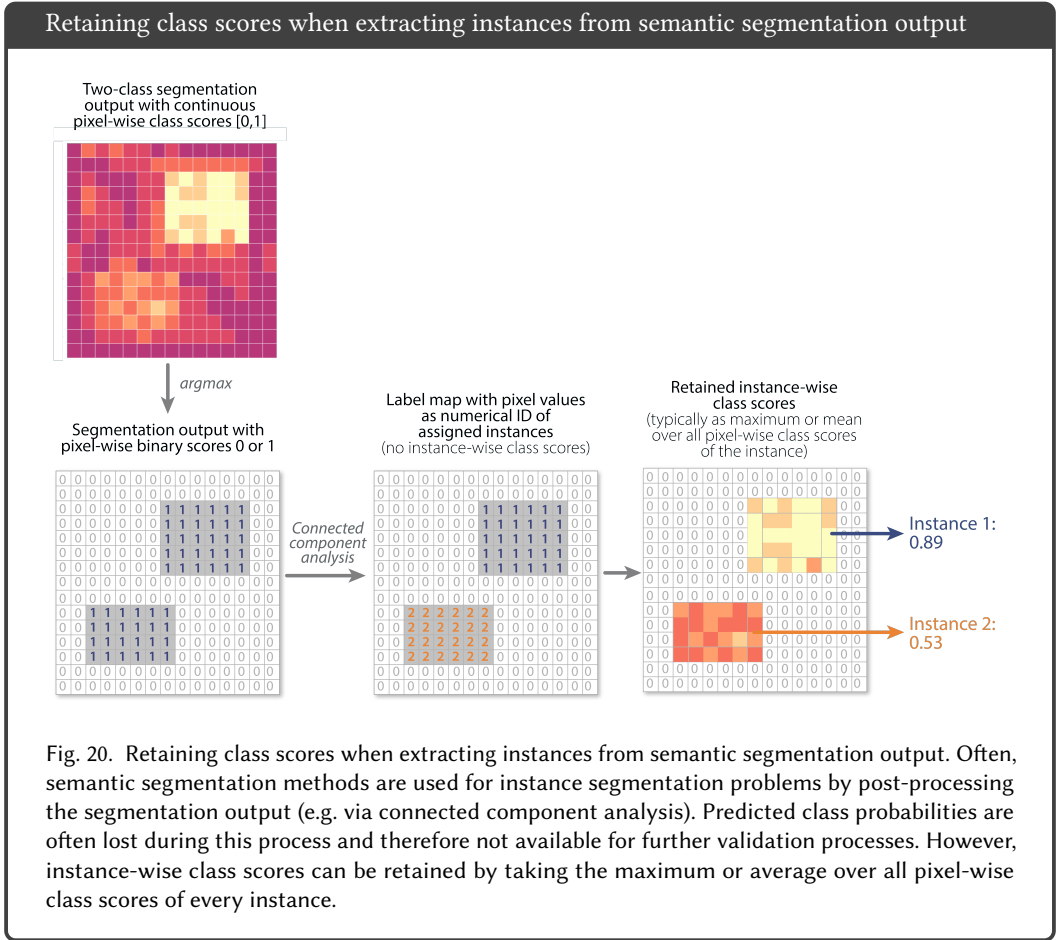
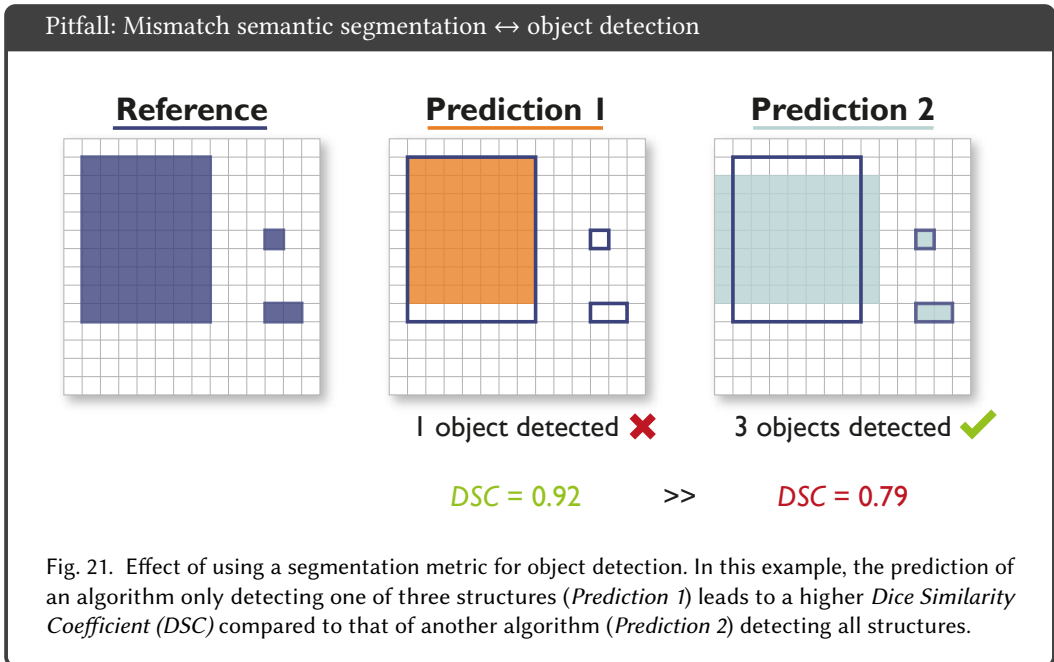


Fig. 20. Retaining class scores when extracting instances from semantic segmentation output. Often, semantic segmentation methods are used for instance segmentation problems by post-processing the segmentation output (e.g. via connected component analysis). Predicted class probabilities are often lost during this process and therefore not available for further validation processes. However, instance-wise class scores can be retained by taking the maximum or average over all pixel-wise class scores of every instance.

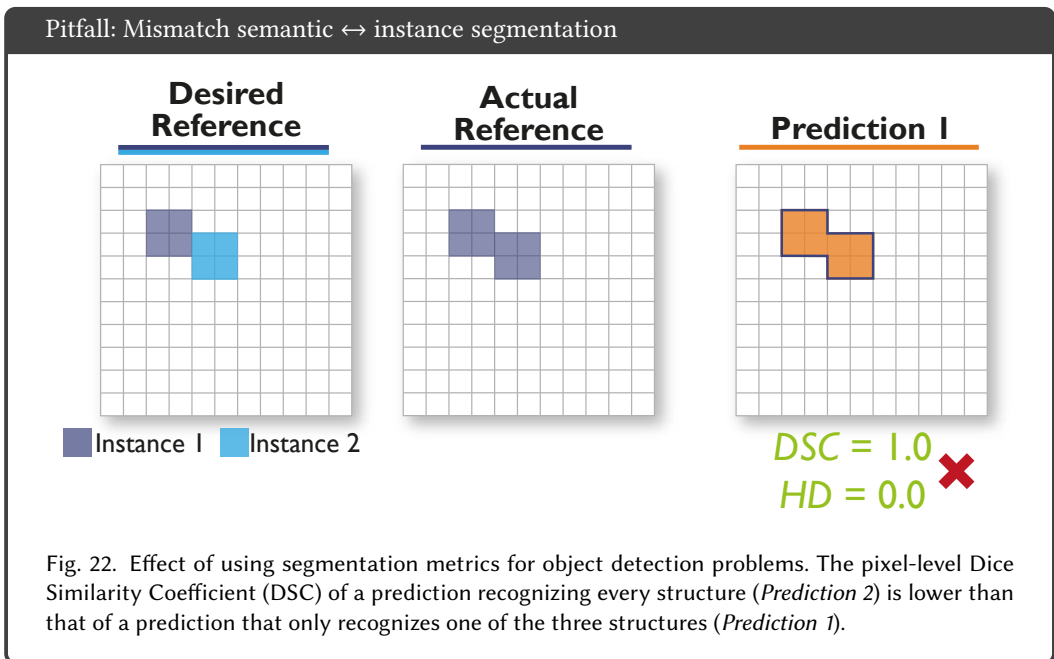
3 PITFALLS DUE TO CATEGORY-METRIC MISMATCH

Performance metrics are typically expected to reflect a domain-specific validation goal (e.g. clinical goal). Previous research, however, suggests, that this is often not the case [74]. Before choosing validation metrics, the correct problem category needs to be defined. In the following, we will describe pitfalls related to metrics not being applied to the appropriate problem category.

Mismatch semantic segmentation \leftrightarrow object detection. A common problem is that segmentation metrics, such as the *DSC*, are applied to *object detection* tasks [12, 43], as illustrated in Figure 21. From a clinical perspective, for example, the algorithm producing *Prediction 2* and covering all three structures of interest (e.g. tumors) would be clinically much more valuable compared to the one producing a highly accurate segmentation for one structure but missing the other two in *Prediction 1*. This is not reflected in the metric values, which are substantially higher for *Prediction 1*. In general, the *DSC* is strongly biased against single objects, therefore not appropriate for the detection of multiple structures [46, 92].



Mismatch semantic \leftrightarrow **instance segmentation**. In segmentation problems, the driving research question should decide whether semantic or instance segmentation should be chosen for validation. This is particularly relevant when multiple objects within one image overlap or touch, as often occurring in cell images. For semantic segmentation problems, overlapping or touching objects may end up merged into a single object without clear boundaries or distinction between the single objects. Instance segmentation problems, on the other hand, ensure that the borders of touching or overlapping structures can be accurately assigned and that objects can be differentiated. If instance segmentation is preferred, the labels need to be chosen accordingly. An example is shown in Figure 22: The desired annotation consists of two different instances, but only semantic labels are available (middle). A prediction will only be as accurate as the reference, hence detecting only one instance but yielding a perfect metric score although the desired task is not solved.



Mismatch image-level classification \leftrightarrow object detection. Tasks that should be validated at image level are sometimes erroneously approached with object detection models instead of image-level classification models [42]. Object detection models are designed to handle different objects in an image rather than the complete image and will naturally introduce problems in a validation setting on image level. Object detection tasks are dependent on choosing a proper localization criterion, which is not needed for an image-level classification problem. For example, a *ROC* curve, typically used for assessing the performance of image-level classification algorithms, does not consider the localization step needed in object detection tasks, as it was designed to validate at image rather than object level. It therefore does not take into account whether a detected object is at the correct location in the image. Moreover, when validation on image level is conducted by using an object detection model, the detection with the largest class probability (confidence score) of all detections in one image is usually taken, neglecting all other predictions. This does not capture the performance of the model accurately. Figure 23 illustrates some of the resulting problems:

- (1) The image-level *ROC* curve **does not measure the localization performance**. As can be seen from Figure 23a, the validation is performed per image, not per object, therefore not considering whether an object is actually hit (see *Prediction 2*).
- (2) The image-level *ROC* curve is **invariant to the number of annotated objects**. As can be seen from Figure 23b, the curve can not discriminate between a model detecting all objects in an image (*Prediction 1*) or just detecting one object (*Prediction 2*), as long as the largest score is the same across predictions.
- (3) The image-level *ROC* curve is **invariant to the number of detected objects**. As can be seen from Figure 23c, the curve can not discriminate between a model detecting many FP objects in an image (*Prediction 2*) or only detecting one FP (*Prediction 1*), as long as the largest score is the same.

Pitfall: Mismatch image-level classification \leftrightarrow object detection

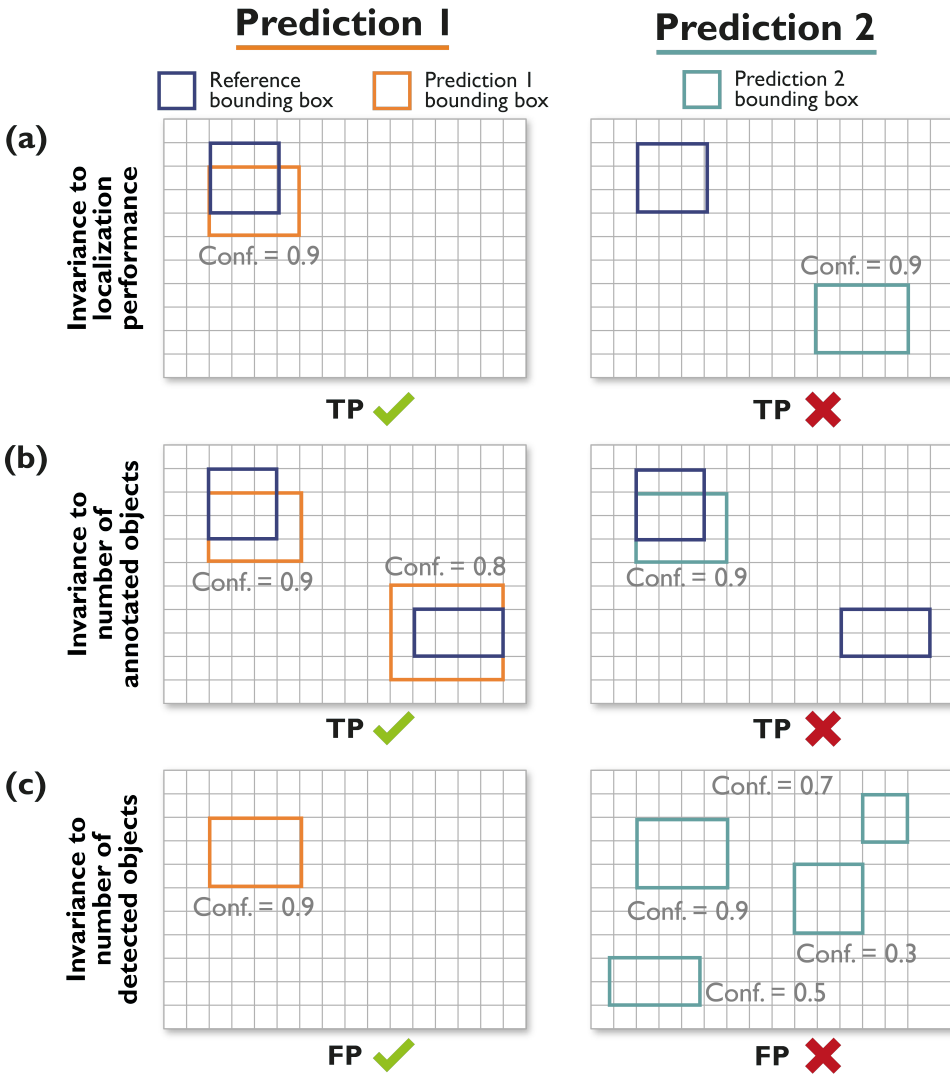
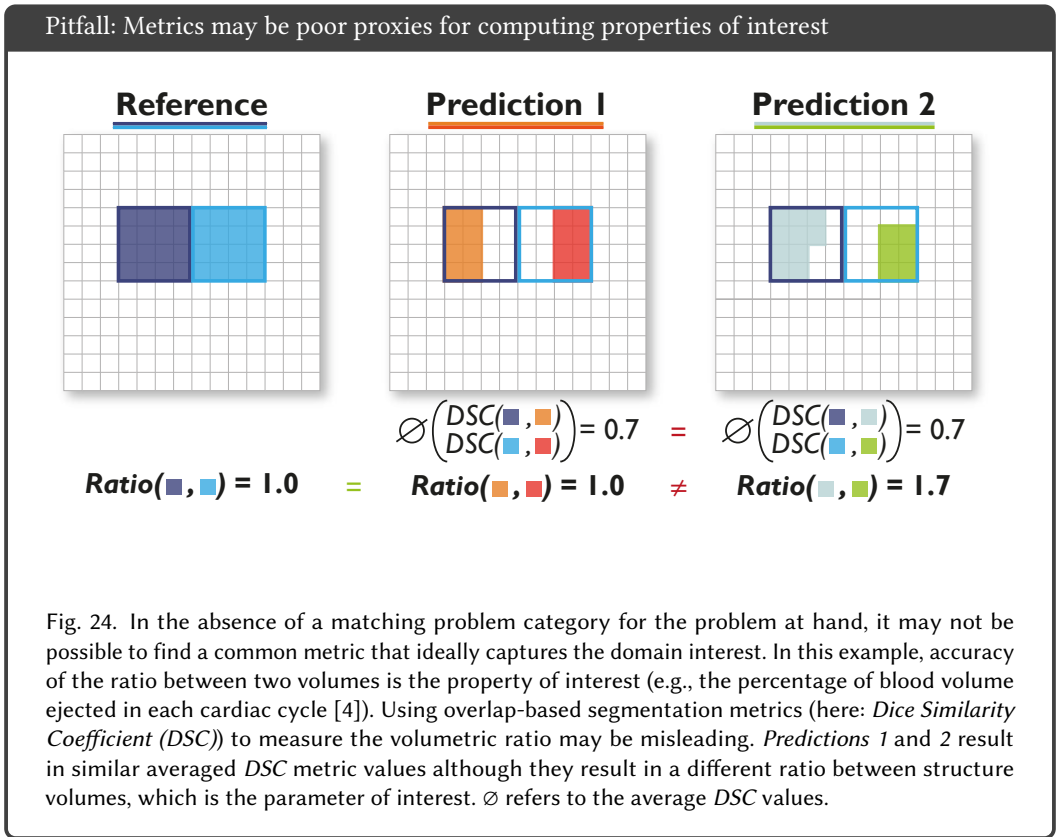


Fig. 23. Image-level classification metrics such as the Area under the Receiver Operating Characteristic curve (AUROC) curve can be used to validate object detection models by first aggregating predictions to one image-level score (per class). This validation scheme discards the information on the object matching (localization, number of objects etc.), which leads to several problems: **(a)** The image-level ROC curve does not measure the localization performance. Both *Prediction 1* and *2* are considered as True Positive (TP) due to their score being very high, although *Prediction 2* is not hitting the annotated object. **(b)** The image-level ROC is invariant to the number of annotated objects in an image. The curve does not discriminate between a model detecting all positives (*Prediction 1*) and a model detecting only one of the positives (*Prediction 2*), as long as the maximum score is the same. **(c)** The image-level ROC is invariant to the number of detections in an image. The curve does not discriminate between a model with many False Positives (FP), (*Prediction 2*) and a model with just one FP (*Prediction 1*), as long as the maximum score is the same. The class probabilities are represented by confidence scores (conf.).

No matching problem category. Metrics should reflect a domain-specific validation goal. This goal may not align with commonly used technical measures like the *DSC*. Figure 24 shows an example with the property of interest being the accuracy of the ratio between two structure volumes, indicating, for example, the percentage of blood volume ejected in each cardiac cycle [4]. Both predictions will result in similar averaged *DSC* scores, although the ratio of the volumes vastly differs. A common segmentation metric thus does not reflect the actual research question in this case.



4 PITFALLS RELATED TO IMAGE-LEVEL CLASSIFICATION

Most issues related to classification metrics are related to one of the following properties of the underlying biomedical problem:

- High class imbalance (Figures 25 - 27)
- Presence of more than two classes (Figure 28)
- Unequal severity of class confusions (Figure 29)
- Unequal handling of classes (Figure 30)
- Interdependencies between classes (Figure 31)
- Lack of stratification (Figure 32)
- Importance of cost-benefit analysis (Figure 33)
- Definition of class labels (Figure 34)
- Prevalence dependency (Figures 35 - 37)
- Importance of confidence awareness (Figures 38 - 41)
- Presence of ordinal classes (Figures 42 - 43)

Furthermore, metric-specific limitations may arise (Figures 44 - 49). Please note that all of these also apply to semantic/instance segmentation or object detection problems. The discourse focuses on the most commonly used image-level classification metrics, as presented in Figs. 4, 5 and 6. For most of the problems, it focuses on the *Accuracy*, *Sensitivity* or *PPV*, because those are the most common metrics for image-level classification in biomedical image analysis. Please note that we do not recommend their indiscriminate use, as they come with limitations (discussed in the following paragraphs), but rather wish to spotlight the problems and pitfalls of those most commonly used metrics.

To preserve the clarity of the illustrations, the most important of the presented metric values may be highlighted with color. Green metric values correspond to a "good" metric value (e.g. a high *Sensitivity* score), whereas red values correspond to a "bad" value (e.g. a low *Sensitivity*). Green check marks indicate desirable behavior of metrics, red crosses indicate undesirable behavior. Please note that a low metric value is not automatically a "bad" score. A metric value should always be put into perspective and compared to inter-rater variability. For simplicity, we still use the terms "good" and "bad/poor" throughout the section. Finally, our illustrations do not provide the concrete class probabilities of the presented classifiers.

High class imbalance. *Accuracy* is one of the commonly applied metrics in classification problems, presumably because it is particularly straightforward to interpret. However, the metric is not designed to handle imbalanced data sets, which often occur across all domains. Figure 25 provides an example in which the positive class (orange circle) is heavily underrepresented. While *Prediction 1* gives a reasonable separation of the classes, *Prediction 2* results in the same *Accuracy* value (0.97) although the algorithm only provides the majority vote as a result. In this specific example, *Sensitivity*, *PPV* and *F1 score* reveal the issue, as does *Matthews correlation coefficient (MCC)*, a metric designed to handle class imbalance which reflects that *Prediction 2* is not better than a random guess (0.00) [15]. As many classification measures are easily computable using the number of TP, TN, FP and FN samples, it is highly recommended to report these TP, TN, FP and FN values explicitly and then compute multiple metrics [36].

Plotting the *ROC* and *PR* curves (Figs. 25b and c) also reveals the limitations of *Prediction 2*, which yields an *AUROC* of 0.52 and *AP* of 0.04, indicating that the prediction is not better than random guessing.

Some metrics inherently address the problem of performance overestimation or distortion caused by class imbalance. *Matthews Correlation Coefficient (MCC)* and *Cohen's Kappa κ* , for example, are designed in such a way that they assign a (prevalence-aware) random guessing algorithm the value 0. Similarly, *Area under the Receiver Operating Characteristic curve (AUROC)* assigns the value 0.5 and *Balanced Accuracy* yields a value of $\frac{1}{C}$, where C is the number of classes. For all other metrics (see Figure 25), it is generally recommended to put the resulting values into perspective of with respect to a (prevalence-aware) random guessing algorithm baseline.

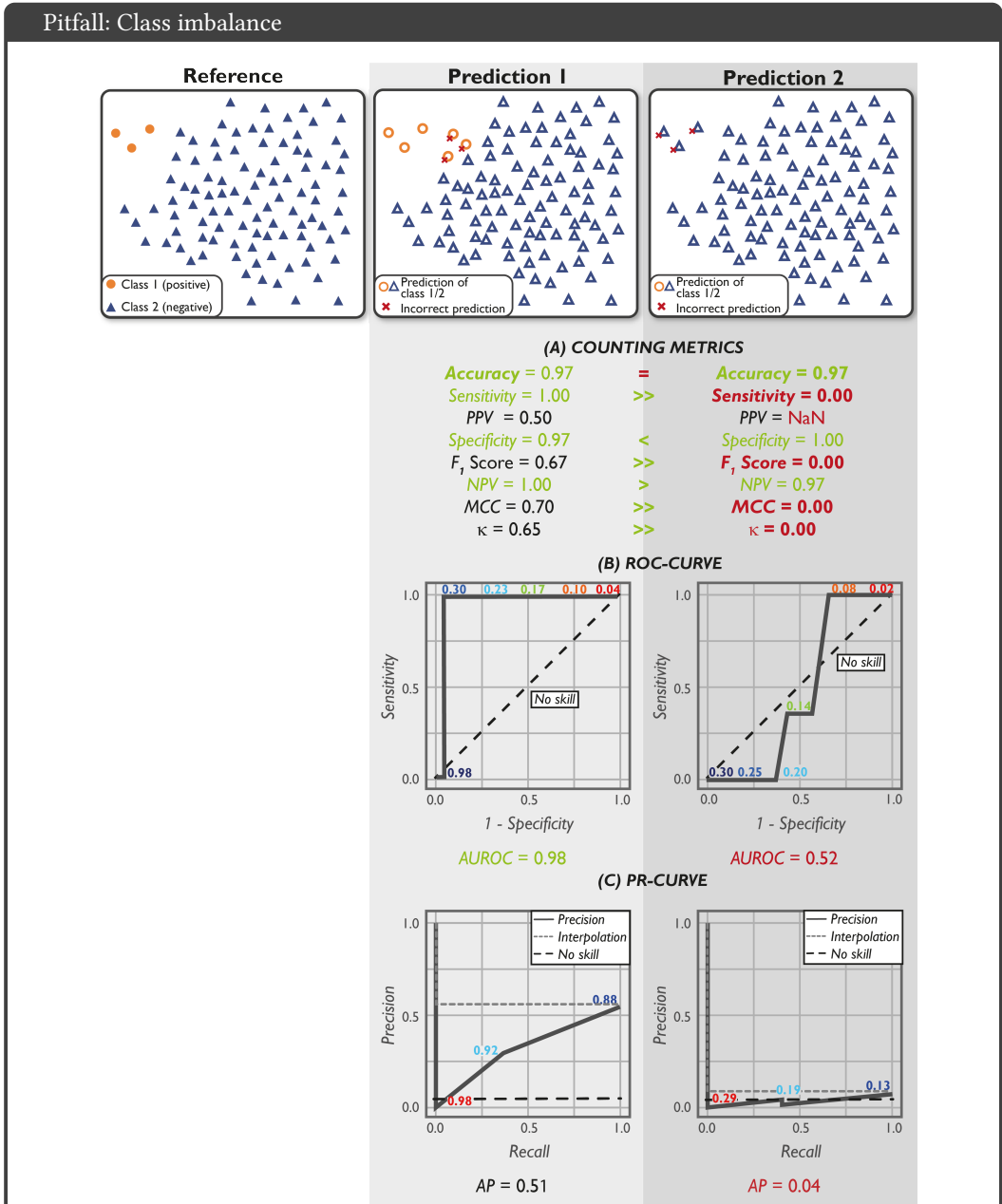


Fig. 25. Effect of class imbalance. Not every metric is designed to reflect class imbalance (e.g. Accuracy). In the case of underrepresented classes, such a metric yields a high value even if the classifier performs very poorly for one of the classes (here: Prediction 2). Multi-threshold metrics, such as the Area under the Receiver Operating Characteristic curve (AUROC) and the Average Precision (AP), reveal the weakness, indicating that Prediction 2 is not better than random guessing. For comparison, a no skill classifier (random guessing) is shown as a black dashed line. For the Precision-Recall (PR) curves, the interpolation applied to compute the AP metric is shown by a dashed grey line. Thresholds used for curve generation are provided as small numbers in the curve. Further abbreviations: Positive Predictive Value (PPV), Negative Predictive Value (NPV), Matthews Correlation Coefficient (MCC), Cohen's Kappa κ .

Given their prevalence invariance (see Figure 36), metrics such as *BA* are a good choice in many scenarios. However, they may be misleading in the case of underrepresented classes (see also use case 2 from [16]). In such a scenario, *BA* yields high scores although the prediction is far from perfect. Here, the *MCC* and *PPV* reveal that the prediction is quite inefficient by assessing predictive values (see Figure 26).

Pitfall: Misleading *BA* for underrepresented classes



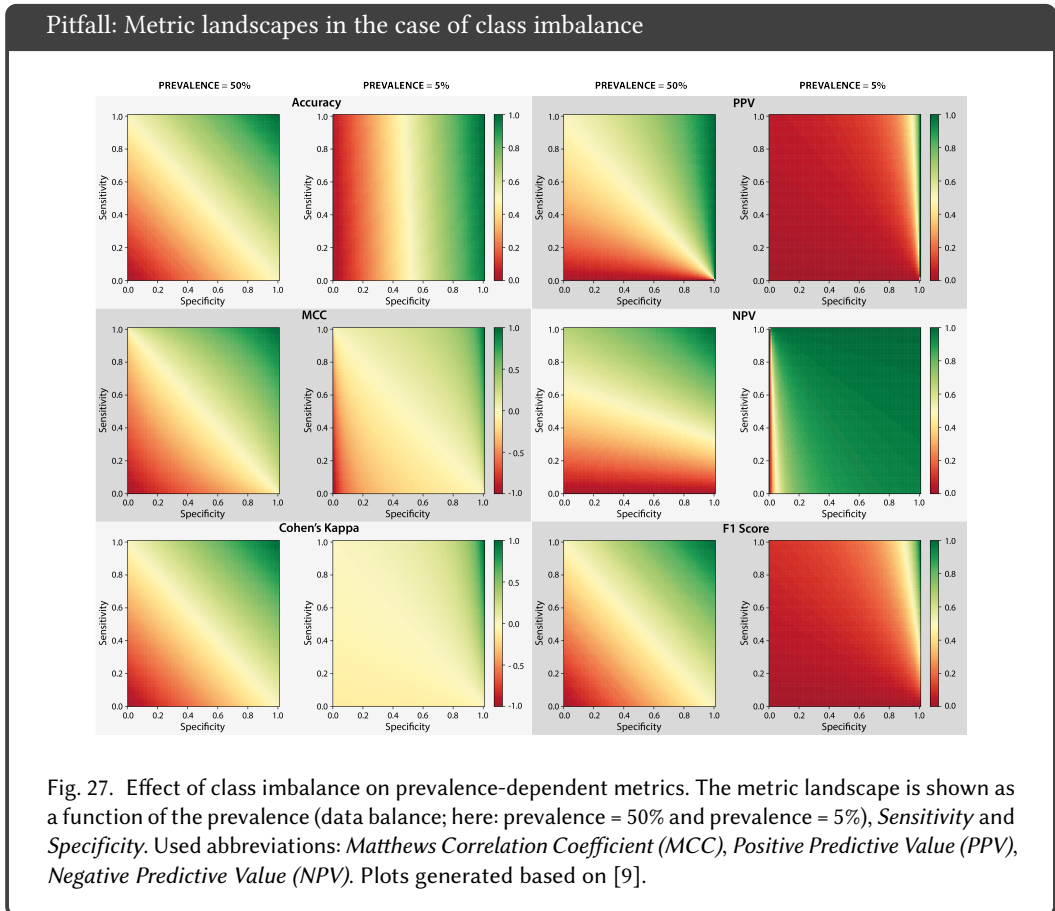
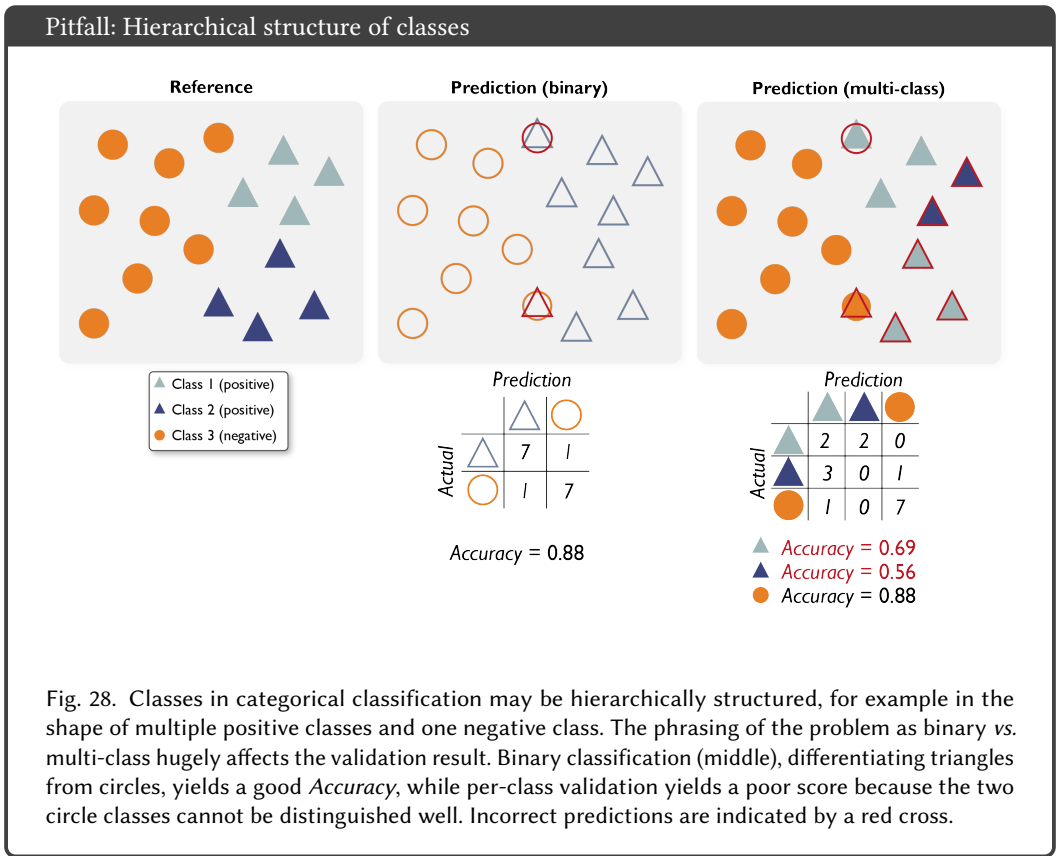
		PREDICTED		
		Positive	Negative	
ACTUAL	Positive	TP 15	FN 5	Accuracy = 0.95 
	Negative	FP 4,980	TN 95,000	BA = 0.85 PPV = 0.00 MCC = 0.05 

Fig. 26. In the case of underrepresented classes, common metrics may yield misleading values. In the given example, Accuracy and *Balanced Accuracy (BA)* have a high score despite the high amount of False Positive (FP) samples. The class imbalance is only uncovered by metrics considering predictive values (here: *Positive Predictive Value (PPV)* and *Matthews Correlation Coefficient (MCC)*).

Prevalence-dependent metrics yield different metric scores for imbalanced data sets. Figure 27 shows the metric landscapes for a balanced data set, meaning a prevalence of 50%, in comparison to those for imbalanced data (prevalence of 5%) [9].

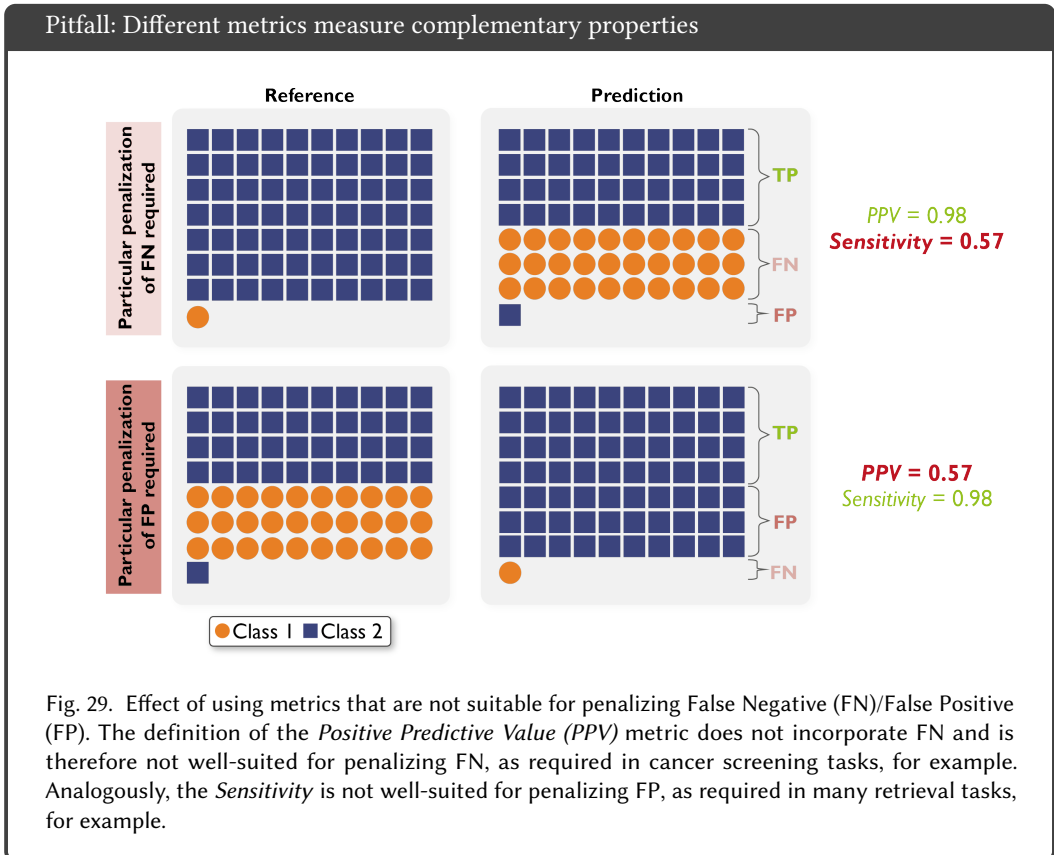


More than two classes available. Many binary metrics can directly be translated to the multi-class case by expanding the confusion matrix to all classes. These classes are often hierarchically structured, for example in the shape of one negative class (e.g. no pathology) and multiple positive classes (e.g. different types of pathologies). Figure 28 shows an example of a classification into triangles and circles, for which the circle class is further separated into two distinct classes (green and orange). The binary performance into triangle vs. circle, shown in the middle, is good (*Accuracy* of 0.88). But when considering the three classes separately, the prediction struggles to identify the color of the circles, causing their per-class accuracy scores to drop significantly.



Unequal severity of class confusions. In biomedical applications, classes are often not equally important. Consider the task of colon polyp detection in the gastrointestinal tract, for example. To provide the patient with the best care, it is crucial to detect all of these precancerous lesions. This requires a particular penalization of those samples containing a polyp which have been marked as 'no polyp' (FN), and the metrics need to be chosen accordingly. The *PPV*, for example, does not include the FN in its definition, hence would not be appropriate for this research question. *Sensitivity*, on the other hand, would show the desired poor performance in the presence of many FN predictions, as seen in the top row of Figure 29.

For image retrieval, the task of finding images for a specific content, it is not important to find every single existing image, but the images found should be correct. In this setting, the FP (assigning an incorrect image as correct) need to be penalized. Since it includes the computation of FP, in this case, the *PPV* would be a good metric. In contrast, *Sensitivity* does not consider FP, therefore being inappropriate in this context (see bottom row of Figure 29). Penalization in both cases is especially important in cases of imbalanced data sets (see Figure 25).



Unequal handling of classes. When it comes to multi-class problems, different approaches may be chosen to compute the metric values. One possibility is to first compute the metric values per class and aggregate them subsequently. Special care has to be taken in the case of unequal importance of the different classes. For example, identifying whether a patient harbors a pathology in general might be more important than identifying the specific type of pathology. In this case, one should not just average over all class metric scores, but instead apply a sufficient weighting scheme. In the example of Figure 30, the triangle class is the most important class but also the one with the lowest per-class Accuracy. Simple averaging, so-called macro-averaging, would ignore that property and thus result in a higher aggregated Accuracy than merited. This effect can be compensated with the *Weighted Accuracy*.

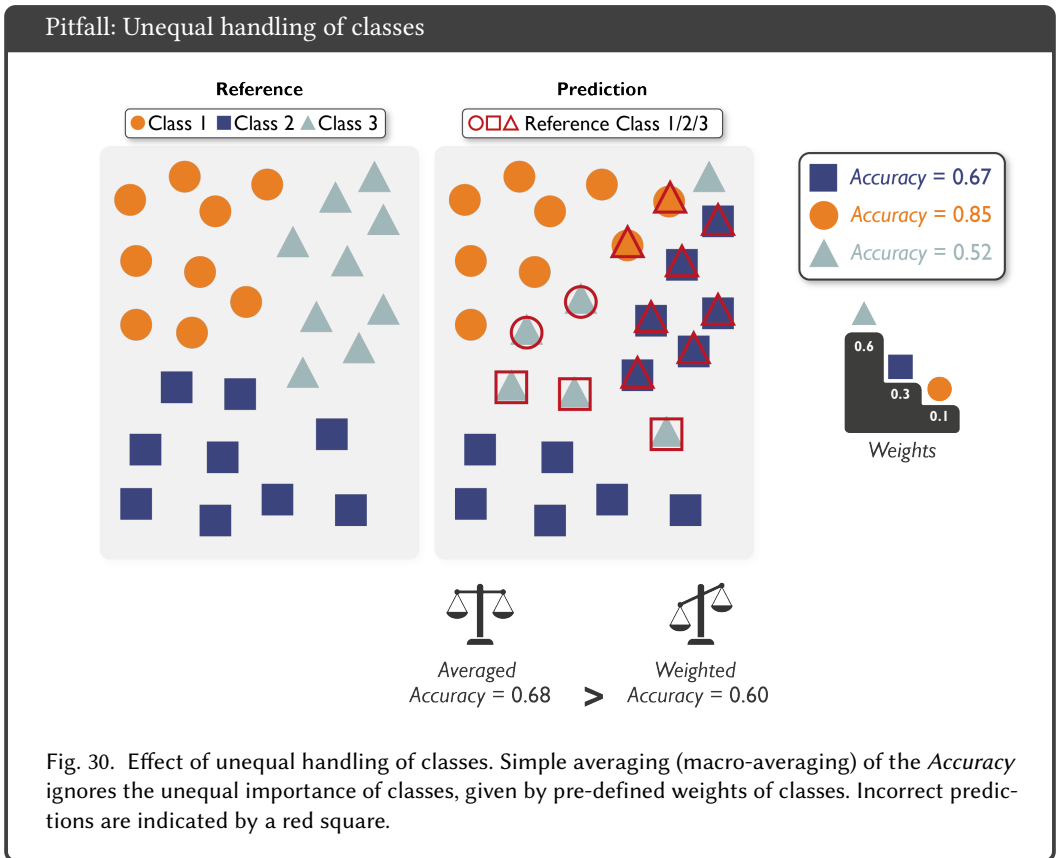
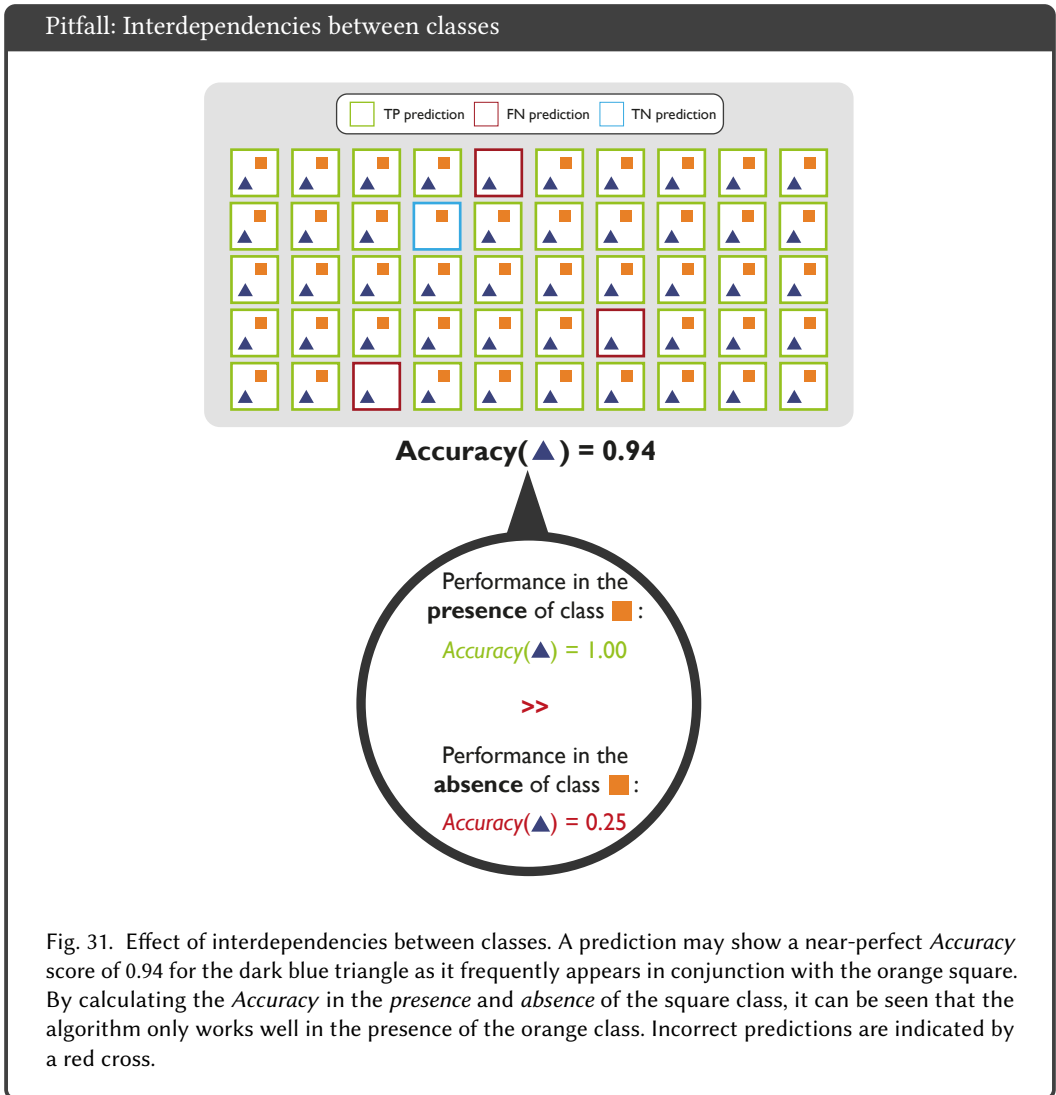
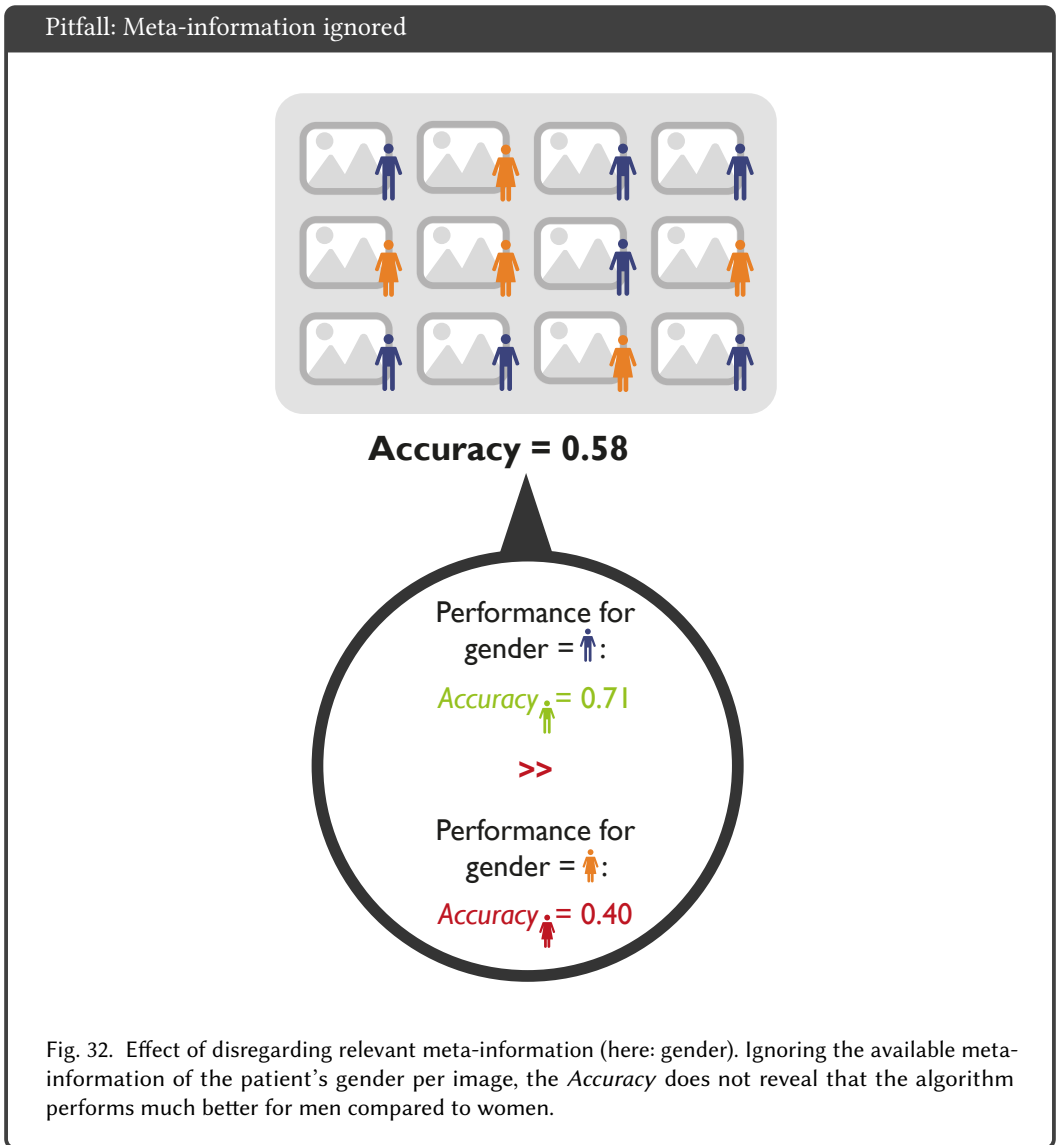


Fig. 30. Effect of unequal handling of classes. Simple averaging (macro-averaging) of the Accuracy ignores the unequal importance of classes, given by pre-defined weights of classes. Incorrect predictions are indicated by a red square.

Interdependencies between classes. If multiple classes are visible in the data set, one should carefully account for interdependencies between the classes. Interdependencies can happen in cases of multi-colinearities in which two classes are correlated, either inherently, such as for the body mass index (BMI) and the body fat percentage, or in the case of dependent data settings, for example multiple images per patient or the presence of confounders. An algorithm aiming to classify the dark blue triangle class in Figure 31 may result in a nearly perfect *Accuracy* of 0.94, but only because the dark blue triangle almost always appears in conjunction with the orange square. Computing the *Accuracy* for those images individually without the square class would lead to a much lower performance.



Stratification based on meta-information. Different kinds of meta-information may be available for a data set, including the presence and relevance of artifacts or artificial structures (e.g. metal artifacts in CT images or text overlay in endoscopic data) as well as specifics of acquisition protocols (e.g. acquisition angle or viewpoint) or grid size (cf. Figure 65). Another typical example is the gender of a patient, as shown in Figure 32. In this case, the *Accuracy* is computed over twelve cases, disregarding the available meta-information (gender). Stratification based on gender will reveal that the prediction performs much worse for women compared to men. These aspects are currently investigated in the fairness literature [5].



Importance of cost-benefit analysis. Most common performance metrics fall short when it comes to determining whether an algorithm can lead to improved clinical decisions. Knowing that an algorithm performs well in terms of calibration, discrimination, and accuracy, for instance, does not necessarily imply that decisions guided by the algorithm will lead to improved clinical outcomes. Motivated by the idea of taking into account the tradeoff between the benefit resulting from the detection of a TP case and the cost of a FP, a risk threshold should be defined for a specific prediction problem. Net Benefit (NB) is a metric that incorporates the tradeoff between costs and benefits resulting from the selection of a specific risk threshold in the validation of an algorithm, and thus facilitates informed medical decision-making [88]. In Figure 33, we present a similar example as the one presented by [88]. In this example, nine unnecessary biopsies are deemed acceptable to detect one lesion, resulting in an exchange rate of 1:9. Two scenarios are to be considered here. On the one hand, applying the biopsy to every patient would ensure that all patients with the disease receive a biopsy (benefit) but also result in 75 patients with no disease undergoing biopsy (harm). On the other hand, a marker-based biopsy decision would result in only 20 patients with the disease undergoing biopsy, thus missing 15 of them, while reducing the number of unnecessarily biopsied healthy patients to 60. Only considering the Accuracy would rate both scenarios similarly. However, incorporating the cost-benefit analysis and the resulting exchange rate, NB would indicate that performing biopsy on all patients yields better clinical outcome. Please note that defining risk cutoffs and exchange rates is highly subjective. This is why NB is often considered over various thresholds.

Common metrics disregard cost-benefit analysis

Cost-benefit analysis:
~9 unnecessary biopsies for one detected lesion are acceptable.



1) BIOPSY IN ALL PATIENTS:

		PREDICTED	
		Positive	Negative
ACTUAL	Positive	TP 30	FN 0
	Negative	FP 75	TN 0

Accuracy = 0.29

BUT
75 unnecessary biopsies (FP)

2) MARKER-BASED DECISION ON BIOPSY

		PREDICTED	
		Positive	Negative
ACTUAL	Positive	TP 20	FN 15
	Negative	FP 60	TN 10

Accuracy = 0.29

BUT
60 unnecessary biopsies (FP)

=



NB metrics relate the benefits of TPs with the cost of FPs by incorporating an exchange rate (here: 1/9 based on benefit-cost analysis)

NB = 0.21

>

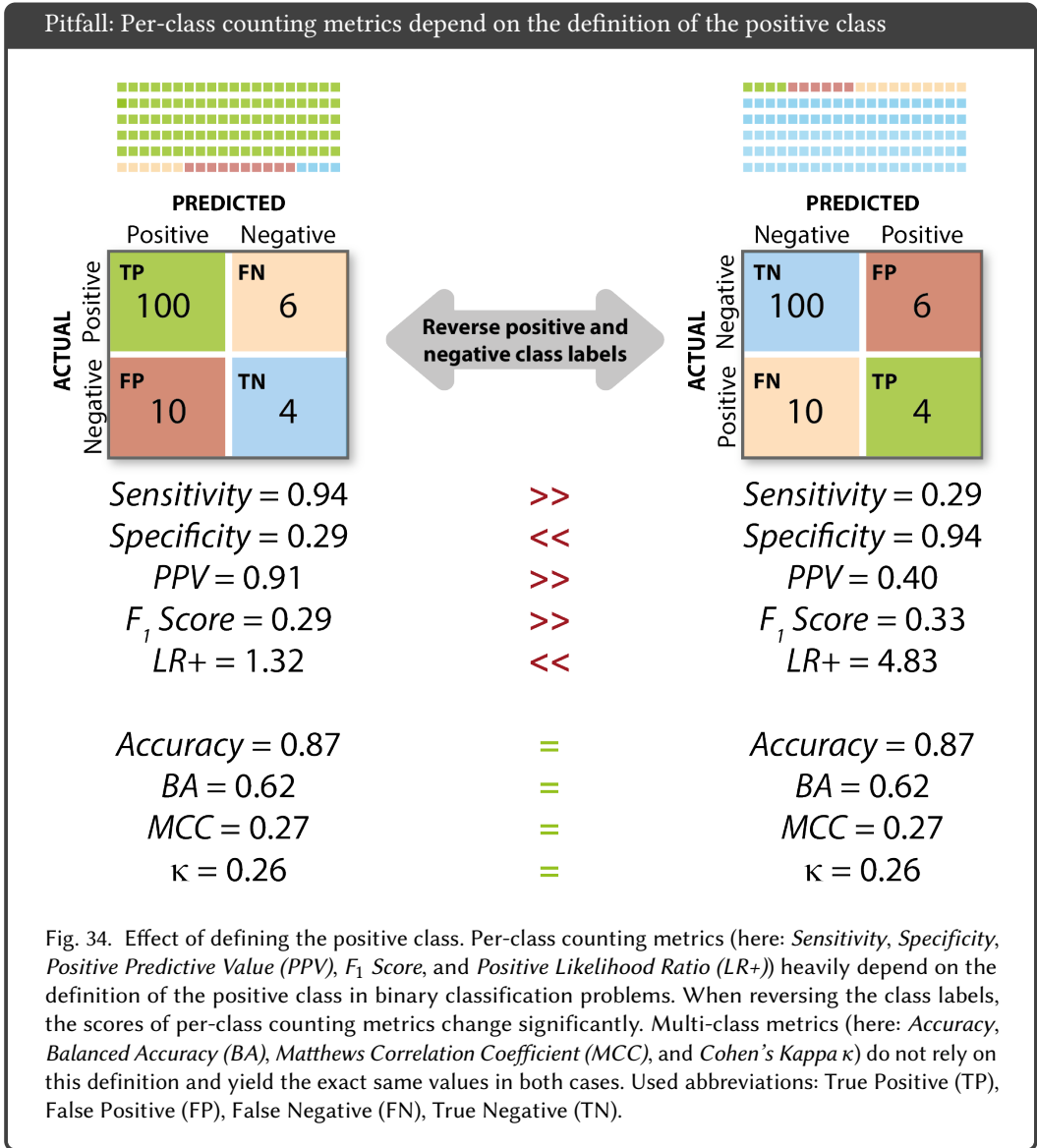
NB = 0.13

Same Accuracy, but
better clinical utility

Same Accuracy, but
poorer clinical utility

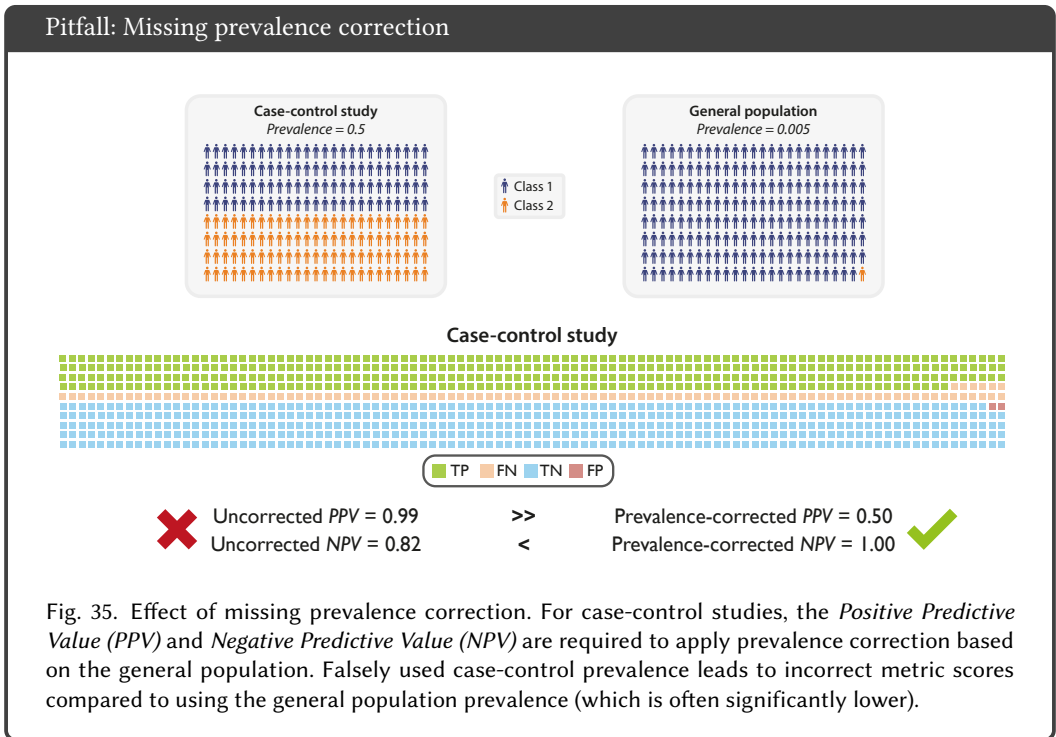
Fig. 33. Effect of neglecting a cost-benefit analysis. In a cost-benefit analysis, clinicians are able to define a risk-specific exchange rate to be used in the computation of the *Net Benefit (NB)* metric. Common metrics such as the Accuracy do not include this analysis and would rate both decision types similarly, while *NB* indicates that having all patients undergo biopsy actually yields a better clinical outcome [88].

Definition of class labels. Binary classification problems typically involve the step of defining one class as positive and the other as negative. The final scores of per-class counting metrics rely on the definition of the positive class. Figure 34 shows an example in which the class labels are reversed in the same data set. The scores of per-class counting metrics dramatically change when the class labels are switched. On the other hand, multi-class counting metrics remain stable as they rely on the entire confusion matrix and are invariant to changes in the class labels.



Prevalence dependency. The *PPV* and the *Negative Predictive Value (NPV)* are common measures to validate classification performances. In many cases, binary classification is considered, for example presence or absence of a disease. In contrast to *Sensitivity* and *Specificity*, in case-control studies, *PPV* and *NPV* should be seen as the conditional probability of a disease being present based on a test result and the prevalence in a general population [62].

However, *PPV* and *NPV* are frequently used incorrectly. This is due to the fact that many practitioners assume the same prevalence in an analyzed case-control study group as in the general population. However, a study group is often heavily biased, either due to the study design or due to the observation of patient groups from specialized clinics. Thus, the assumed disease prevalence in scientific literature is often higher than that found in the general population (cf. Figure 35). This problem is amplified by default implementations (e.g. in *scipy* [89]) which disregard wider population prevalence and calculate prevalence from the study group. Without prevalence correction, this can lead to misleading results, confusion among patients and ill-informed policy-making.



Metrics depending on the prevalence cannot easily be compared across data sets with different prevalences, as shown in Figure 36. Here, two situations with the same *Sensitivity* and *Specificity* values but with different prevalences (50% vs. 90%) are presented. Only metrics that do not rely on the prevalence (such as *BA* and *EC*) can be used for a comparison across data sets.

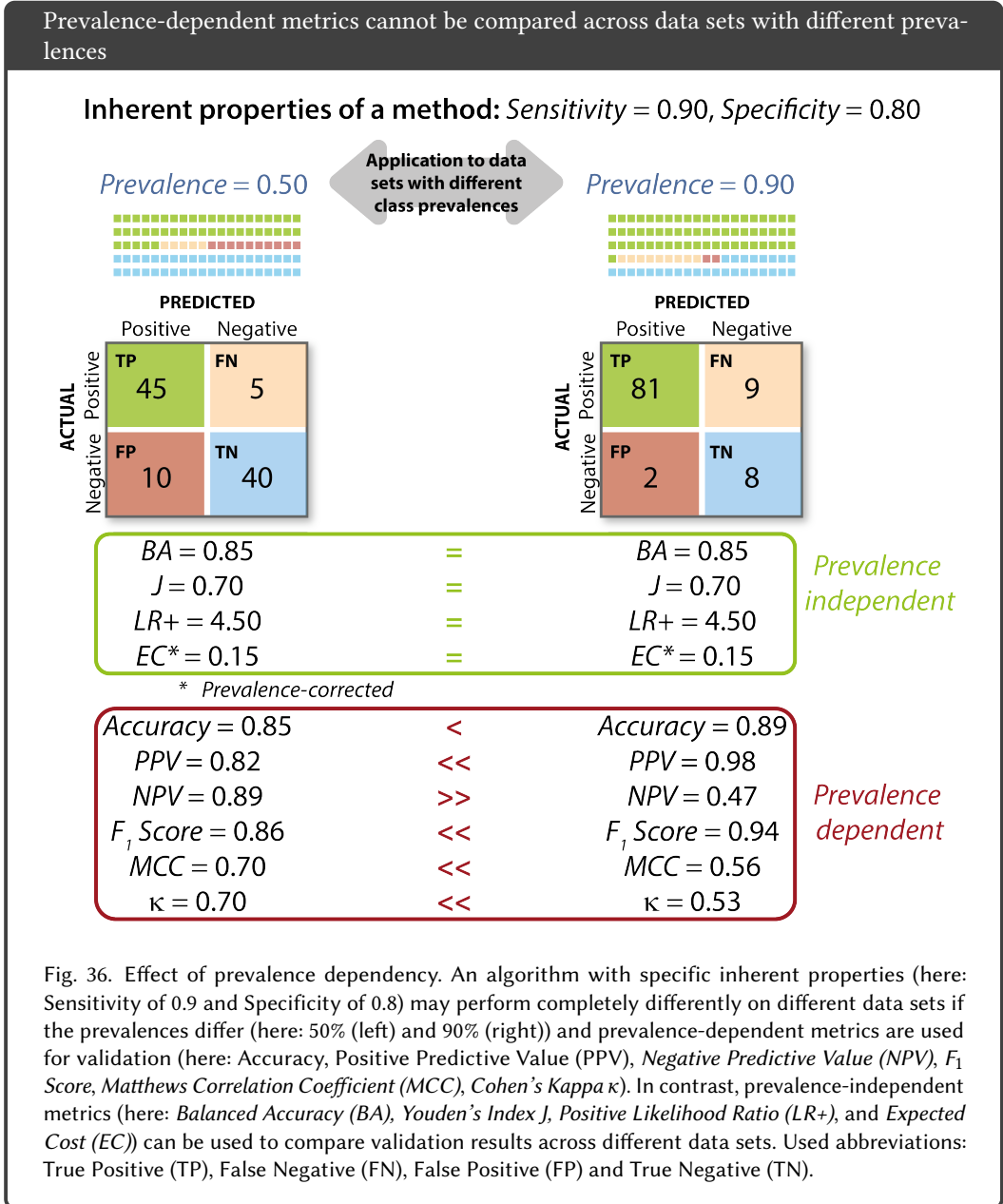


Fig. 36. Effect of prevalence dependency. An algorithm with specific inherent properties (here: *Sensitivity* of 0.9 and *Specificity* of 0.8) may perform completely differently on different data sets if the prevalences differ (here: 50% (left) and 90% (right)) and prevalence-dependent metrics are used for validation (here: *Accuracy*, *Positive Predictive Value (PPV)*, *Negative Predictive Value (NPV)*, *F₁ Score*, *Matthews Correlation Coefficient (MCC)*, *Cohen's Kappa κ*). In contrast, prevalence-independent metrics (here: *Balanced Accuracy (BA)*, *Youden's Index J*, *Positive Likelihood Ratio (LR+)*, and *Expected Cost (EC)*) can be used to compare validation results across different data sets. Used abbreviations: *True Positive (TP)*, *False Negative (FN)*, *False Positive (FP)* and *True Negative (TN)*.

For a prevalence unequal to 50%, *BA* and *Youden's Index J* may lead to different rankings compared to *MCC* and *Cohen's Kappa κ* [16], as illustrated in Figure 37. In this example, predictions for three different prevalences (50%, 40% and 60%) are shown. Only in the case of a 50% prevalence will the rankings generated by all metrics be the same, with all preferring *Prediction 2*. For different prevalences, rankings may differ: While *BA* and *Youden's Index J* prefer *Prediction 2* over *Prediction 1*, *MCC* and *Cohen's Kappa κ* favor the *Prediction 1*.

Pitfall: Rankings in the case of prevalence dependency

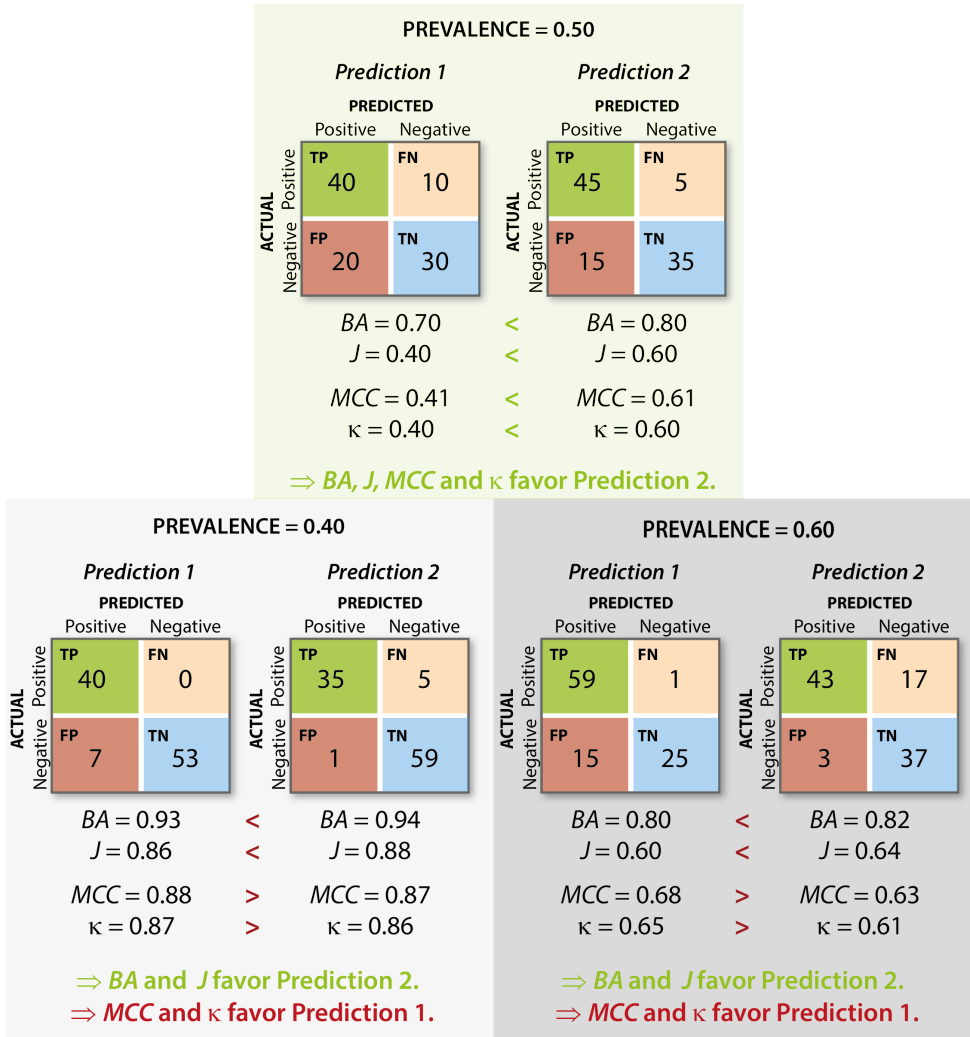


Fig. 37. Effect of prevalence dependency on rankings. For a prevalence unequal to 0.5, the rankings generated by *Balanced Accuracy* (BA) and *Youden's Index J* (J) (here preferring Prediction 2 over Prediction 1) differ from those generated by *Matthews Correlation Coefficient* (MCC) and *Cohen's Kappa* κ (preferring Prediction 1 over Prediction 1). Rankings will only be the same for a prevalence of 0.5 (favoring Prediction 2). Used abbreviations: True Positive (TP), False Negative (FN), False Positive (FP) and True Negative (TN).

Discrimination vs. calibration. A model's *discrimination* capability refers to how well it separates samples with and without the class of interest. If all predicted class scores for the samples with the class of interest are higher than for the others, the model discriminates perfectly, reflected in an AUROC score of 1. A *calibrated model* outputs predicted class scores that match the empirical success rate (e.g. outputs with score 0.8 for a specific class, empirically belong to this class in 80% of the cases) [17]. However, it may happen a perfectly discriminating model, such as the one presented in Figure 38, is not well calibrated. The *Prediction* gives a confidence score of 0.52 for all samples of the positive class (orange circle) and a score of 0.51 for all samples of the negative class (blue triangle). Although this leads to a perfect discrimination, the calibration is very poor and the predicted probabilities would not be helpful in practice at all.

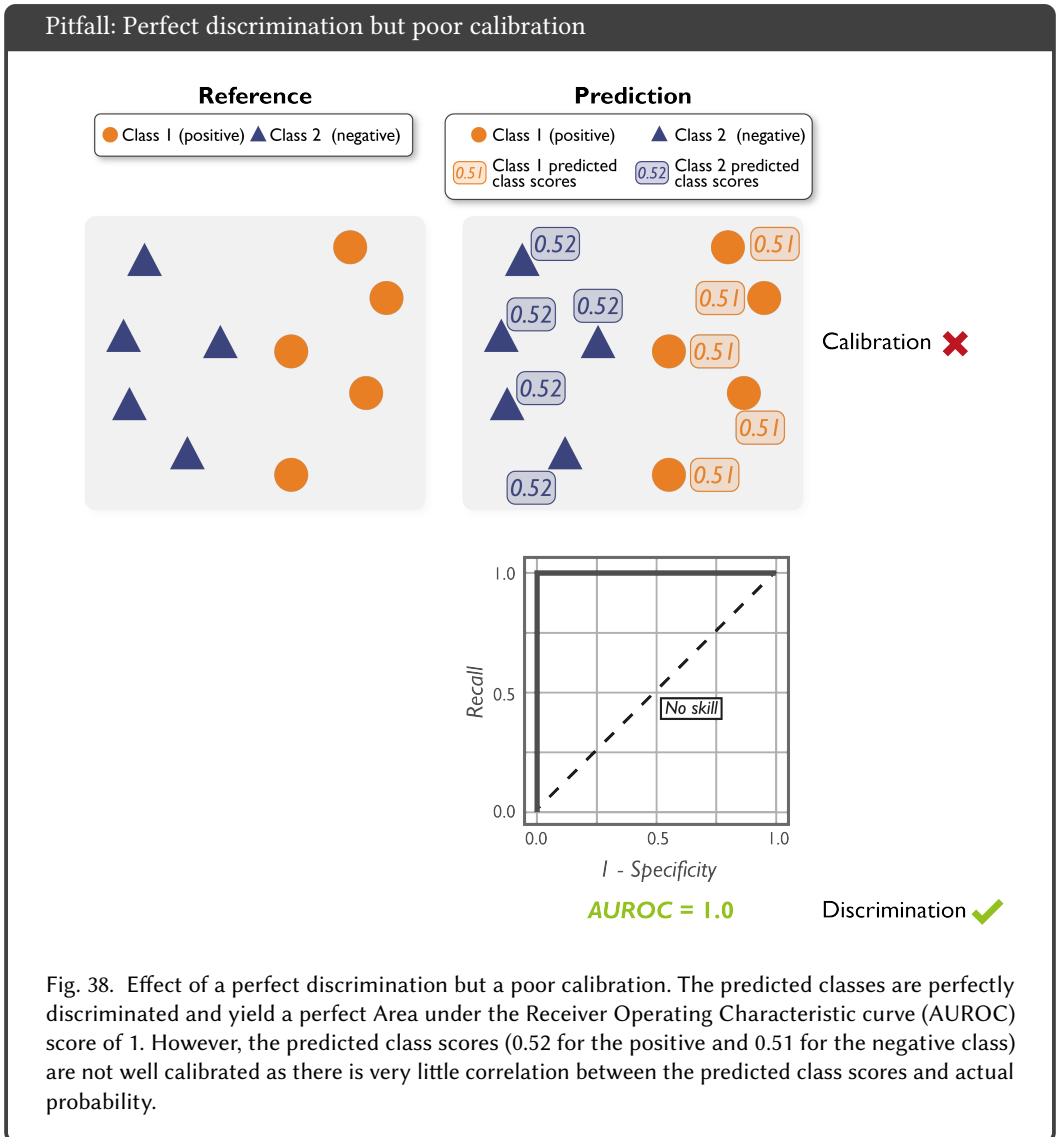
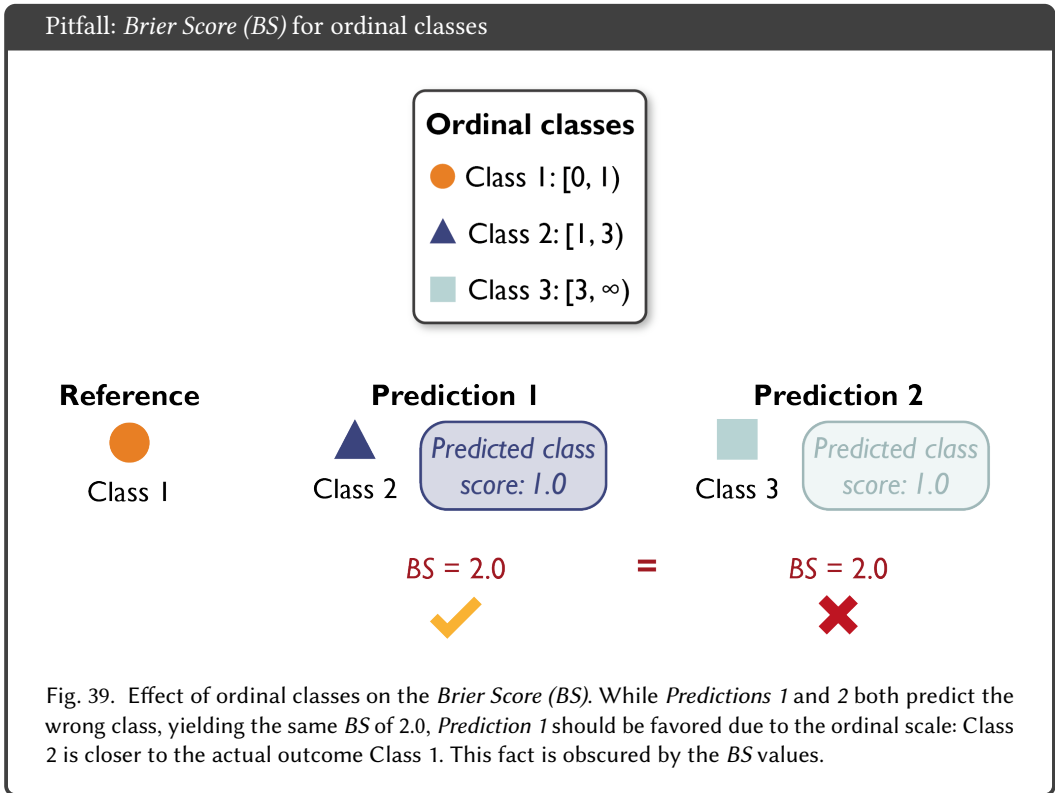


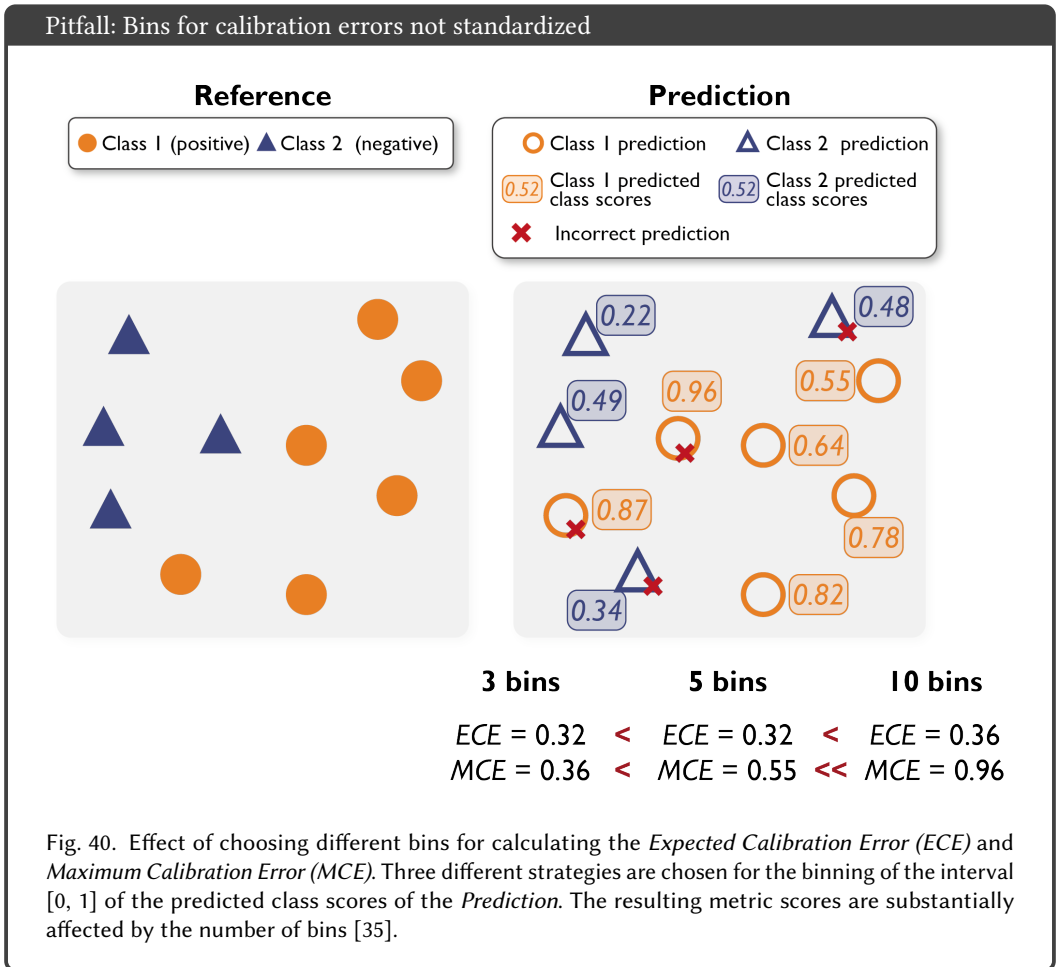
Fig. 38. Effect of a perfect discrimination but a poor calibration. The predicted classes are perfectly discriminated and yield a perfect Area under the Receiver Operating Characteristic curve (AUROC) score of 1. However, the predicted class scores (0.52 for the positive and 0.51 for the negative class) are not well calibrated as there is very little correlation between the predicted class scores and actual probability.

Similarly to standard validation metric measuring the discrimination power of algorithms, calibration metrics come with limitations. For example, the *BS* [7, 29] is defined as the squared difference between a predicted class score f_t and the actual outcome o_t for one of n events t , typically defined as 1 if the event occurred and 0 otherwise.

However, the *BS* should be used with caution in the case of ordinal classes, in which the classes underlie an order, such as in the example in Figure 39. Here, three classes are present which denote patient survival times in years. The first class refers to zero to one year, the second class to two to three years, and the third class denotes a survival time of three or more years. While the actual survival is zero to one year (class 1; orange circle), *Predictions 1* and *2* are predicting classes 2 (blue triangle) and 3 (green square), both with a probability of 100%. Although both predictions are incorrect, *Prediction 1* would be preferable given the ordinal scale of variables: The predicted time frame of one to two years of survival time is closer to the actual survival time of zero to one year than that of *Prediction 2*. However, both predictions would yield the same *BS*.



Calibration errors [34], on the other hand, compute the difference between the accuracy of a prediction and the average predicted class scores. Classifier outputs are generally continuous, which often reduces the number of available samples per prediction to one. Strategies for alleviating the sparse sampling problem include binning the continuous scale [57], as done by the *ECE* and *MCE* [34, 63]. However, the binning itself is not strictly defined, neither in regard to whether the bins should be equidistant nor in the number of bins. Depending on the binning strategy, the scores of the *ECE* and *MCE* will differ, as shown for the example in Figure 40.



Calibration can be defined on different levels. While top-label and class-wise calibration only consider certain parts of the predicted class score vectors, solely the canonical definition of calibration computes the calibration errors based on the full probability vectors. As shown in Figure 41(a), the Calibration Error (CE) may imply a perfect calibration although the prediction is not perfectly calibrated, as indicated by the canonical CE [33, 85]. Moreover, the CE depends on the sample size [33]. Although a model may be perfectly calibrated, the ECE only converges towards a perfect score with an increasing number of data samples, as shown in Figure 41(b).

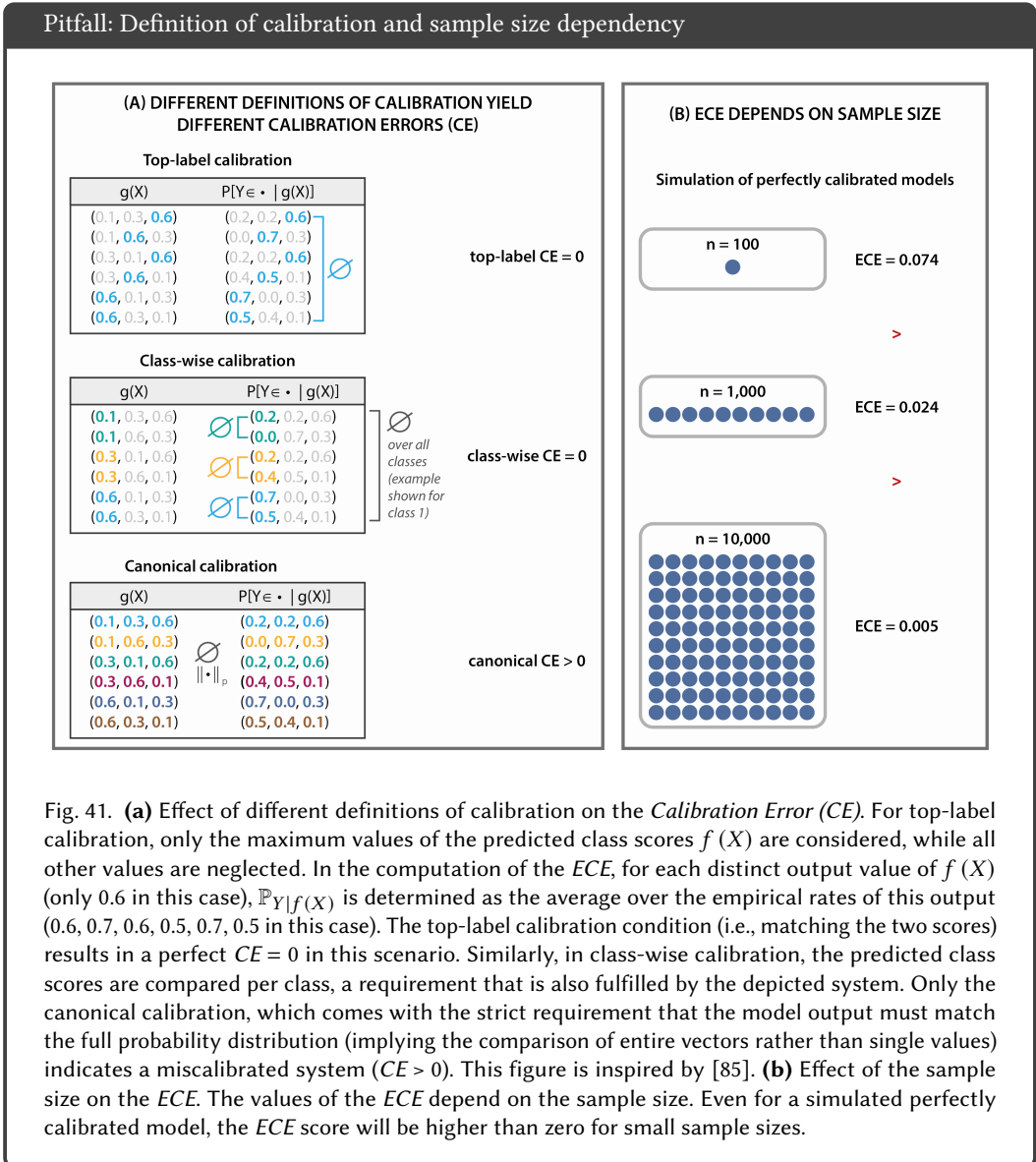
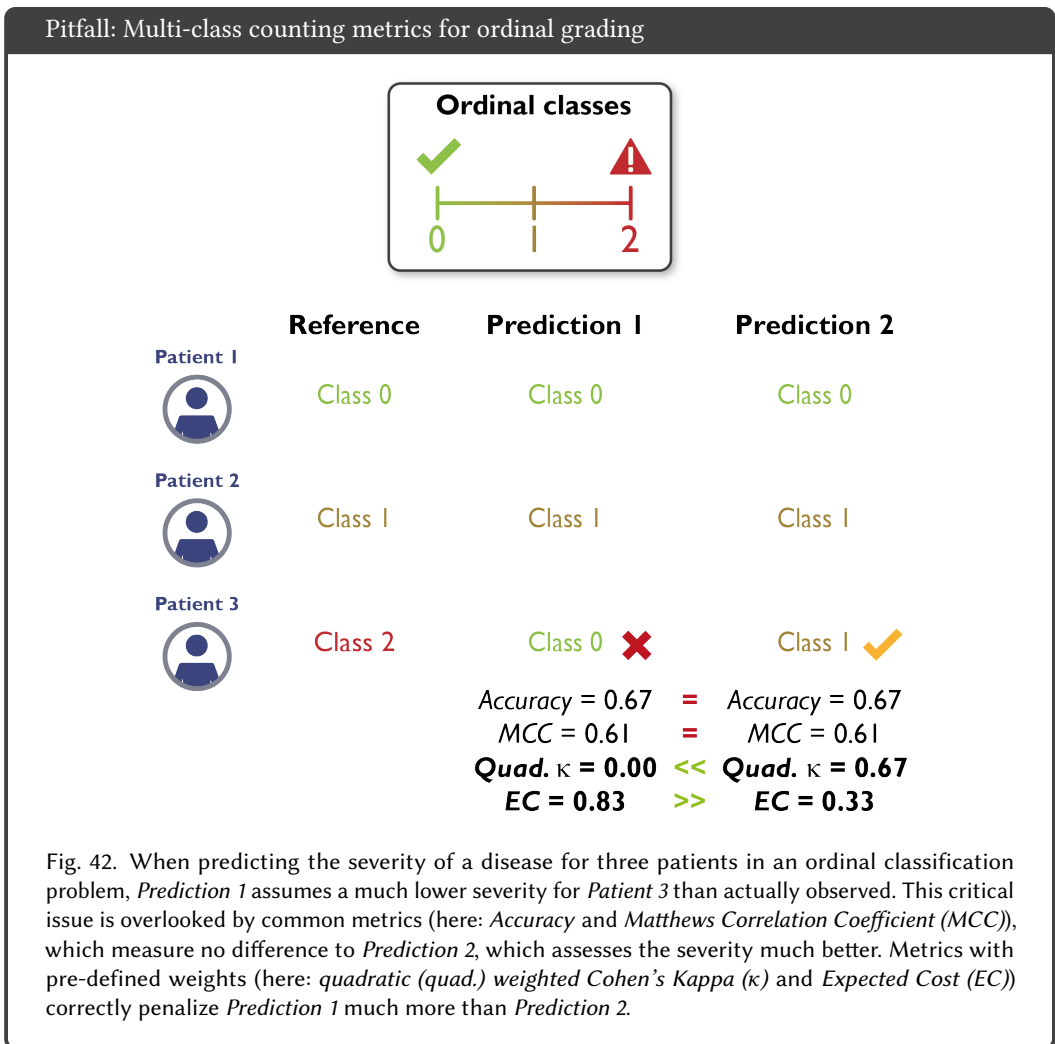
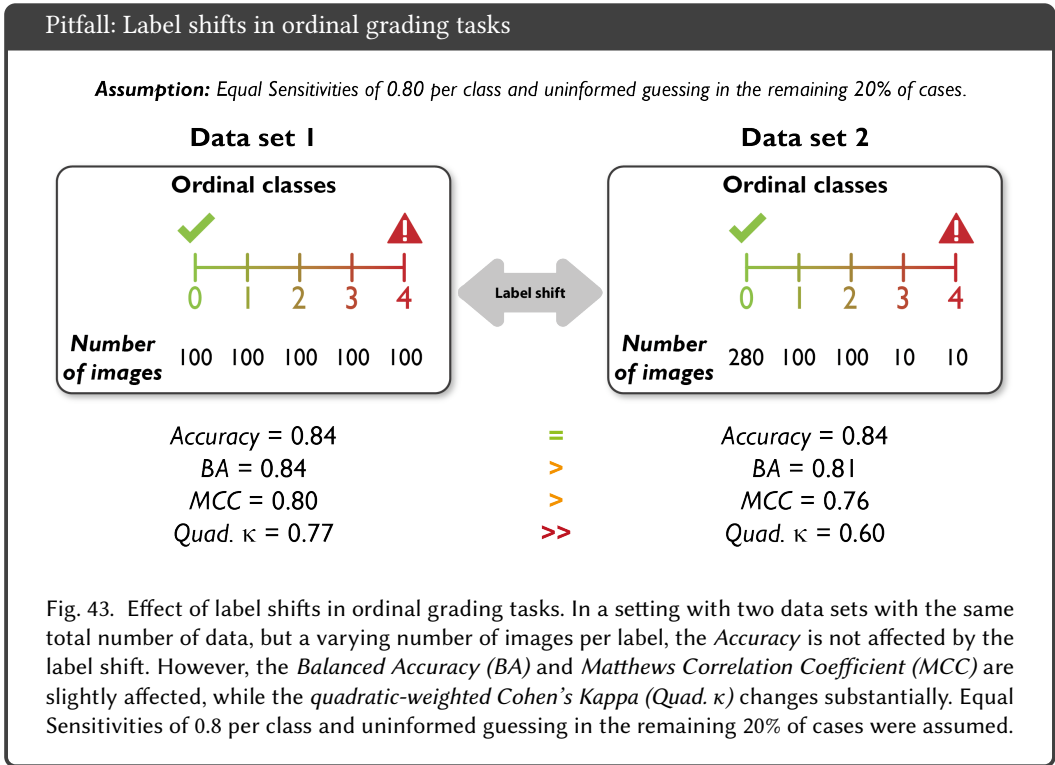


Fig. 41. **(a)** Effect of different definitions of calibration on the Calibration Error (CE). For top-label calibration, only the maximum values of the predicted class scores $f(X)$ are considered, while all other values are neglected. In the computation of the ECE, for each distinct output value of $f(X)$ (only 0.6 in this case), $\mathbb{P}_{Y|f(X)}$ is determined as the average over the empirical rates of this output (0.6, 0.7, 0.6, 0.5, 0.7, 0.5 in this case). The top-label calibration condition (i.e., matching the two scores) results in a perfect CE = 0 in this scenario. Similarly, in class-wise calibration, the predicted class scores are compared per class, a requirement that is also fulfilled by the depicted system. Only the canonical calibration, which comes with the strict requirement that the model output must match the full probability distribution (implying the comparison of entire vectors rather than single values) indicates a miscalibrated system (CE > 0). This figure is inspired by [85]. **(b)** Effect of the sample size on the ECE. The values of the ECE depend on the sample size. Even for a simulated perfectly calibrated model, the ECE score will be higher than zero for small sample sizes.

Classification metrics in the case of ordinal classes. In the case of ordinal classes, similarly to calibration metrics, the scores of classification metrics should be interpreted with caution, as shown in Figure 39. The classification or grading of patients according to a scale of disease severity would be a typical use case. In Figure 42, the severity of the disease is given by three classes, with class 0 denoting the lowest severity and class 2 the highest. *Predictions 1* and *2* agree in the grading of the first four patients. However, *Prediction 1* classifies *Patient 3* into the lowest severity, and thus performs much more poorly than *Prediction 2*, which is only one class of severity below the reference. However, both *Accuracy* and *MCC* do not spot this difference. Underestimating the severity of disease in a patient, however, would lead to serious consequences in clinical practice and thus needs to be heavily penalized. Only metrics with pre-defined weights would highly penalize *Prediction 1* (here: *EC* and *quadratic-weighted Cohen’s Kappa*).



Label shift in the case of ordinal classes. In ordinal class scenarios, one should also be aware of potential label shifts, in which the distribution or number of labels changes over time or data sets [93]. Figure 43 shows the metric scores for two data sets with the same labels and same number of data, but a differing number of images per label. While *Data set 1* is balanced, *Data set 2* underwent a label shift with different per-class prevalences. While the *Accuracy* values do not change, the *BA* and *MCC* are slightly affected by the label shift. The most dramatic change is observed for the *quadratic-weighted Cohen’s Kappa*, with a drop of 0.17 after label shift. Thus, when comparing the performance of a model on data sets with varied regional or temporal origins, one should take precautions when utilizing the *quadratic-weighted Cohen’s Kappa*⁸.



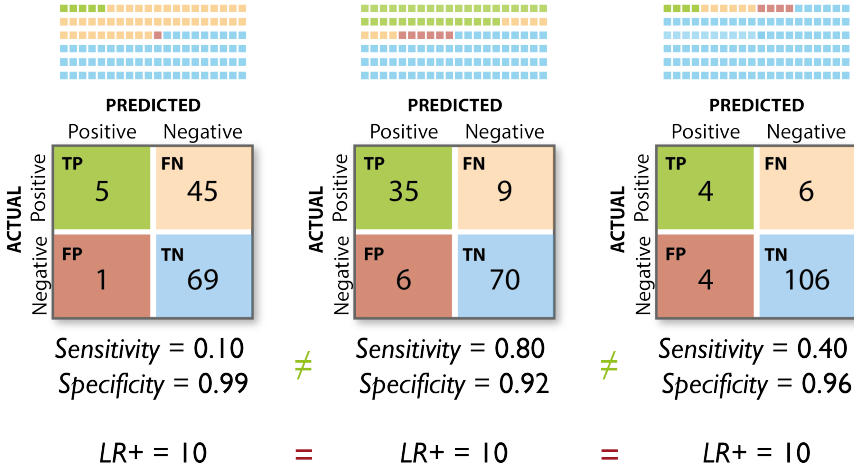
Same metric values for different confusion matrices. Per definition, the *LR+*, *Youden Index J* and *BA* are calculated from *Sensitivity* and *Specificity*. However, the exact same *LR+* or *BA* values can occur for very different specifications of the confusion matrix. Figure 44a shows three examples of predictions, yielding quite different confusion matrices. For example, the leftmost prediction shows a very high number of *TNs* and *FNs*, while the prediction in the middle only has very few false predictions. The prediction on the right correctly classifies most of the negative samples. Despite the different *Sensitivity* and *Specificity* values, *LR+* will be the same for all three examples [25]. The same can occur for the *BA*, as shown in Figure 44b. In both cases, the substantial differences between the predictions remain hidden unless *Sensitivity* and *Specificity* are reported in

⁸Equal Sensitivities of 0.8 per class and uninformed guessing in the remaining 20% of cases were assumed. See https://github.com/agaldran/kappa_pitfall/blob/main/kappa_pitfall.ipynb for details.

addition. Similar issues hold true for other metrics that rely on multiple measures. An AUROC of 0.9, for example, may correspond to various appearances of the ROC curve, and various underlying distributions of positive and negative samples and predictions [90].

Pitfall: Same metric scores for different confusion matrices

(a) LR+



(b) BA and J

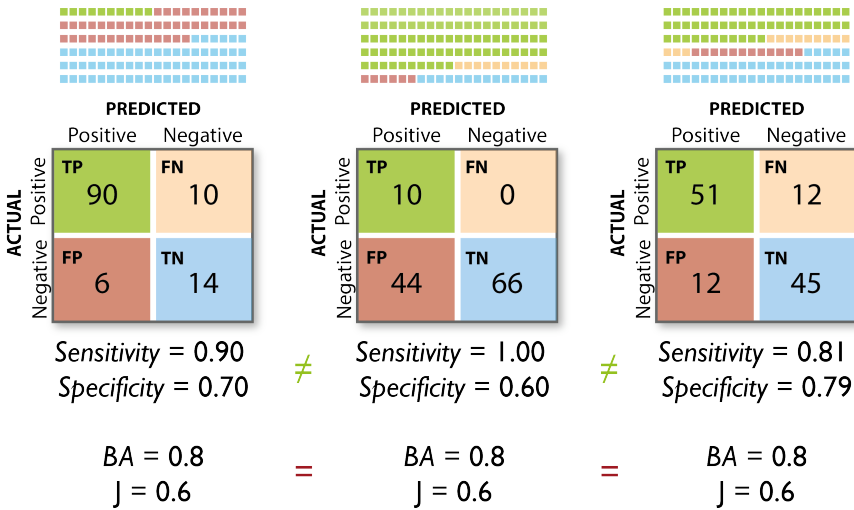


Fig. 44. Effect of the same (a) *Positive Likelihood Ratio (LR+)*, (b) *Balanced Accuracy (BA)*, and *Youden Index J* values for different combinations of cardinalities (True Positive (TP), False Negative (FN), False Positive (FP) and True Negative (TN)). A data set of 120 samples with different confusion matrices results in different *Sensitivity* and *Specificity* values. The *LR+*, *BA*, and *Youden Index J*, however, can still yield the exact same scores.

Upper bound in Cohen's κ calculation. Cohen's κ measures the agreement between ratings while incorporating information on the *Accuracy* by chance. It therefore investigates how well a prediction follows the distribution of the actual class. The maximum *Cohen's κ* helps interpreting the calculated κ score by symbolizing the corner case in which either the FP or FN are equal to 0 [83]:

$$\begin{aligned} \kappa_{max} &= \frac{p_{max} - p_e}{1 - p_e}, \\ p_{max} &= \min \left(\frac{TP + FN}{TP + TN + FP + FN}, \frac{TP + FP}{TP + TN + FP + FN} \right) \\ &\quad + \min \left(\frac{TN + FN}{TP + TN + FP + FN}, \frac{TN + FP}{TP + TN + FP + FN} \right) \end{aligned} \quad (6)$$

The maximum *Cohen's κ* score will be lower as the number of the predicted positive and negative samples diverges more from the actual number of positive and negative samples. This is shown in Figure 45 with two predictions. *Prediction 1* achieves lower *Accuracy* and *Cohen's κ* scores compared to *Prediction 2*, as it only predicts a very low number of TP. However, the predicted distribution of samples in *Prediction 1* is closer to the actual distribution of samples (13 circle predictions vs. 15 actual circles and 87 triangle predictions vs. 85 actual triangles). The distribution of samples of *Prediction 2* differs more from the actual distribution, yielding a lower *Cohen's κ_{max}* value⁹.

⁹<https://www.knime.com/blog/cohens-kappa-an-overview>

Pitfall: Upper bound not equally obtainable in Cohen's κ

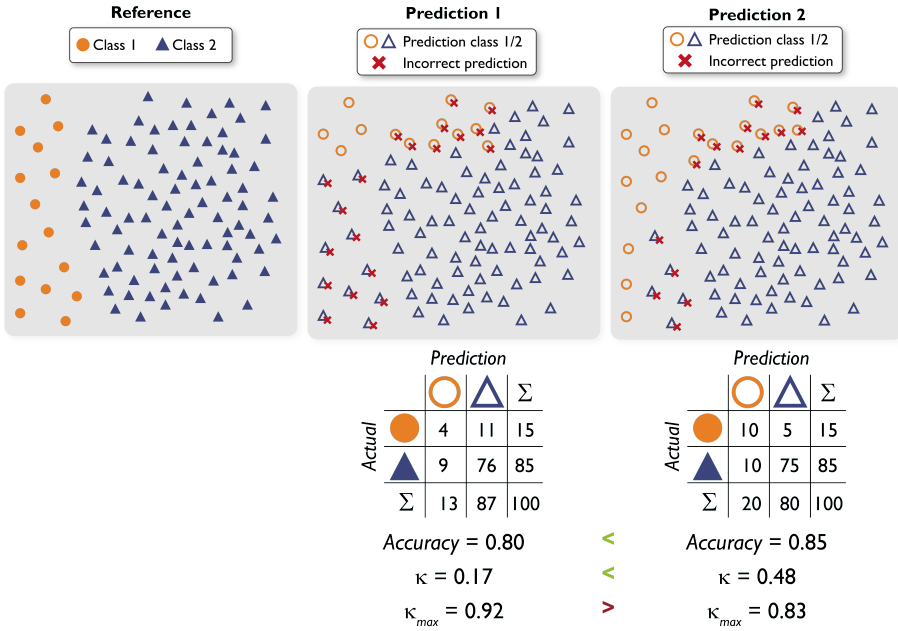
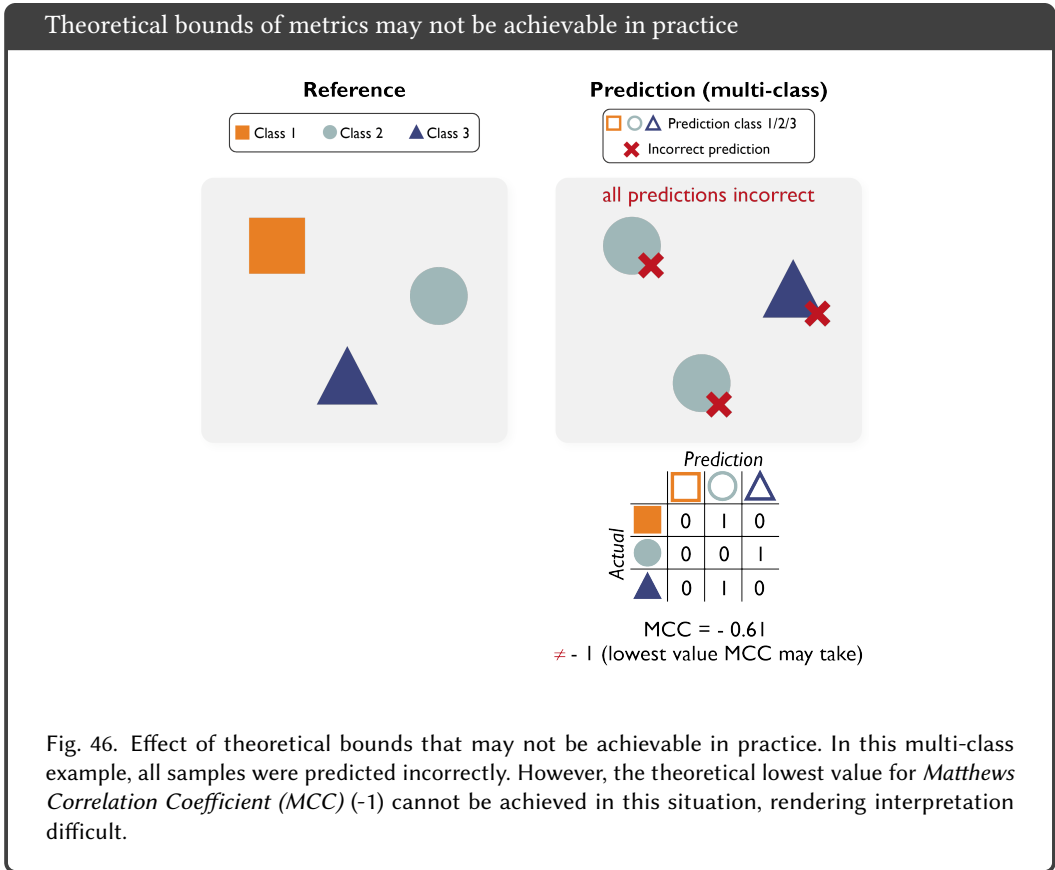


Fig. 45. Effect of different numbers of predicted positive and negative samples in comparison to the actual number of positive and negative samples. A prediction with a similar maximum of positive and negative samples to the actual distribution (*Prediction 1*) reaches higher maximum *Cohen's kappa* values compared to a prediction with a dissimilar distribution (*Prediction 2*), although the overall *Accuracy* and *Cohen's kappa* is lower. Incorrect predictions are indicated by a red cross.

Similarly, the theoretical lower bound for the MCC is not always achievable, such as in the example in Figure 46.



Determination of a global threshold for all classes. In a scenario with multiple classes, a single cutoff value for a threshold needs to be chosen for all classes. Multi-threshold metrics, such as *AUROC*, may be overly optimistic as the optimal threshold range for one class may differ from the optimal threshold range for another. Figure 47 illustrates the case of three classes that yield three perfect *AUROC* scores. However, when choosing a single threshold of 0.8 based on class 1 for all classes, the respective counting metrics will yield very poor results for classes 2 and 3.

Pitfall: Per-class tuning of the decision threshold yields misleading results

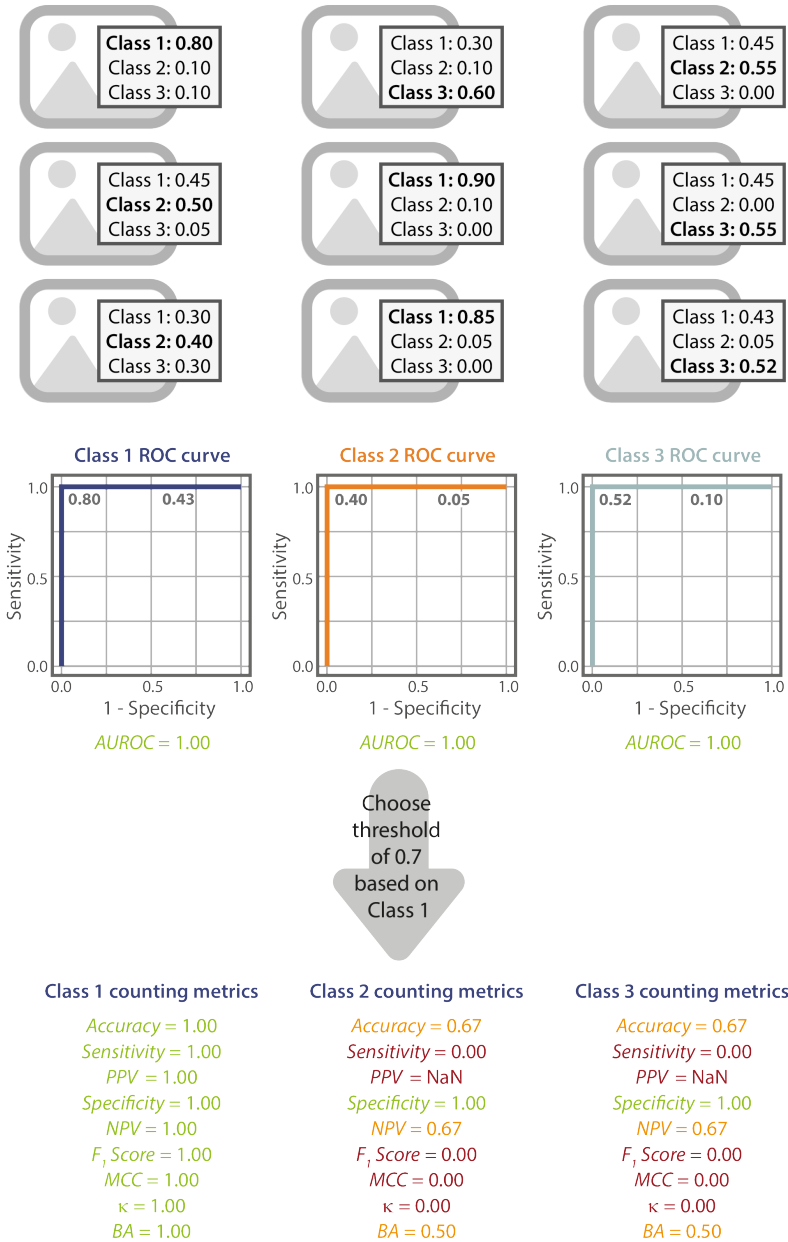


Fig. 47. Effect of the determination of a global threshold for all classes based on a single class. In a data set of three classes and nine images, the Area under the Receiver Operating Characteristic curve (AUROC) score is 1.0 for every class. In practice, however, a global decision threshold needs to be set in multi-class problems, which typically renders substantially worse results. Here, the optimal threshold for Class 1 yields poor results for Classes 2 and 3 (see e.g., [22, 51]). Used abbreviations: Positive Predictive Value (PPV), Negative Predictive Value (NPV), Matthews Correlation Coefficient (MCC), Cohen's Kappa κ , and Balanced Accuracy (BA).

Model bias. Image analysis models might be affected by image features that human experts naturally ignore and that are not truly relevant for the prediction task. Such model biases might be revealed by analyzing data external to those used for development [48]. However, multi-threshold metrics such as *AUROC* will inherently obscure model biases that affect the predicted class scores but not their ranking, if model calibration is not considered. Such a pitfall is illustrated in Figure 48 (similar to [47]). The example assumes a model that works perfectly on a subset of a larger dataset used for training. Generalizing to a different dataset when using a model with a severe bias is simulated by linear rescaling, i.e., dividing all model scores by 10, meaning that all predicted class scores will be 0.1 or below, while the ranking of the scores remains the same. Since the ranking remains the same, the *AUROC* value will not change. However, given the low predicted class scores, the model would be very confident that all cases actually belong to the negative class. Here, the substantial model bias is thus not captured by multi-threshold metrics such as *AUROC*, which would yield perfect metric values on the external dataset. In general, any metric calculation that adapts to the score distribution of the test dataset will obscure such model biases, including metrics such as *Specificity* at a particular level of *Sensitivity* (see [47] for details).

Pitfall: Area under the Receiver Operating Characteristic curve (AUROC) may obscure model bias

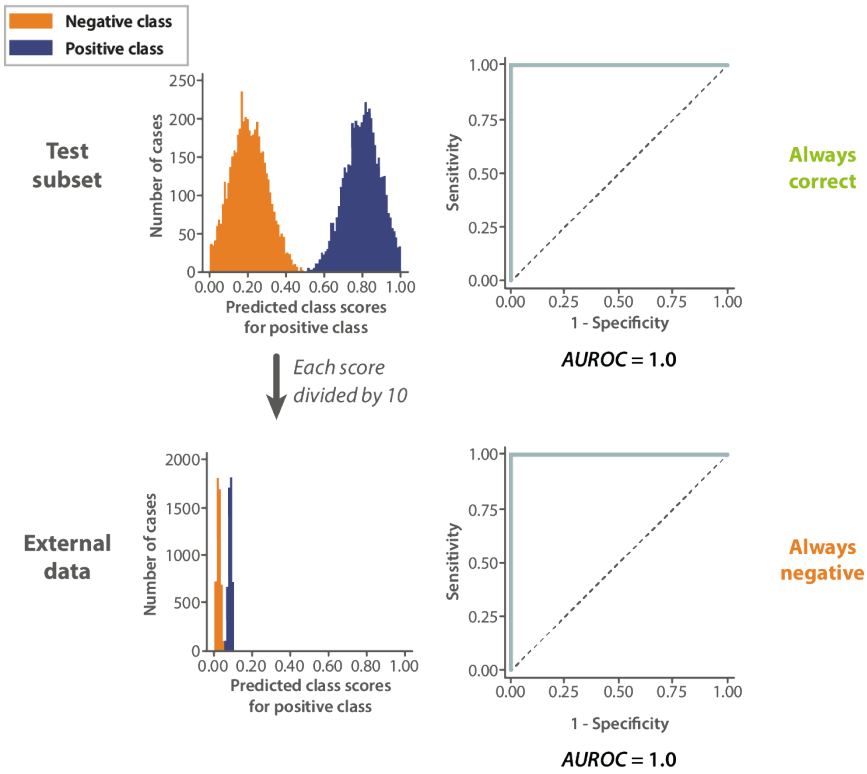


Fig. 48. Calculating the Area under the Receiver Operating Characteristic curve (AUROC) may obscure model bias. In this example, the model works well, i.e., yields very distinct predicted class scores, on a test subset ('always correct'). When generalizing to a different dataset, assuming similar conditions for the given model's predicted class scores (in this example obtained by linear rescaling), AUROC still indicates a perfect performance, although the predicted class scores for the external dataset are all very low, indicating that all predictions would be of the negative class with high confidence ('always negative'). Figure courtesy of [47].

Small sample sizes. Small sample sizes are a common issue in the biomedical image analysis domain. Caution should be applied when calculating, for example, the *AUROC* in the presence of only very few images. Figure 49 provides an example of six images (three positive, three negative samples) for two data sets and the respective predicted class scores of an algorithm. The data sets only differ in a single image. However, this apparently minor difference will result in a difference in the *AUROC* scores of 0.11. By calculating the 95% Confidence Interval (CI), we see that the CIs are very large and do not allow for proper interpretation of *AUROC* scores in the case of very small sample sizes.

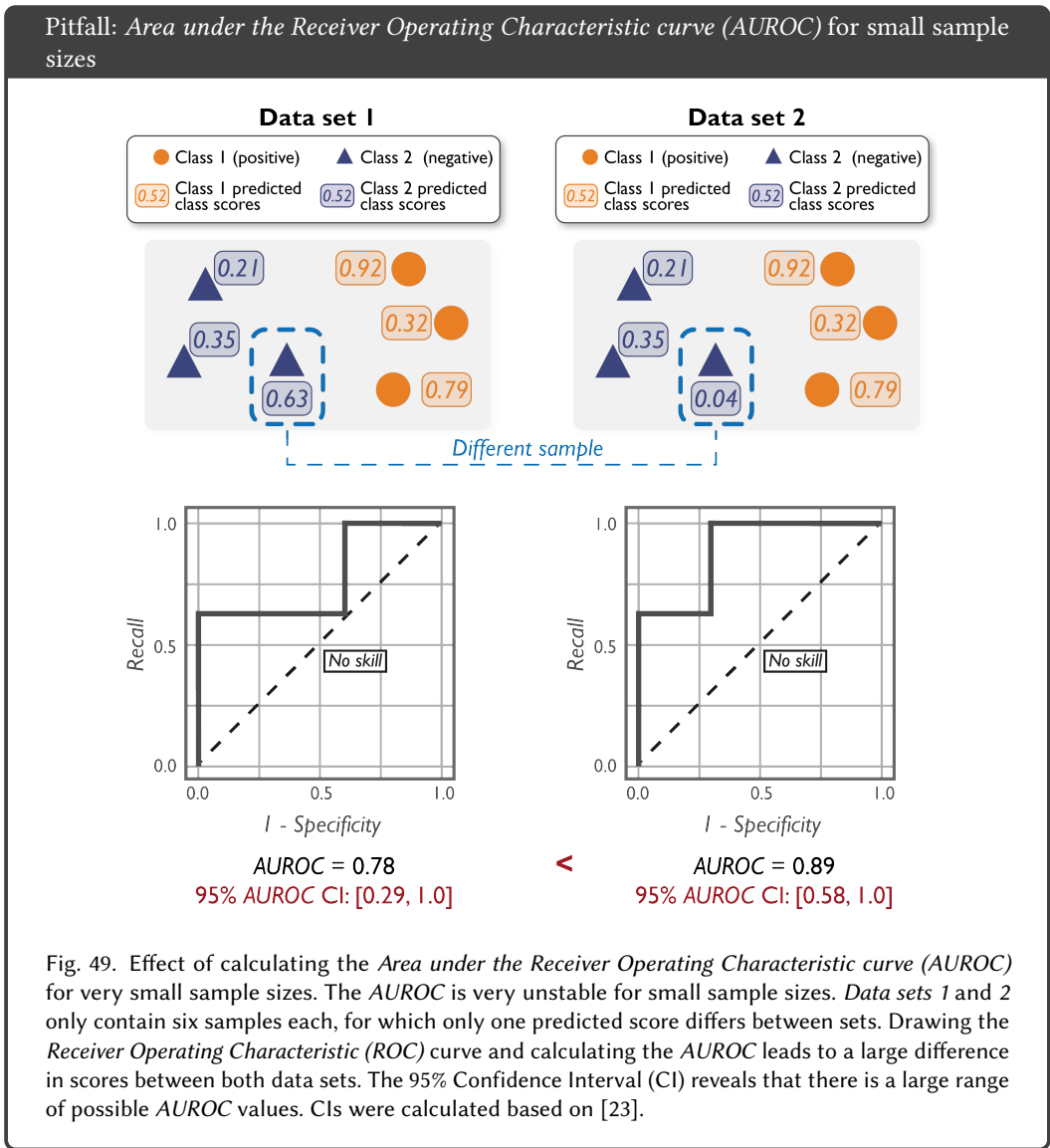


Fig. 49. Effect of calculating the Area under the Receiver Operating Characteristic curve (*AUROC*) for very small sample sizes. The *AUROC* is very unstable for small sample sizes. *Data sets 1* and *2* only contain six samples each, for which only one predicted score differs between sets. Drawing the *Receiver Operating Characteristic (ROC)* curve and calculating the *AUROC* leads to a large difference in scores between both data sets. The 95% Confidence Interval (CI) reveals that there is a large range of possible *AUROC* values. CIs were calculated based on [23].

5 PITFALLS RELATED TO SEGMENTATION

All pitfalls compiled for this work and relevant for semantic or instance segmentation are summarized in Table 1. This section focuses on limitations for semantic segmentation, but some of them are also transferable to other problem categories, as indicated in the table. Limitations of metrics are typically related to the following properties:

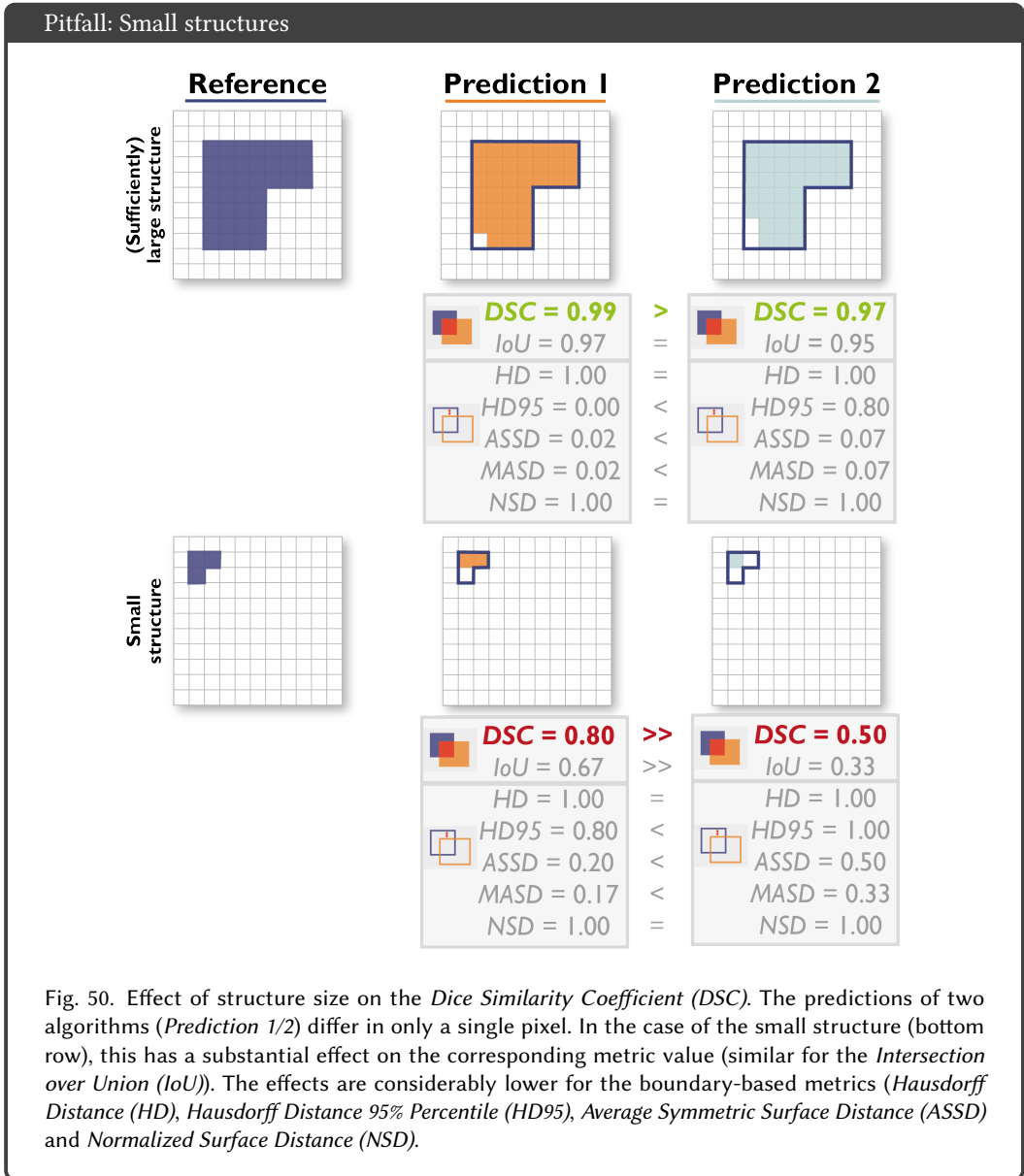
- Small size of structures relative to pixel size (Figures 50 - 51)
- High variability of structure sizes (Figures 52 - 53)
- Complex shapes of structures (Figures 54 - 56)
- Particular importance of structure volume (Figure 57)
- Particular importance of structure center (Figure 58)
- Particular importance of structure boundaries (Figure 59 - 60)
- Possibility of multiple labels per unit (Figure 61)
- High inter-rater variability (Figure 62)
- Possibility of outliers in reference annotation (Figure 63)
- Possibility of reference or prediction without the target structure (Figure 64)

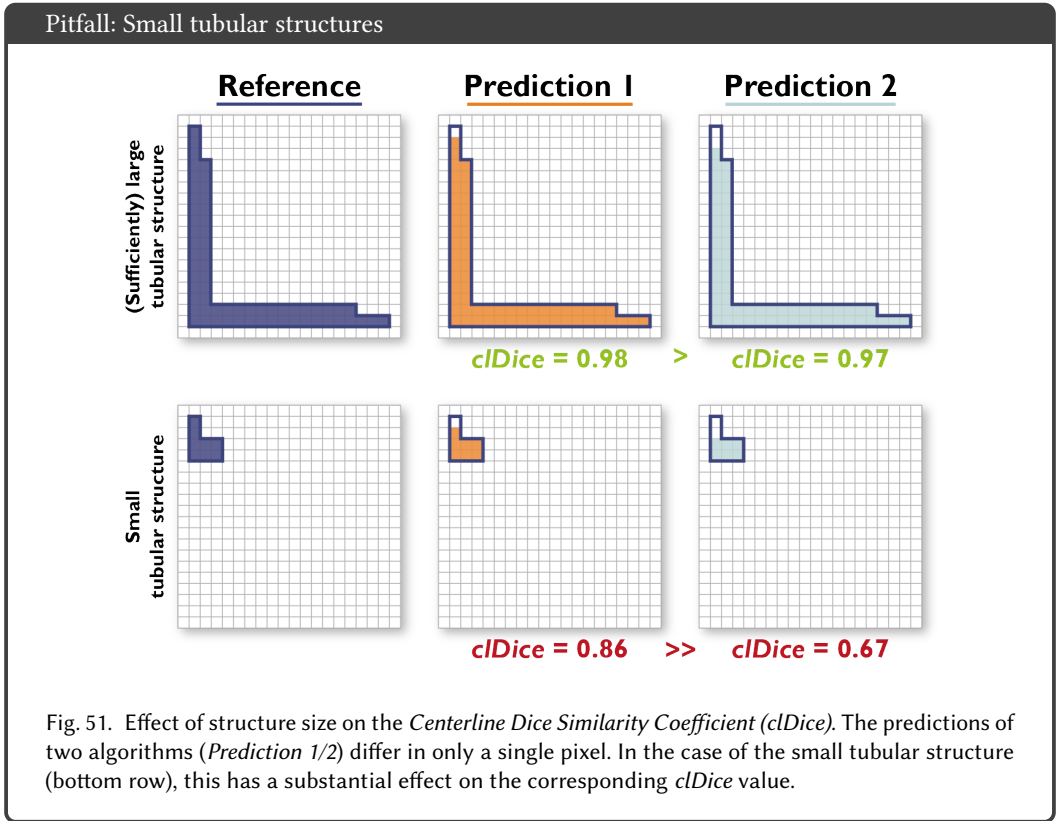
Further pitfalls are related to technical peculiarities, such as the image resolution (Figure 65), preference for over- vs. undersegmentation (Figure 66) and the choice of global decision threshold for creating the confusion matrix (Figure 67).

The limitations are presented for the most commonly used overlap segmentation metrics, namely *DSC*, *IoU*, and the most common boundary-based metrics, namely *HD*, *HD95*, *ASSD*, *MASD* and *NSD*. The *NSD* calculation is based on a user-defined threshold (cf. Figure 10). Results differ for different thresholds. Unless stated otherwise, we set the threshold to $\tau = 1$.

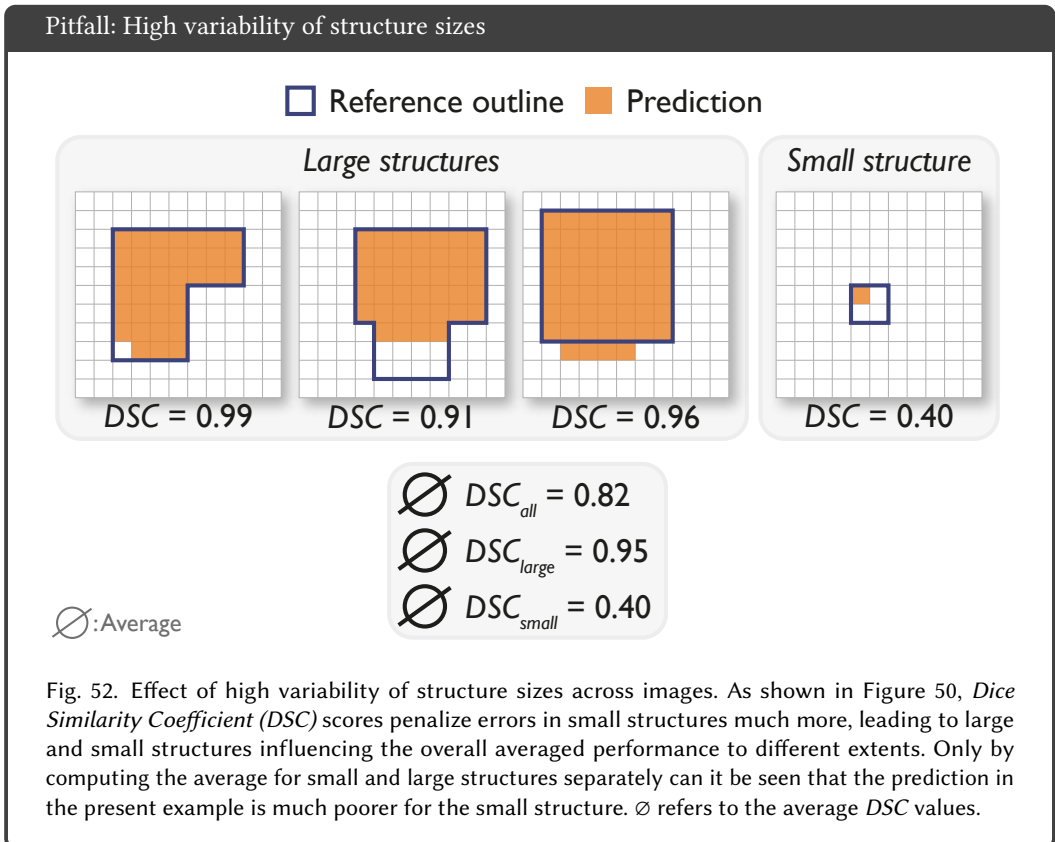
To preserve clarity of the illustrations, specific values may only be highlighted for one metric from each metric family, if the other metrics share similar properties (e.g. *DSC* and *IoU* share the same properties). Green metric values correspond to a "good" value (e.g. a high *DSC* or a low *HD* score), whereas red values correspond to a "bad" value (e.g. a low *DSC* or a high *HD* score). Green check marks indicate metric scores reflecting the research question, red crosses show those that do not. Please note that a low *DSC* value (or similar) is not automatically a "bad" score. A metric value should always be put into perspective and compared to inter-rater variability. We only use the terms "good" and "bad/poor" for simplicity.

Small size of structures relative to pixel size. Segmentation of small structures, such as brain lesions or cells imaged at low magnification, is essential for many image processing applications. In these cases, the *DSC* or *IoU* may not be appropriate metrics, as illustrated in Figure 50 (cf. [14]). In fact, a single-pixel difference between two predictions can have a large impact on the metric values. Given that the correct outlines (e.g. of pathologies) are often unknown and taking into account the potentially high inter-observer variability related to generating reference annotations [44], it is typically not desirable for few pixels to influence the metrics as much. This problem is particularly amplified in cases of large variability of structure sizes (cf. Figure 52). The same problem arises for other versions of the *DSC* or *IoU*. For example, the *clDice* is often used in the case of tubular structures. Similarly to the original *DSC* metric, a single-pixel difference will have a larger influence on the *clDice* for small tube structures compared to larger ones. This pitfall also applies to object detection tasks. It should be noted that once a data set exclusively contains only very tiny structures, one may consider this problem to be an object detection rather than a segmentation problem.





High variability of structure sizes. The size of target structures may vary substantially, both within an image and across images. For example, in medical instrument segmentation in laparoscopic video data, an image frame may contain full-sized instruments as well as only the tip of an instrument just entering the scene [73]. In these cases, metrics need to be chosen carefully. As shown in the example above (Figure 50), metrics such as the *DSC* or *IoU* are typically not well-suited for very small structures. Furthermore, size stratification – the aggregation of metric values for objects of similar sizes to uncover differences between them – should be employed. Figure 52 shows an exemplary data set of four images, containing three large structures and one small structure. When aggregating over all *DSC* values, the average *DSC* is 0.82. Computing the average for large and small structures separately, however, shows that the performance is much lower for the small structures compared to the large ones, demonstrating the large influence of the low metric values of small objects. This pitfall also applies to object detection tasks and other metrics.



The ASSD and MASD often result in very similar metric scores, as both compute the average over distances from the boundaries. While ASSD calculates the general average over all distances, the MASD computes the average distance for each of the structures and calculates the mean over those averages. MASD, however, substantially rewards situations in which the predicted structure is significantly smaller than the reference object and is located near the surface of the reference, as shown in the example of Figure 53. In this case, the average distance from the prediction to the reference is approximately zero. Thus, only the average distance from the reference to the prediction decides the score. For MASD, this distance is halved, which leads to a significantly better score compared to that obtained with ASSD.

Pitfall: High variability of sizes for the Mean Average Surface Distance (MASD) and Average Symmetric Surface Distance (ASSD)

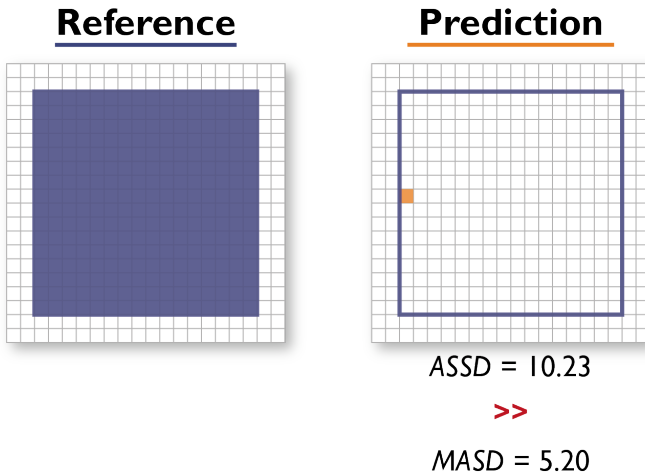


Fig. 53. Corner case in which Mean Average Surface Distance (MASD) yields an undesired result. If the *Prediction* is very small (here: one pixel) and located close to the reference boundary, the Mean Average Surface Distance (MASD) will be much lower compared to the Average Symmetric Surface Distance (ASSD).

Complex shapes of structures. Metrics measuring the overlap between objects are not designed to uncover differences in shapes. This is an important problem in many applications such as radiotherapy, for which identifying and treating all parts of the tumor is essential to avoid recurrence [10]. Figure 54 illustrates that completely different object shapes may lead to the exact same *DSC* and *IoU* values. Boundary-based measures are able to detect the changes in shapes [81]. Note that this pitfall also applies to object detection tasks.

Pitfall: Shape unawareness

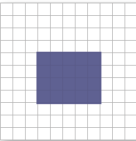
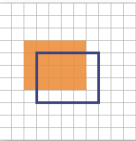
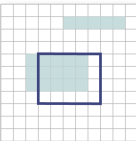
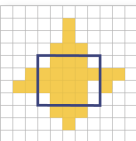
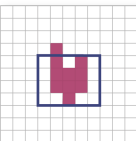
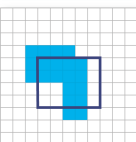
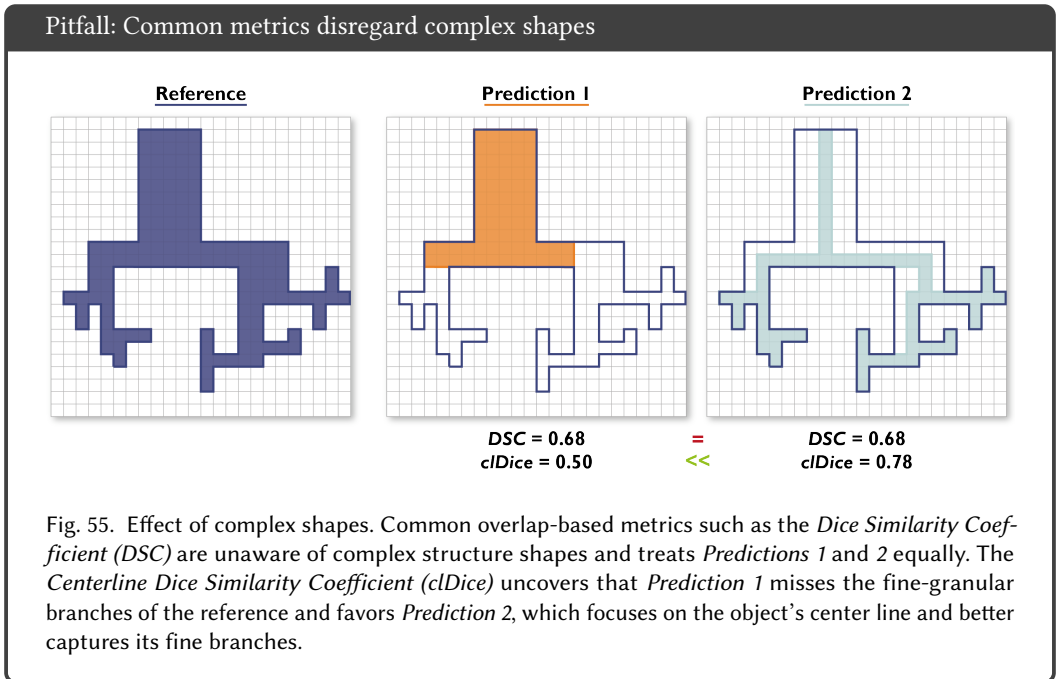
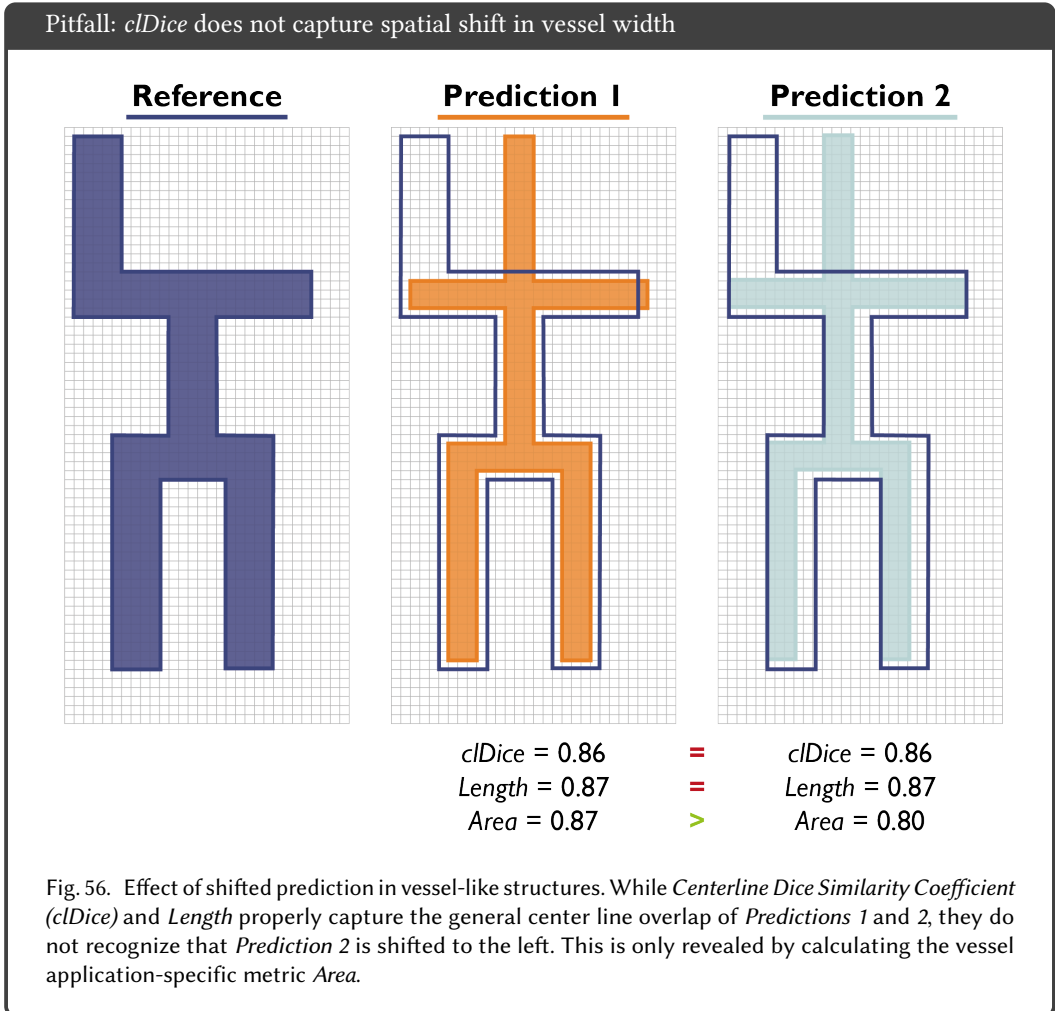
Reference	DSC	IoU	HD	HD95	ASSD	MASD	NSD
							
Prediction 1 	DSC = 0.6	IoU = 0.4	HD = 1.4	HD95 = 1.3	ASSD = 0.9	MASD = 0.9	NSD = 1.0
Prediction 2 	DSC = 0.6	IoU = 0.4	HD = 3.6	HD95 = 3.1	ASSD = 1.0	MASD = 1.0	NSD = 0.7
Prediction 3 	DSC = 0.6	IoU = 0.4	HD = 3.0	HD95 = 2.0	ASSD = 0.8	MASD = 0.7	NSD = 0.8
Prediction 4 	DSC = 0.6	IoU = 0.4	HD = 2.2	HD95 = 2.0	ASSD = 0.8	MASD = 0.7	NSD = 0.8
Prediction 5 	DSC = 0.6	IoU = 0.4	HD = 2.0	HD95 = 1.2	ASSD = 0.8	MASD = 0.8	NSD = 0.9

Fig. 54. Effect of different shapes. The shapes of the predictions of five algorithms (*Predictions 1-5*) differ substantially, but lead to the exact same *Dice Similarity Coefficient (DSC)* and *Intersection over Union (IoU)*, while boundary-based metrics (*Hausdorff Distance (HD)*, *Hausdorff Distance 95% Percentile (HD95)*, *Average Symmetric Surface Distance (ASSD)* and *Normalized Surface Distance (NSD)*) consider the shape differences.

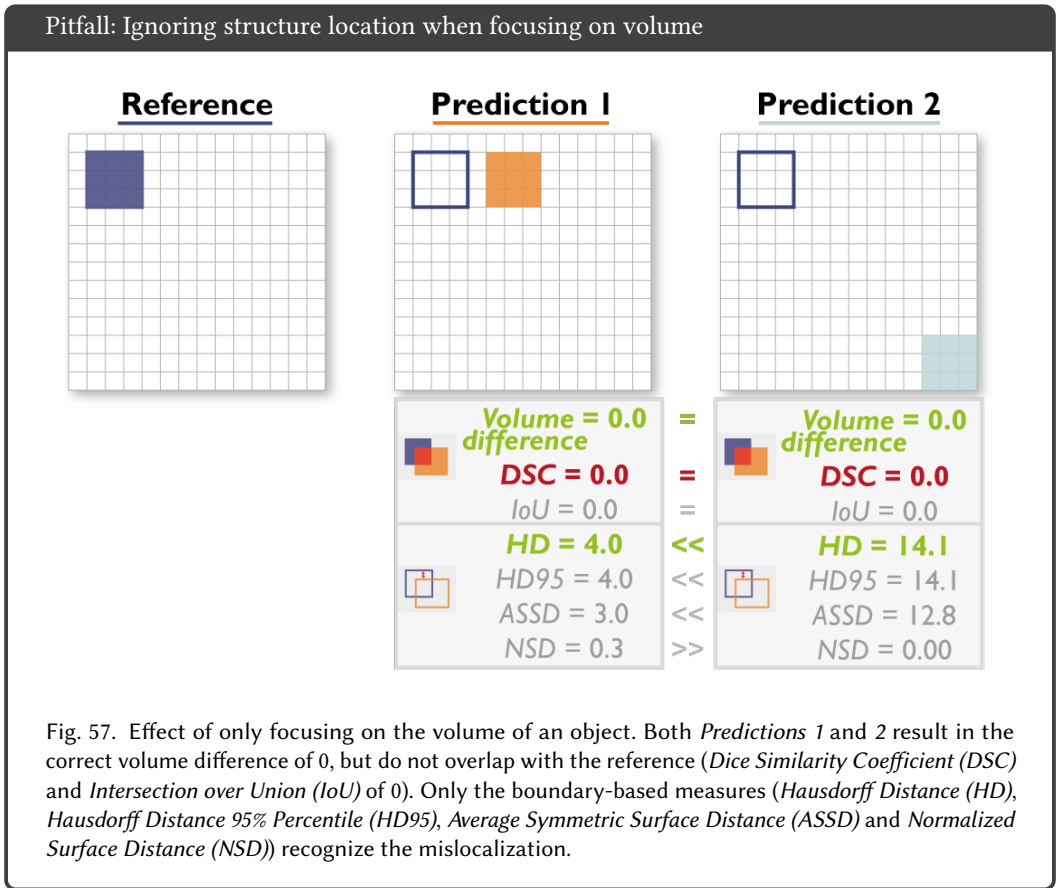
Shape unawareness is especially harmful in the case of very complex shapes, for example in bronchi. These structures typically feature many small branches, as depicted in a simplified manner in Figure 55. In this example, *Prediction 1* only shows the root of the structure, while *Prediction 2* focuses on its center line, which would be the preferred option. However, common overlap-based metrics such as the *DSC* yield the same value for both predictions. The *cIDice* on the other hand, designed to capture the center line focus, recognizes the difference and penalizes *Prediction 1* with a substantially lower value.



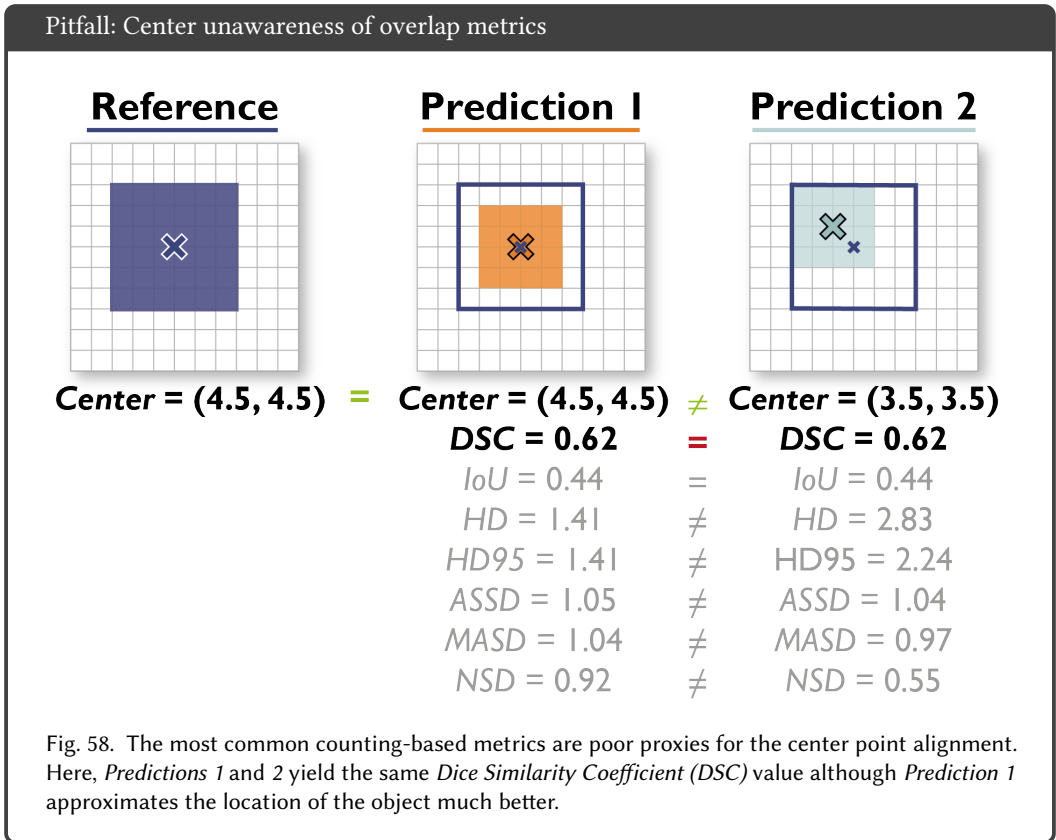
While the *clDice* can typically validate tree-like structures such as vessels better than other overlap-based measures, it still faces limitations. Clinicians are sometimes particularly interested in predicting the length of a vessel, whereas its width may be of lesser importance. As shown in Figure 56, *clDice* captures the length of the vessel-like structure in a similar manner as another proposed metric called *Length* [28]. However, it does not recognize that *Prediction 2* is spatially shifted to the left. This shift could be captured by domain-specific metrics such as the *Area* [28], introducing a tolerance factor to vessel width.



Particular importance of structure volume. Depending on the domain focus, a surgeon, radiologist or similar may be especially interested in the volume of a segmented structure. The most commonly used metrics may, however, result in predictions at entirely wrong locations if boundary or overlap are not considered. Figure 57 shows two predictions of a 3x3 square structure, both of them being at the wrong position. While the volume difference is correct for both predictions, the overlap is zero. Only boundary-based metrics will indicate the magnitude of mislocalization of the predicted objects.



Particular importance of structure center. The structure center point or center line may be more important than an accurate boundary or overlap of the structure, as for example in nerve segmentation [61]. In these cases, the accuracy of the center point or line should be examined via an additional metric to make sure the center is correct for the prediction. Figure 58 shows two predictions yielding the same *DSC* values, as they have the same overlap to the reference annotation. However, only *Prediction 1* is centered around the same point as the reference, while *Prediction 2* is shifted slightly towards the upper left corner and thus centered incorrectly. This pitfall also applies to object detection tasks. It should be noted that once the center location is of particular importance to the task, one may consider it an object detection rather than a segmentation problem.



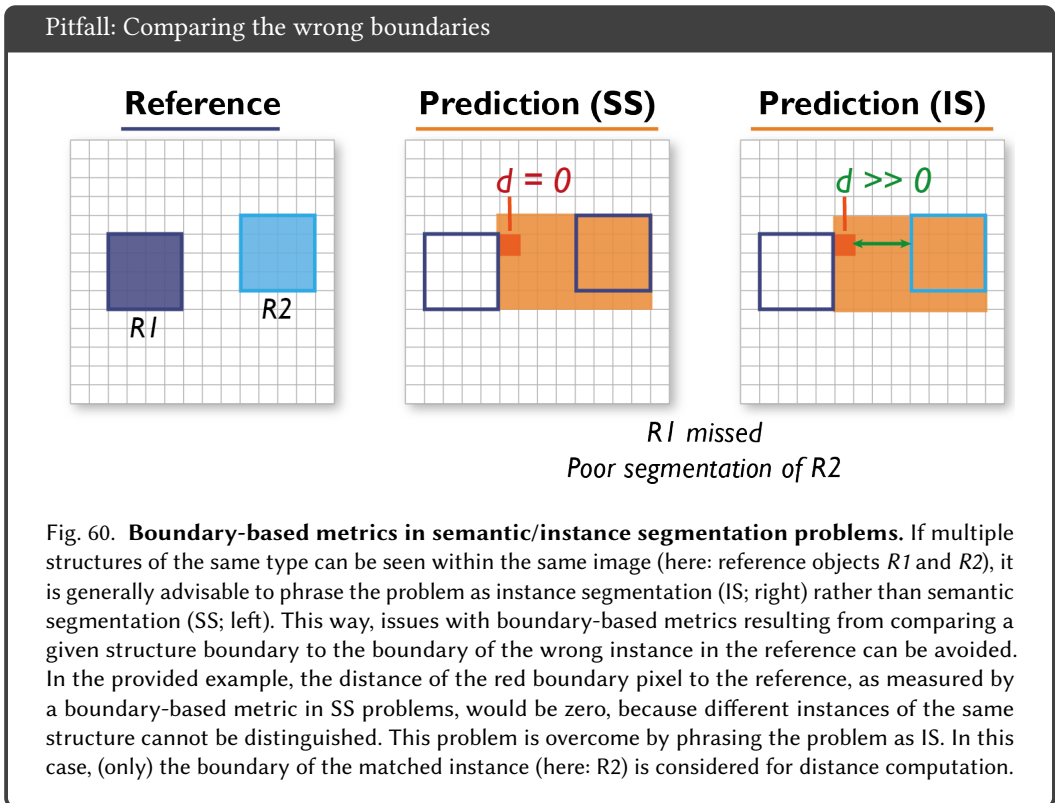
Particular importance of structure boundaries. While boundary-based metrics such as the $HD(95)$, $ASSD$ and others can help to detect shape differences between the reference and the predicted object, they do not focus on the object itself. As shown in Figure 59(top), the boundary-based metrics do not recognize a prediction with a large hole inside as poor (*Prediction 2*). Furthermore, in Figure 59(bottom) [81], those metrics do not punish the spotted pattern within the object. It should be noted that this behavior may also be desirable. For example, it may be highly difficult to decide whether a necrotic core (hole) is present in a tumor or not. A boundary-based metric would not punish errors resulting from such annotation uncertainties.

Pitfall: Holes in the segmentation ignored by boundary-based metrics

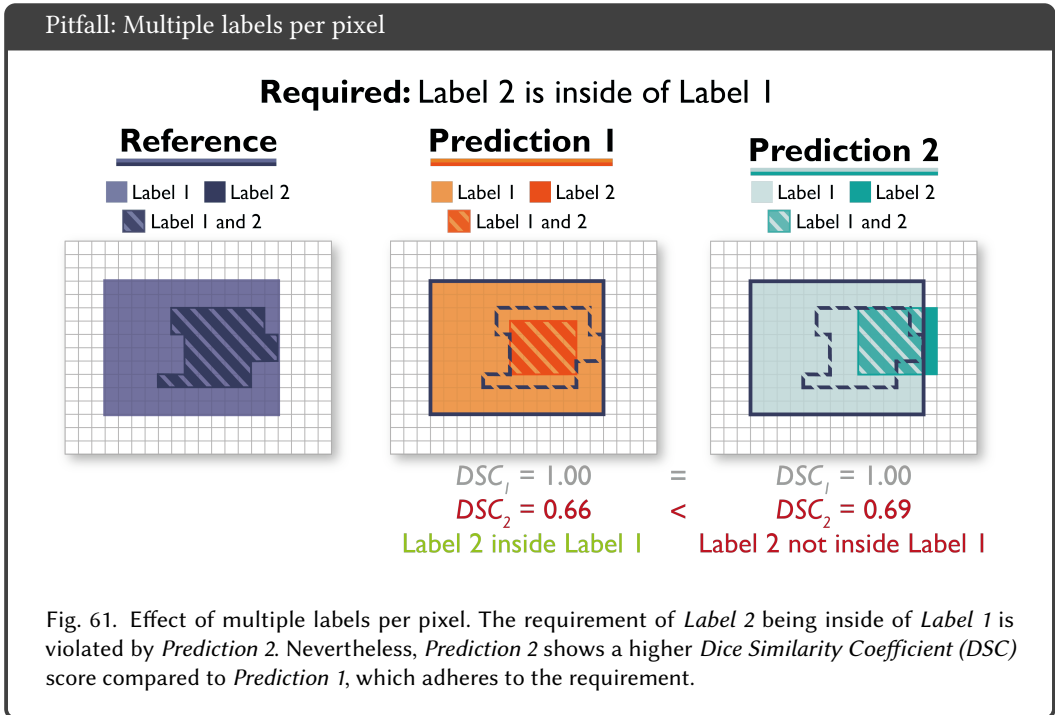


Fig. 59. Boundary-based metrics commonly ignore the overlap between structures and are thus insensitive to holes in structures. **Upper part:** Here, *Predictions 1* and *2* feature holes within the object. The boundary-based metrics (*Hausdorff Distance (HD)*, *Hausdorff Distance 95% Percentile (HD95)*, *Average Symmetric Surface Distance (ASSD)*, *Normalized Surface Distance (NSD)*) do not recognize this problem, yielding very good or even perfect metric scores of 0.00 for the *HD(95)/ASSD* and 1.00 for the *NSD (Prediction 2)*, whereas the overlap-based metrics (*Dice Similarity Coefficient (DSC)*, *Intersection over Union (IoU)*) reflect the fact that the inner area is missed by the predictions. **Lower part:** Here, *Predictions 1* and *2* feature a spotted pattern within the object. Although the boundary of *Prediction 2* is perfect, the holes are penalized by the boundary-based metrics compared to *Prediction 1*. *Prediction 1* shows an imperfect boundary. Depending on the surface-based metric used, slight deviations in the boundary (here in *Prediction 1*) may be tolerated, reflected by calculating the *NSD* for $\tau = 1$.

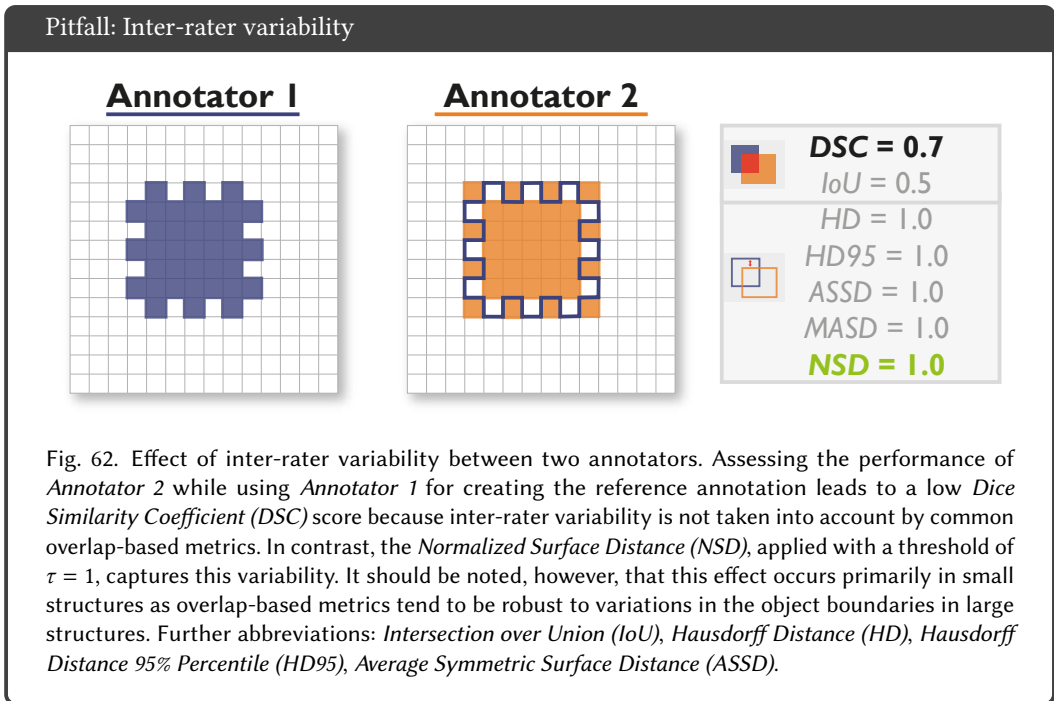
Please note that boundary-based metrics are not appropriate under several circumstances. In scenarios in which multiple structures of the same type are present within the same image (e.g., in multiple sclerosis lesion segmentation), for example, a potential pitfall is related to comparing a predicted structure boundary to the boundary of the wrong instance in the reference, as shown in Figure 60. In this example, the prediction misses the reference object *R1*, while poorly segmenting *R2*. In the case of a semantic segmentation, the distance between the red pixel and the object boundary would be zero, which may not be desired. If phrased as an instance segmentation problem, the distance would be higher, and thus penalized.



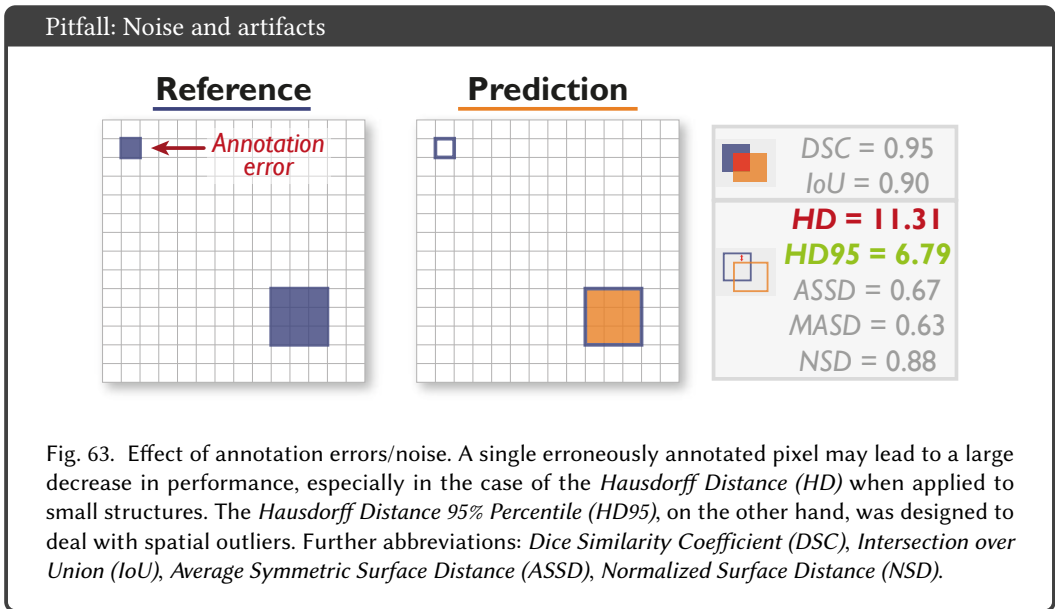
Possibility of multiple labels per unit. In several biomedical imaging scenarios, multiple labels per pixel may be possible. A prominent example would be the tumor core inside the tumor [60]. Often, however, prior knowledge related to such scenarios (e.g. a tumor core cannot lie outside the tumor) is not reflected by common metrics, which simply calculate the agreement of the reference and prediction per class. Figure 61 shows two predictions for a multi-label example. The DSC value of *Label 2*, which is required to be inside of *Label 1*, is higher for *Prediction 2* although *Label 2* is also found outside the *Label 1* area. For simplicity, we only show the results for the DSC metric. This pitfall also applies to object detection tasks.



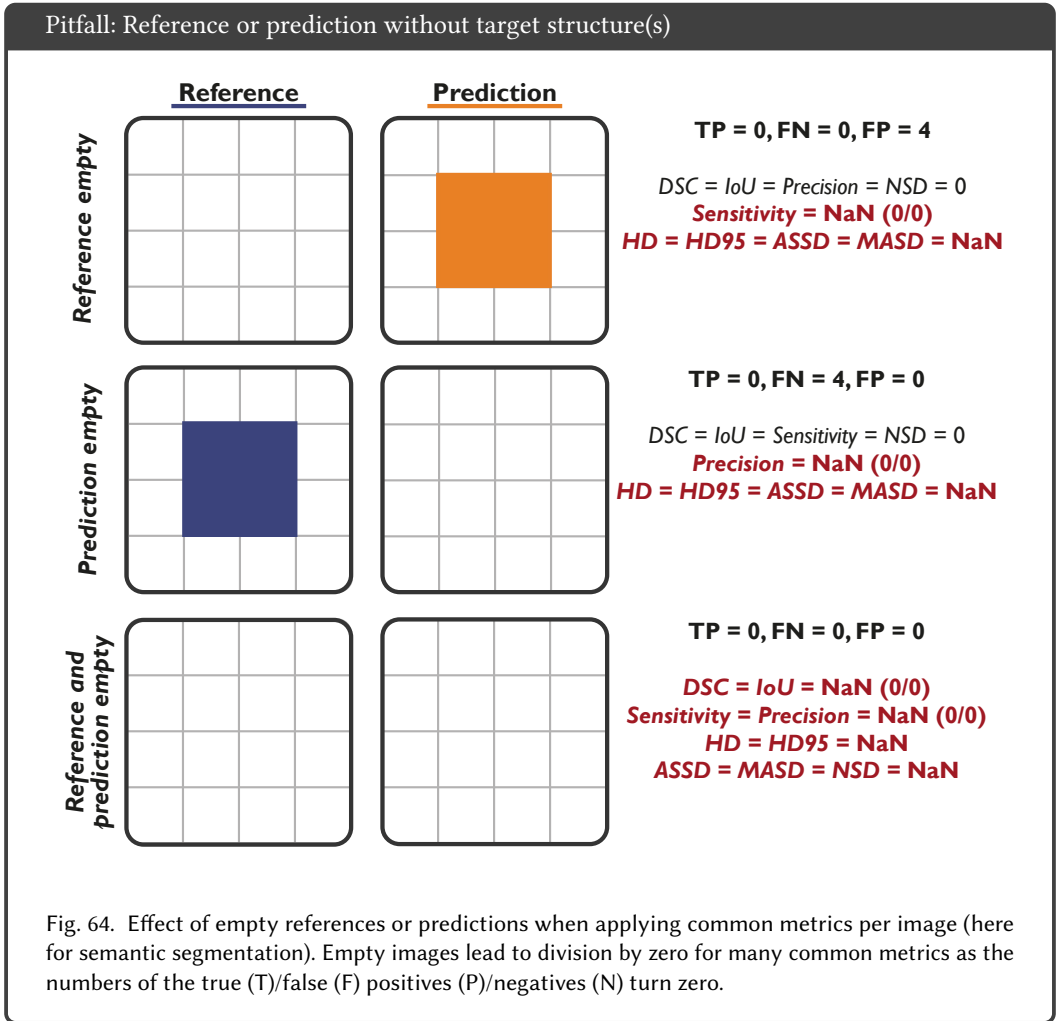
Imperfect reference standard. A high quality reference annotation is crucial to determine the performance of a supervised learning algorithm. A prediction can be almost perfect, but low quality reference images will still result in a bad metric score. Especially in the medical domain, the inter-rater variability is often very high as domain knowledge is required and experts themselves often disagree [44]. Figure 62 shows two masks from different annotators approximating the same structure. Although the annotations differ only slightly at the boundary, the *DSC* score is 0.7. With such inter-rater variability, a *DSC* score of 1 would not be achievable in practice. To address this issue, the *NSD* metric can be applied as an alternative or additional metric, as it is designed to allow a certain tolerance of outline pixels based on the threshold τ . This pitfall can also be translated to object detection and image-level classification tasks.



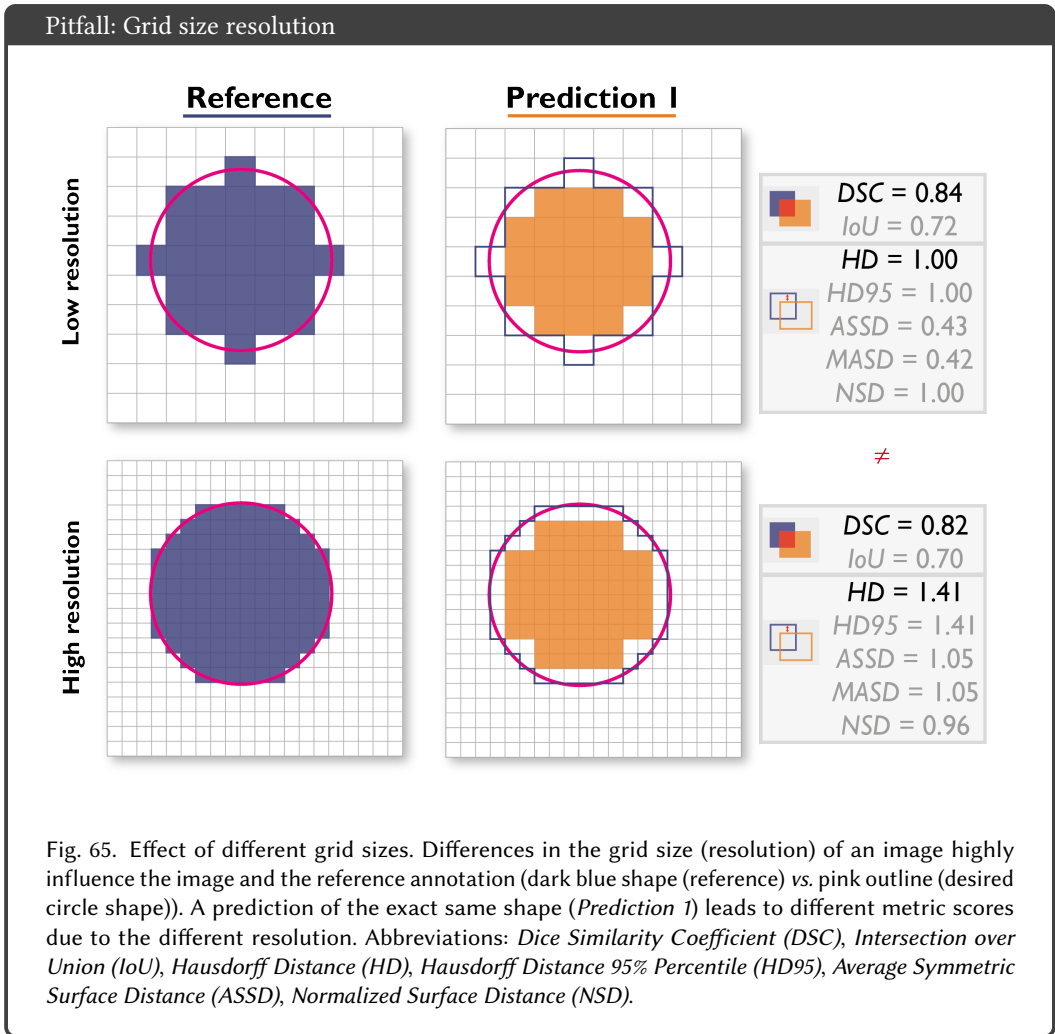
Possibility of outliers in reference annotation. The presence of spatial outliers, such as noise or reference annotation artifacts, may severely impact performance metric values. Figure 63 demonstrates how a single erroneous pixel in the reference annotation (or the prediction) leads to a substantial decrease in the measured performance, especially in the case of the *HD*. Using the 95% percentile instead of the maximum (*HD95*) to compute the distance substantially improves the metric score as it can handle outliers. Please note that the presented example may also be seen vice versa, with a prediction including single pixel errors. It should further be noted that whether or not outliers should be considered depends on the respective research question.



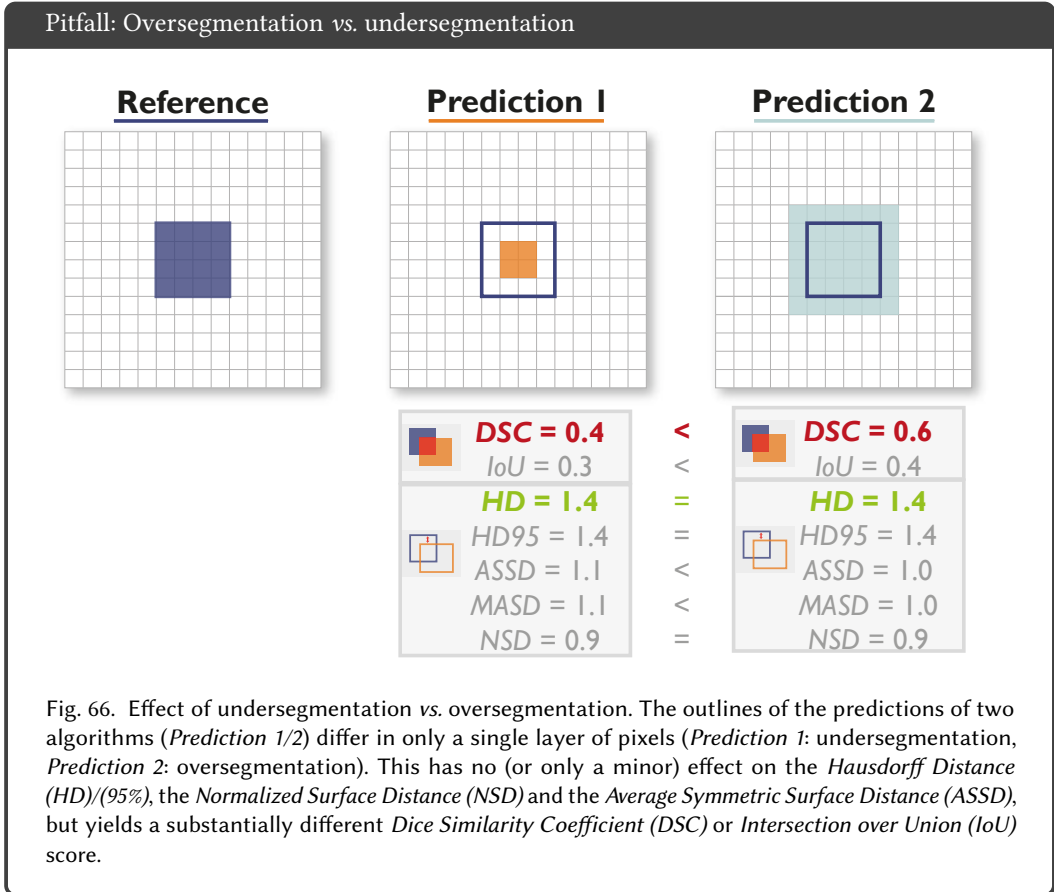
Possibility of reference/prediction without target structure(s). A given data set may contain reference annotations without the target structure(s). For example, the data set may consist of healthy and sick patients. A healthy patient will not have a tumor in the image, yielding an empty reference if the tumor is the targeted structure. An algorithm should be careful not to classify a healthy patient as tumourous as this may lead to unnecessary medical interventions. Similarly, a patient with a tumor should not be classified as healthy (empty prediction). These cases require special care to be taken in the validation, because some metrics may be undefined due to division by zero errors or similar. It is necessary to either choose appropriate metrics that consider empty references (or predictions) or account for it in the metric implementation. For example, boundary-based metrics such as the $HD(95)$ and $ASSD$ will be NaN if one of the structures is empty. Figure 64 shows three examples, for which several counting- and boundary-based metrics were computed. The top row depicts the case of an empty reference and a prediction of an object. Given the number of TP and FN being 0, this will result in a division by zero in the *Sensitivity* calculation, yielding a NaN score. A similar case is given in the second row, showing an empty prediction for a given target structure in the reference annotation, yielding an undefined *Precision*. When both reference and prediction are empty (bottom row), all scores will be undefined. Please note that this example is shown for a validation per image, as done for segmentation tasks. For classification and object detection tasks, the validation is typically performed over the whole data set, which would possibly preclude this problem. The presented pitfall also applies to object detection tasks.



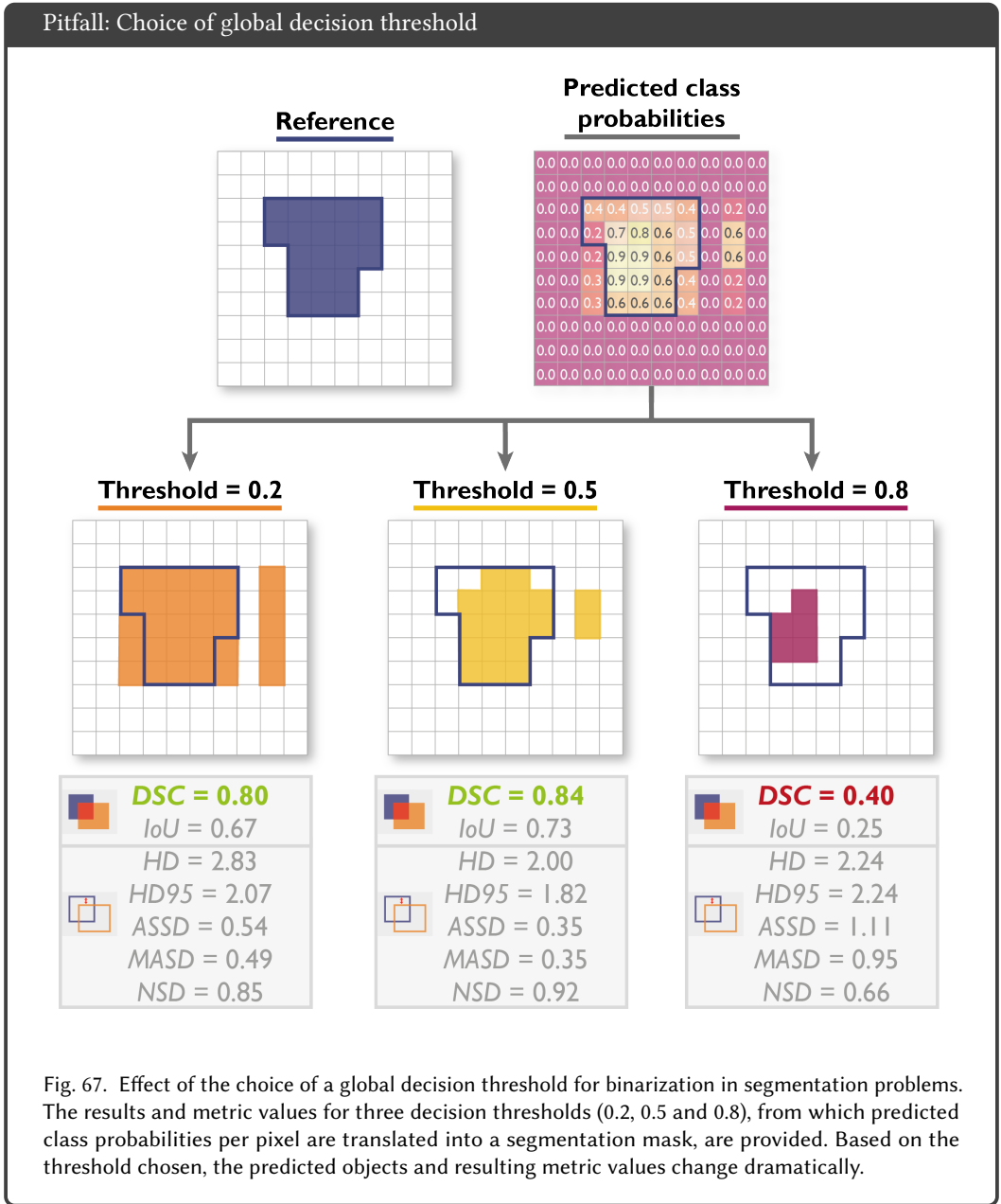
Technical peculiarities. Several technical peculiarities also have an impact on metric behavior. For example, the image resolution and pixel sizes highly influence the reference annotation and the predicted shapes in image processing tasks. Figure 65 illustrates how the reference annotation differs between a low resolution image (top) and a high resolution image (bottom) compared to a circle. The latter is more exact. A prediction of the same size will therefore lead to different corresponding metric values, independent of the type of the metric. This pitfall also applies to object detection tasks.



In some applications such as radiotherapy, it may be highly relevant whether an algorithm tends to over- or undersegment the target structure. The *DSC* metric, however, does not represent over- and undersegmentation equally [92]. As depicted in Figure 66, a difference of a single layer of pixels in the outline yields different *DSC* scores (oversegmentation preferred) [81]. Other boundary-based performance values such as the *HD* are invariant to these properties.



Another technical peculiarity is the choice of global decision threshold. Most methods in modern image analysis output continuous class scores. While it is quite common to provide those scores in image-level classification and object detection tasks, segmentation architectures often do not output class probabilities per pixel. However, fuzzy segmentation masks are getting more and more common (for instance, see [1, 45, 66]) and the choice of a global decision threshold τ is very important for the algorithm's result. Figure 67 (cf. [65]) shows the predicted class probabilities for a reference annotation. For a binarization typically required for segmentation outputs, a threshold needs to be defined based on which a pixel is assigned to a class (here: a pixel with class probability $< \tau$ corresponds to the background class, otherwise to the foreground class). The resulting segmentation masks are shown for the thresholds 0.2, 0.5 and 0.8. It can be seen that the respective masks completely differ across the thresholds. Consequently, metric values will also vastly change.



6 PITFALLS RELATED TO OBJECT DETECTION

All pitfalls compiled for this work and relevant for object detection are summarized in Table 1. Note that these pitfalls equally apply to instance segmentation problems. While most issues related to the actual metric selection have already been mentioned in the previous paragraphs, this section is primarily dedicated to technical peculiarities related to the localization and assignment criteria. These include:

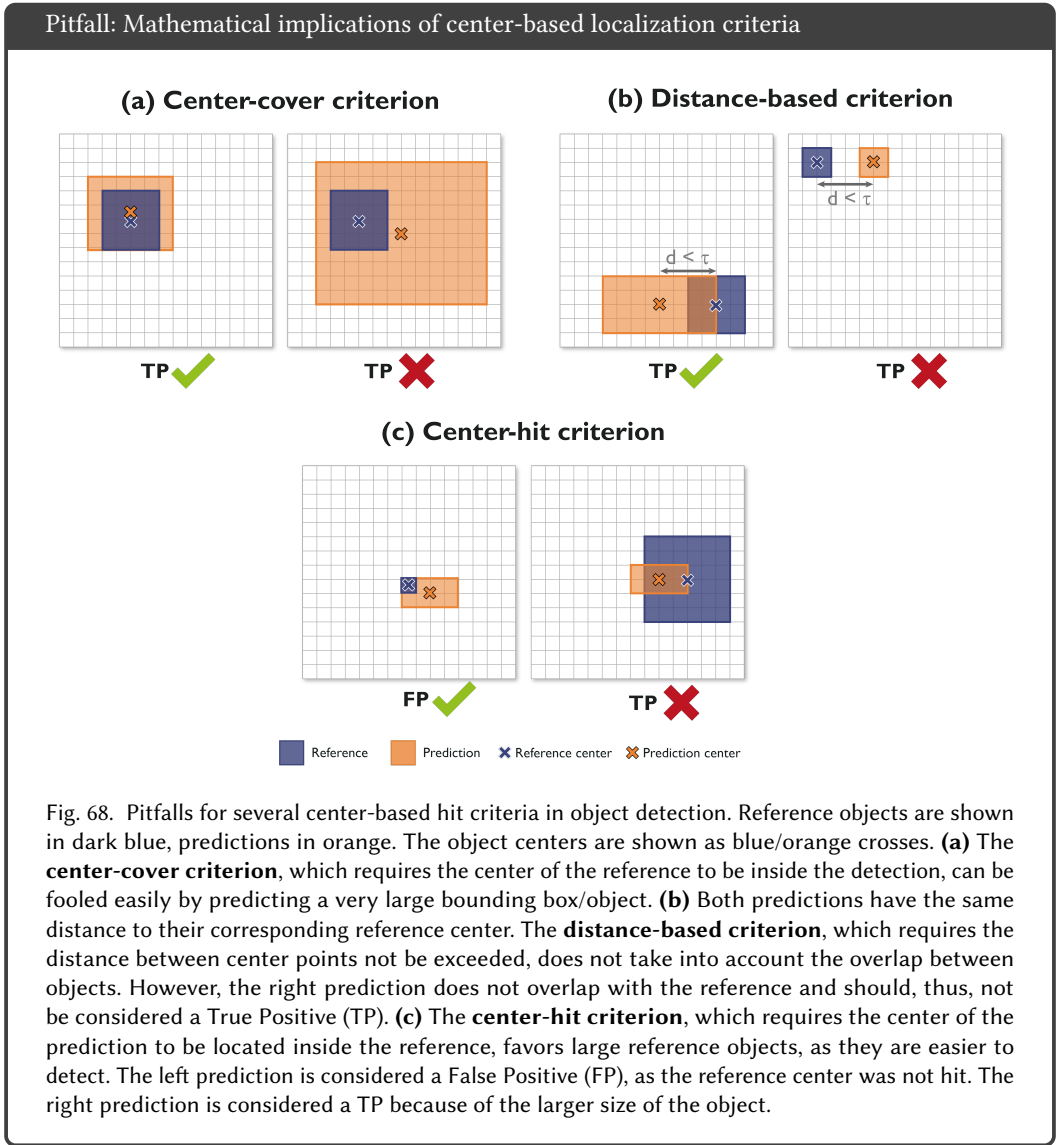
- Mathematical implications of center-based localization criteria (Figures 68 - 69)
- Mathematical implications of *IoU*-based localization criteria (Figure 70)
- Mathematical implications of the choice of assignment strategies (Figure 71 - 73)
- Effect of small structures on localization criterion (Figure 74)
- Perfect *Boundary IoU* for imperfect prediction (Figure 75)
- Possibility of reference or prediction without the target structure and NaN handling (Figure 76)
- *Average Precision vs. Free-response ROC* score (Figure 77)
- *Free-response ROC score* is not standardized (Figure 78)
- Effect of predicted class probabilities on multi-threshold metrics (Figures 79 - 81)
- Non-standardized metric definition (Figure 82)

Mathematical implications of center-based localization criteria. Before calculating metrics for object detection tasks, it is necessary to define what qualifies a detection as a *hit* (TP) or *miss* (FP). There are multiple ways to define a hit, all of which come with their specific limitations. Below, the most commonly used center-based localization criteria are presented¹⁰¹¹.

- For the **center-cover criterion**, the reference object is considered a hit if the center of the reference object is inside the predicted detection. Figure 68a shows how this criterion can be fooled by a model outputting very large boxes to maximize the chance of a correct detection. The same issue holds true for the Point inside Mask/Box criterion, which is fulfilled if a single predicted point lies inside the reference object.
- In the case of the **distance-based hit criterion**, a prediction is considered a hit if the distance d between the center of the reference and the detected object is smaller than a certain threshold τ . In Figure 68b, both predictions have the same distance to their corresponding reference object centers. However, the prediction on the top right shows no overlap with the reference and should therefore not be counted as a hit.
- The **center-hit criterion** holds true if the center of the predicted object is inside the reference bounding box or contour. Given this definition, large reference objects are more likely to be hit, as shown in Figure 68c. The left prediction is defined as a missed object (FP), the right detection as a hit because of its larger size.

¹⁰For more details, please refer to the blogpost "Evaluation curves for object detection algorithms in medical images": <https://medium.com/lunit/evaluation-curves-for-object-detection-algorithms-in-medical-images-4b083fddce6e>.

¹¹The presented pitfalls are also valid for approximations or bounding circles instead of the shown bounding boxes.



The center point might not be a good reference for complex shapes such as tubular structures (Figure 69). In those cases (and if annotations are provided in the form of masks), a binary “Point inside Mask” criterion might be the better choice.

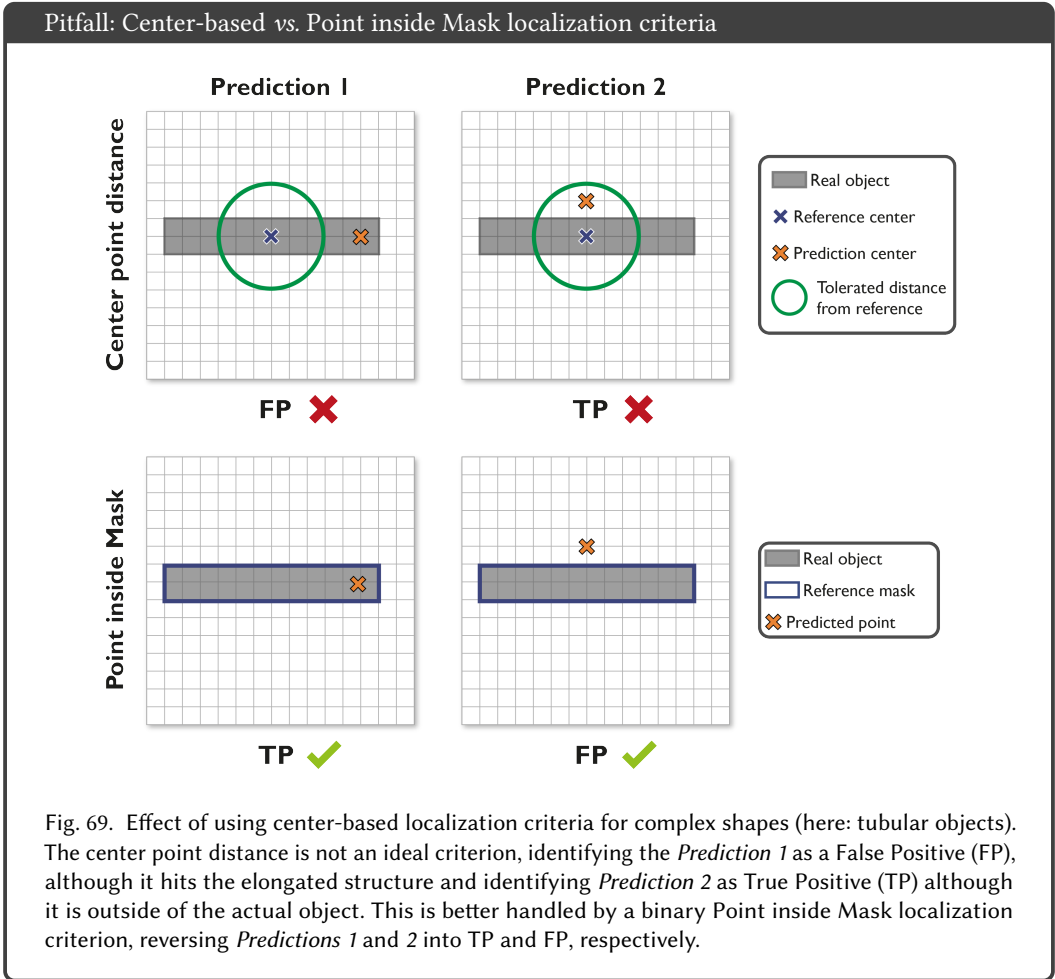


Fig. 69. Effect of using center-based localization criteria for complex shapes (here: tubular objects). The center point distance is not an ideal criterion, identifying the *Prediction 1* as a False Positive (FP), although it hits the elongated structure and identifying *Prediction 2* as True Positive (TP) although it is outside of the actual object. This is better handled by a binary Point inside Mask localization criterion, reversing *Predictions 1* and *2* into TP and FP, respectively.

Mathematical implications of IoU-based localization criteria. The most commonly used hit criterion is determined by computing the *IoU* between the predicted and the reference mask/bounding box/boundary. Pitfalls related to *IoU*-based criteria are mainly related to the setting of the threshold (Figure 70). Many biomedical applications involve 3D rather than 2D images. When working with a higher dimension, it should be kept in mind that metrics may be affected. The additional dimension will lead to overlap errors being punished even more. Figure 70a shows a comparison of the *IoU* for two rectangles (or bounding boxes) in 2D and 3D. Being mistaken by one voxel in the *z*-dimension will lead to a much lower *IoU* score in 3D compared to the 2D case.

As *IoU*-based criteria take the overlap between regions into account, it is only possible to cheat with very large boxes if the *IoU* threshold is set to a very small value (here: 0), as shown in Figure 70b. However, special care should be taken when applying the *Box IoU* in the presence of highly concave or elongated structures, as illustrated in Figure 70c. This is because bounding boxes may quickly grow for narrow and diagonally placed objects, such as medical instruments, and result in FP although visual inspection would indicate a correct prediction.

Pitfall: Mathematical implications of *IoU*-based localization criteria

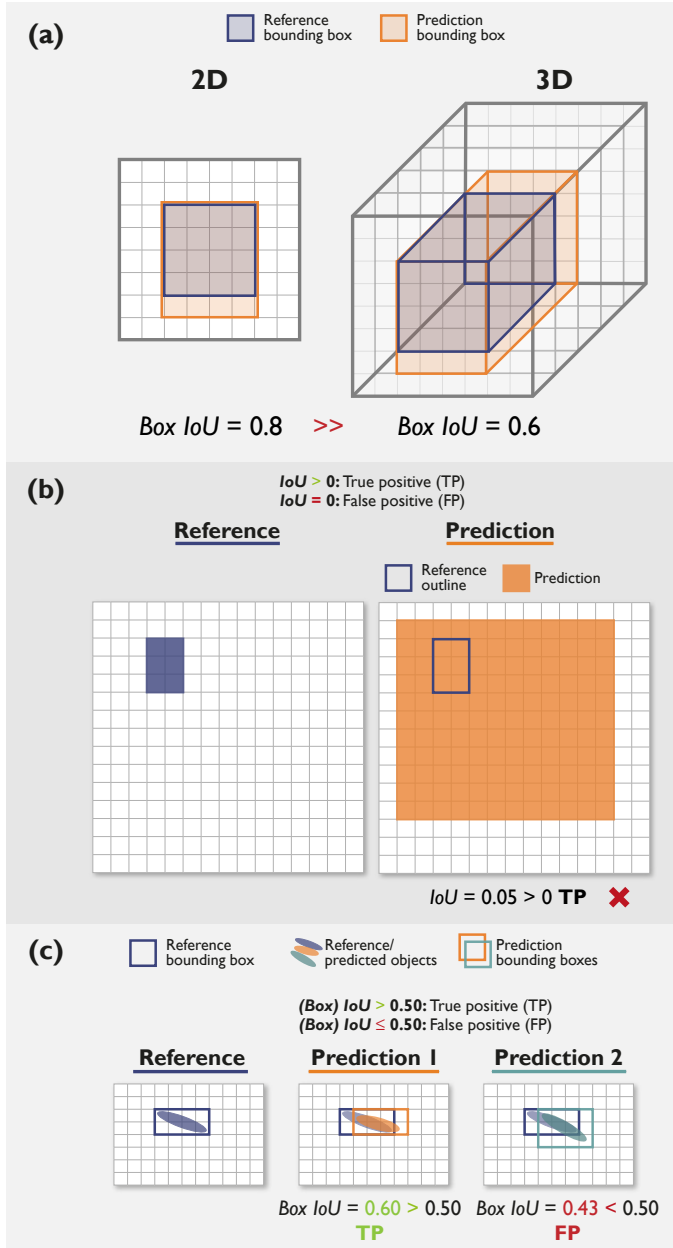
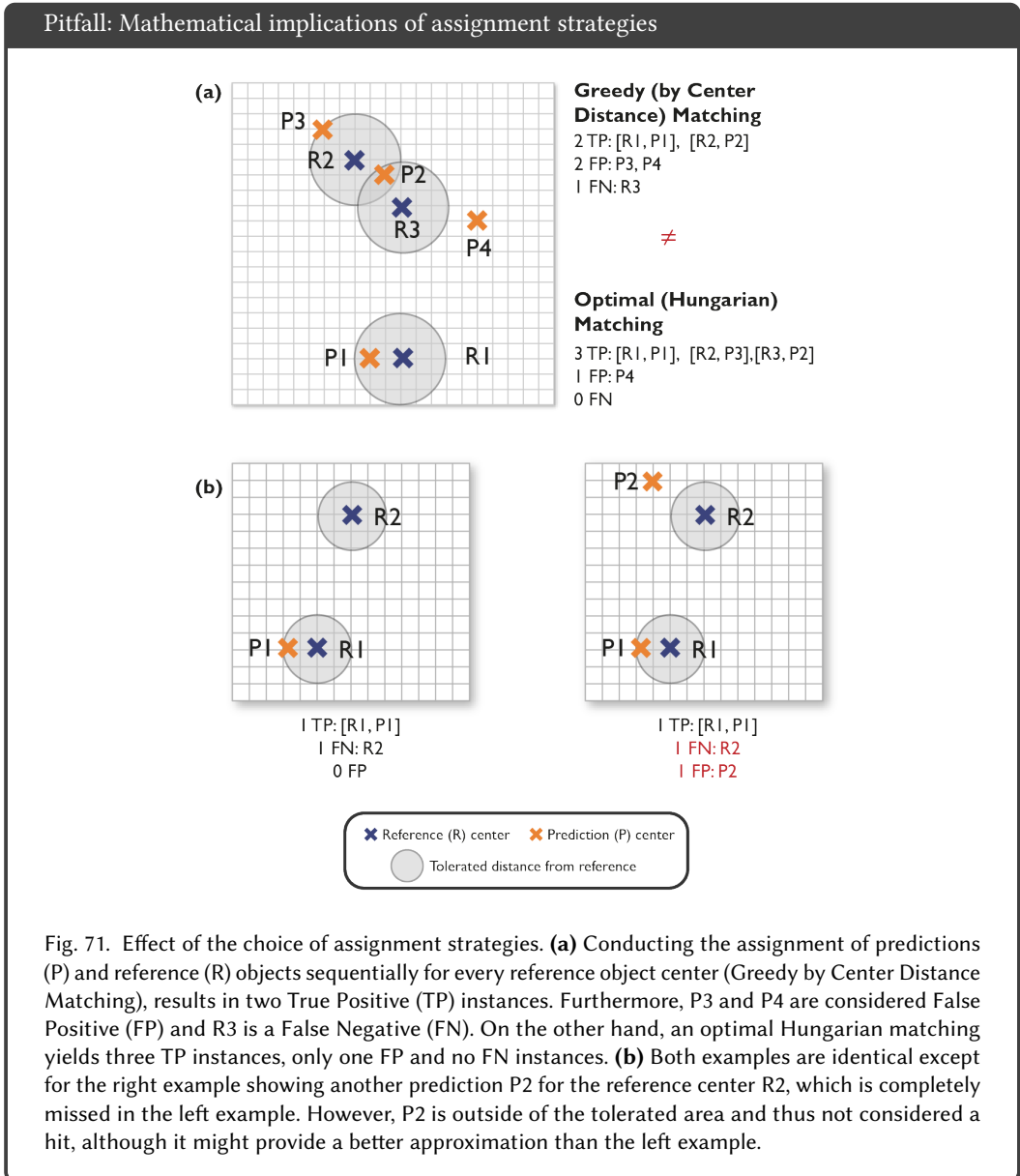


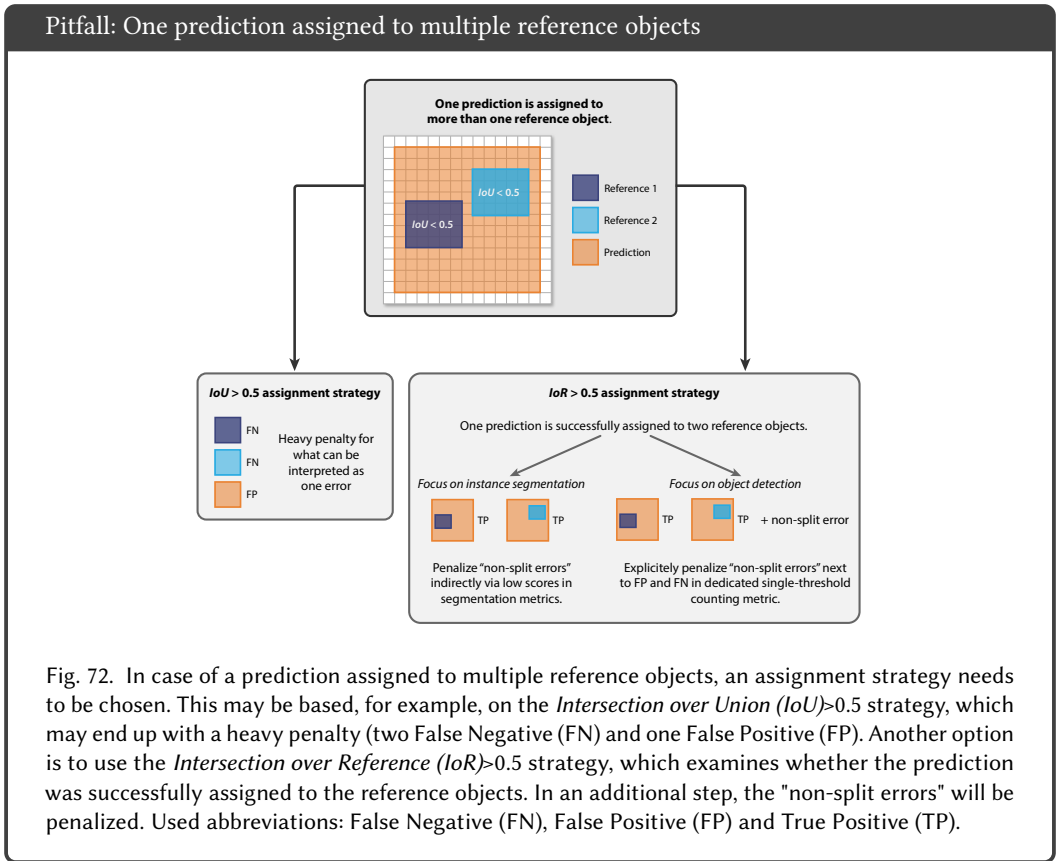
Fig. 70. The *Intersection over Union (IoU)* is a commonly used localization criterion in object detection. It comes with several limitations: **(a)** The image dimension should be considered when setting the *IoU* (here: *Box IoU*) threshold for object detection. In 3D settings, the additional z-dimension results in a cubical increase in erroneous pixels. **(b)** Effect of a loose *IoU* criterion for object detection. When defining a True Positive (TP) by an *IoU* > 0, the resulting localizations may be fooled by very large predictions. **(c)** Effect of defining TP based on the *IoU* (here: *Box IoU*) threshold of the reference and predicted bounding boxes. Especially for diagonal, narrow objects, the number of bounding box pixels may change quadratically. Although *Predictions 1* and *2* are very similar, their bounding boxes diverge and lead to one of them being defined as TP, the other as False Positive (FP).

Mathematical implications of the choice of assignment strategies. Different assignment strategies may yield different proportions of TPs, FPs and FNs. This is shown in Figure 71a, in which two different assignment strategies based on the center distance are shown for the same situation with three reference and four predicted objects. Matching one reference object at a time (Greedy by Center Distance Matching) yields two TP matches: [R1, P1] and [R2, P2]. This is due to the fact that the distance between R2 and P2 is smaller than the distance between R2 and P3 and that between R3 and P2. Thus, R2 is assigned to P2. The distance between R3 and P3 or P4 is greater than the defined tolerance, thus, P3 and P4 are seen as FP and R3 is a FN. If an Optimal (Hungarian) Matching [52] is applied, matching is performed differently by optimizing a cost function. This yields a different assignment with three TP objects. Here, P3 is assigned to R2 and P2 is assigned to R3. As all reference objects are assigned, no FN appears. Only P4 is counted as a FP.

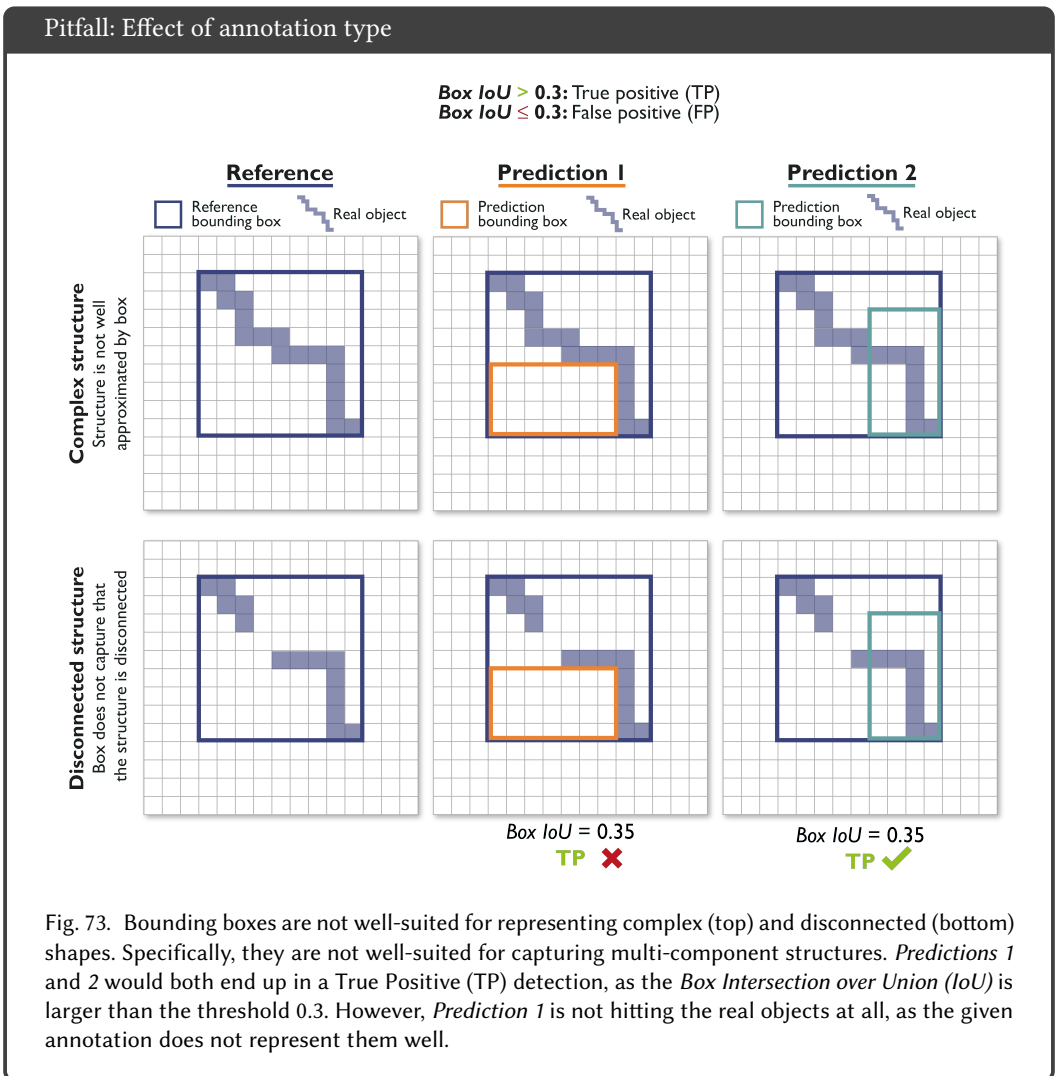
In addition, researchers should think about whether FNs should be further distinguished into real FNs, i.e., reference objects for which no prediction exists (see left example in Figure 71b) and predictions that are outside a distance threshold or below an overlap threshold (see right example in Figure 71b). The latter case may be more useful in the present example, as R2 is not fully overlooked although P2 lies outside of the threshold area.



Penalization of one prediction assigned to multiple reference objects requested. Object detection and instance segmentation algorithms typically involve the step of assigning predicted objects to reference objects. This may result in one prediction being assigned to multiple reference objects or vice versa. Using the $IoU > 0.5$ (or similar threshold) as assignment strategy may end up in a very strict penalty of two FN and one FP if the IoU for both reference objects is smaller than the threshold (as shown for two reference objects in Figure 72. Using the IoR may result in a less strict penalization for what could be interpreted as only a single error with an additional step of penalizing the non-split errors (either directly in object detection or indirectly in instance segmentation) [59].

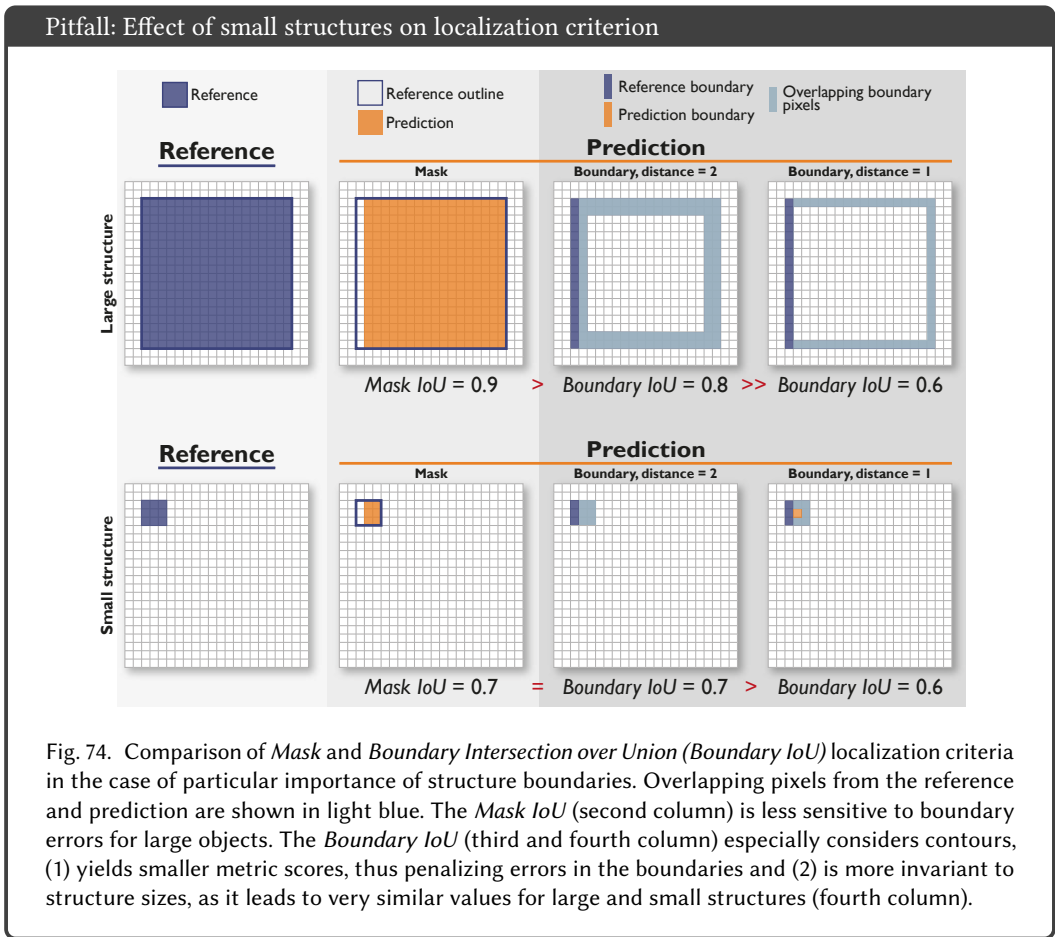


Possibility of disconnected structures. The *Box IoU* is sometimes employed despite access to pixel-mask annotations. A possible explanation is that researchers want to phrase their problem as an object detection problem and then apply the most commonly used validation methods. Such simplification might cause problems if structures are not well approximated by a box shape, or if structures yield multi-component masks, appearing to be disconnected. This may occur in the case of a tubular structure shown in a 2D tomographic image or a medical instrument occluded by tissue in an endoscopic image, for example. Figure 73 provides examples of a complex diagonal (top) and a disconnected structure (bottom). Both box predictions yield a *Box IoU* larger than 0.3, and are thus counted as TP because of the chosen localization threshold. Nevertheless, *Prediction 1* is not hitting the actual object at all. This is due to the fact that the target structures are not well approximated by the bounding box, leaving many empty pixels in the boxes.



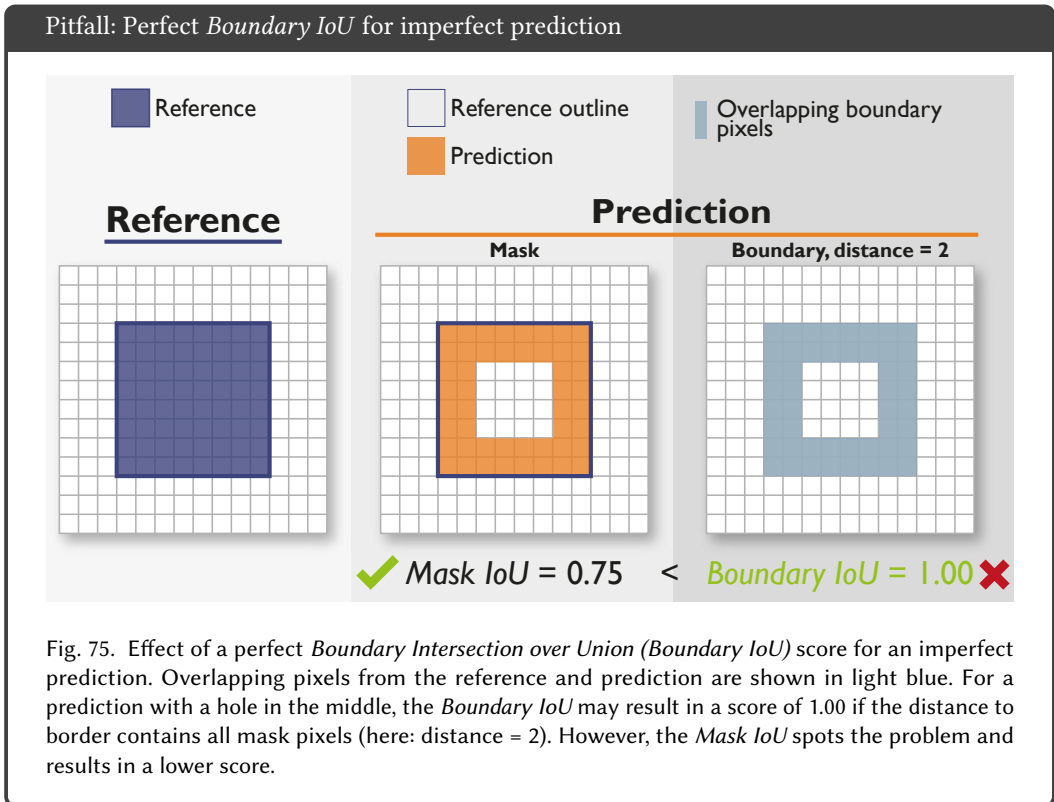
Effect of small structures on localization criterion. *Box IoU* and *Mask IoU* are not sensitive to structure boundary quality in larger objects (cf. Section 5). This is due to the fact that boundary pixels will increase linearly (quadratically in 3D) while pixels inside the structure will increase quadratically (cubically in 3D) with an increase in structure size. In consequence, the *IoU*-scores tend to be higher for large objects compared to small objects. For this reason, localization criteria such as the **Boundary IoU** were designed.

Figure 74 shows an example of *Mask IoU* and *Boundary IoU* for a large (top) and a rather small structure (bottom). In the case of the *Mask IoU*, the score drops substantially for the small structure, while the scores are more consistent for the *Boundary IoU* when comparing small and large structures. This pitfall also applies to segmentation problems in which the (*Mask*) *IoU* and *Boundary IoU* are applied as overlap-based metrics.



It should further be noted that the *Boundary IoU* is highly dependent on the chosen distance d , as illustrated in Figure 74 (third vs fourth column). Similarly to the example provided in Figure 59, the *Boundary IoU* can be fooled to result in a perfect value of 1.0. A prediction with a hole in

the middle of the structure may result in a perfect metric score if the distance is chosen in a way that it incorporates all pixels of the predicted mask, as shown in Figure 75 [14]. The *Mask IoU*, however, will be able to recognize the problem, as it completely measures the overlap between both structures. [14] propose to use the $\min(\text{BoundaryIoU}, \text{MaskIoU})$ to resolve this issue. Please note that the same limitations also affect other distance-based measures, such as the *NSD* or *HD* metrics. This pitfall also applies to segmentation tasks.



Possibility of reference/prediction without the target structure and NaN handling. When validating an object detection problem per image rather than per data set, a reference or prediction image without the target structure(s) may become problematic as some metric values will turn into NaN due to division by zero errors (cf. Figure 64). Figure 76a shows potential scenarios for a validation per image categorized by the presence and absence of TP, FP and FN. Four occurrences of NaN are presented. To proceed with the validation, namely aggregating metric values for every image over the entire data set, a NaN strategy needs to be defined for every use case.

Pitfall: Not A Number (NaN) handling for empty reference/prediction

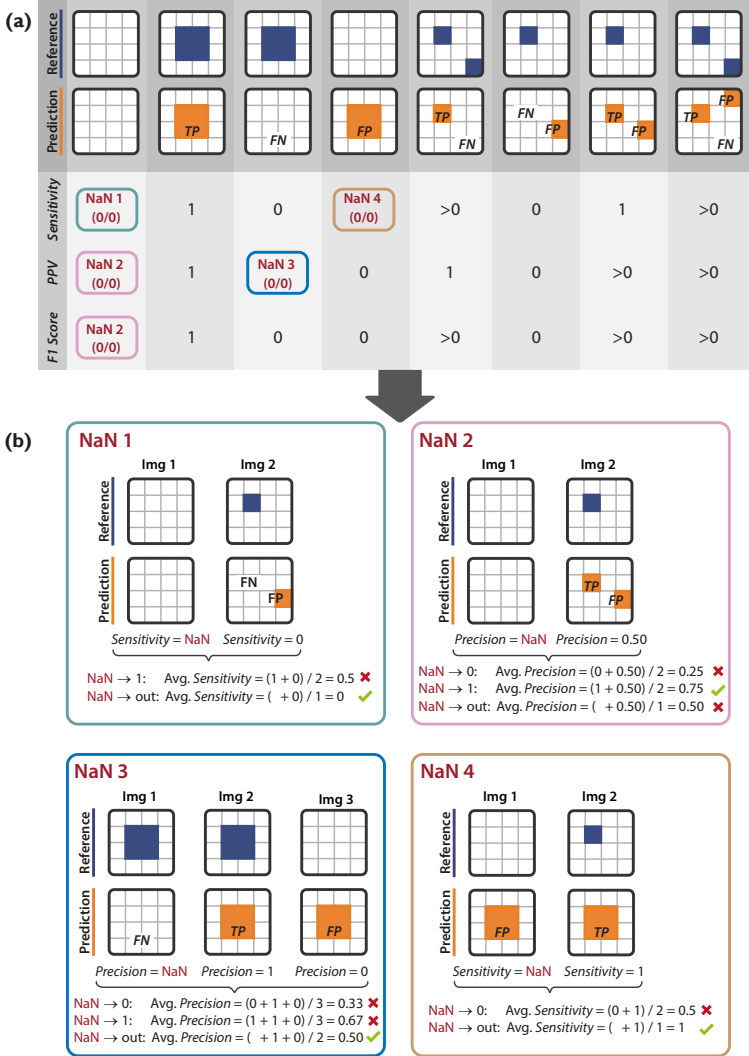
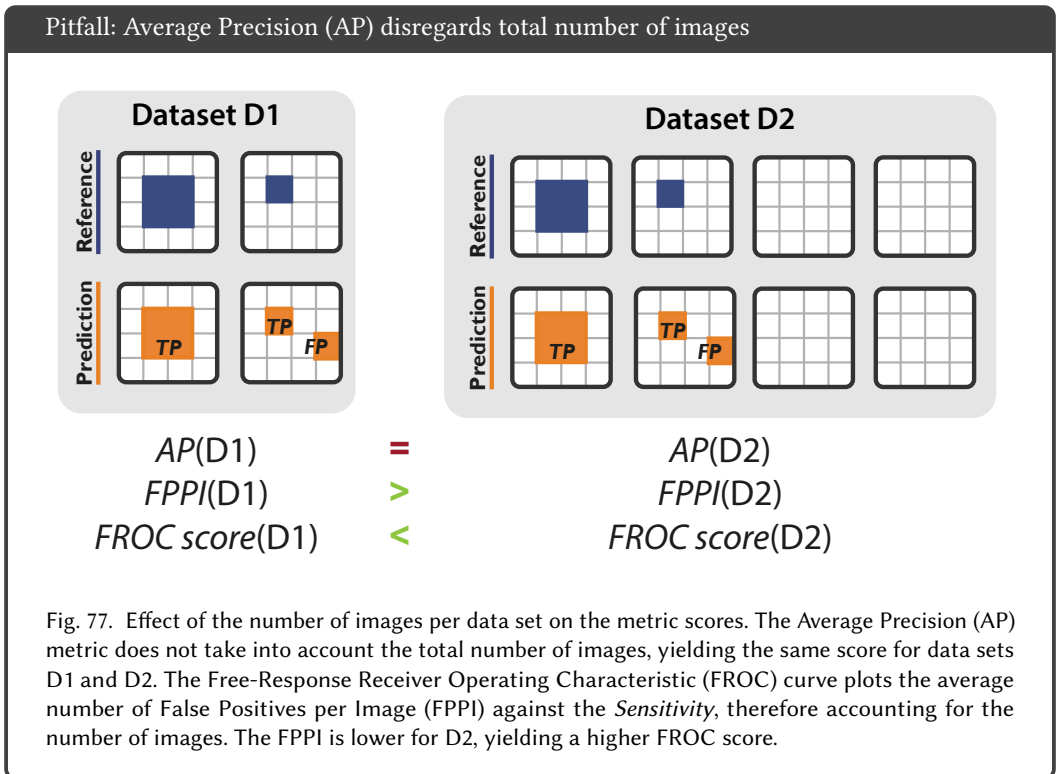


Fig. 76. Effect of handling a Not A Number (NaN) caused by reference or prediction without target structure(s) in object detection/instance segmentation problems validated per image. **(a)** Demonstration of how and when NaN can occur. Each column represents a potential scenario for per-image validation of objects, categorized by whether True Positive (TP), False Negative (FN), and False Positive (FP) are present ($n > 0$) or not present ($n = 0$) after matching/assignment. The sketches on the top showcase each scenario when setting " $n > 0$ " to " $n = 1$ ". For each scenario, *Sensitivity*, *Positive Predictive Value (PPV)* and *F1 Score* are calculated. Some scenarios yield undefined values (Not A Number (NaN)). **(b)** Effect of different NaN handling strategies based on different conventions for the aggregation across multiple images. Four examples are shown for the NaN scenarios from (a) (NaN 1-4). **NaN 1** and **4**: The intuitive penalization for FPs in "empty" images is already established by means of *PPV* scores (see **NaN 4**) and further penalization by means of *Sensitivity* is neither required nor appropriate. Instead, images without reference objects should be ignored when averaging *Sensitivity* scores over images. **NaN 2**: The intuitive penalization for FP in "empty" images is established when assigning a *PPV* (and *F1 Score*) of 1. **NaN 3**: The intuitive penalization for FP is established when removing images with FN and no FP from the aggregation of *PPV* (and *F1*) scores.

Average Precision vs. Free-response ROC score. While the AP constitutes the standard metric for object detection and instance segmentation in the computer vision community, the *FROC* score is often favoured in the clinical context. In contrast to the AP, the *FROC* score takes into account the total number of images in the data set. As can be seen from Figure 77, both data sets D1 and D2 will yield the same AP score, although data set D1 contains two images and D2 contains four images. The *FROC* score, however, will reflect that the number of images is different for both data sets and that data set D2 contains two images that do not contain any FP. Thus, the FPPI will be lower in data set D2, yielding a higher *FROC* score.



FROC is not standardized. Although the *FROC Score* is often favored by clinicians over the *AP* given its simpler interpretation, it comes with a major drawback. While the values of the x-axis are clearly defined and bounded between 0 and 1 for the *AP*, there is no fixed or standardized definition for the *FPPI* used for the *FROC* curve. Depending on the defined range of the *FPPI*, the *FROC Score* will change. Figure 78 shows three examples of different bounds for the x-axes (left: [0, 1], middle: [0, 2], right: [0, 4]) for the same prediction – all of them yielding different *FROC Scores*.

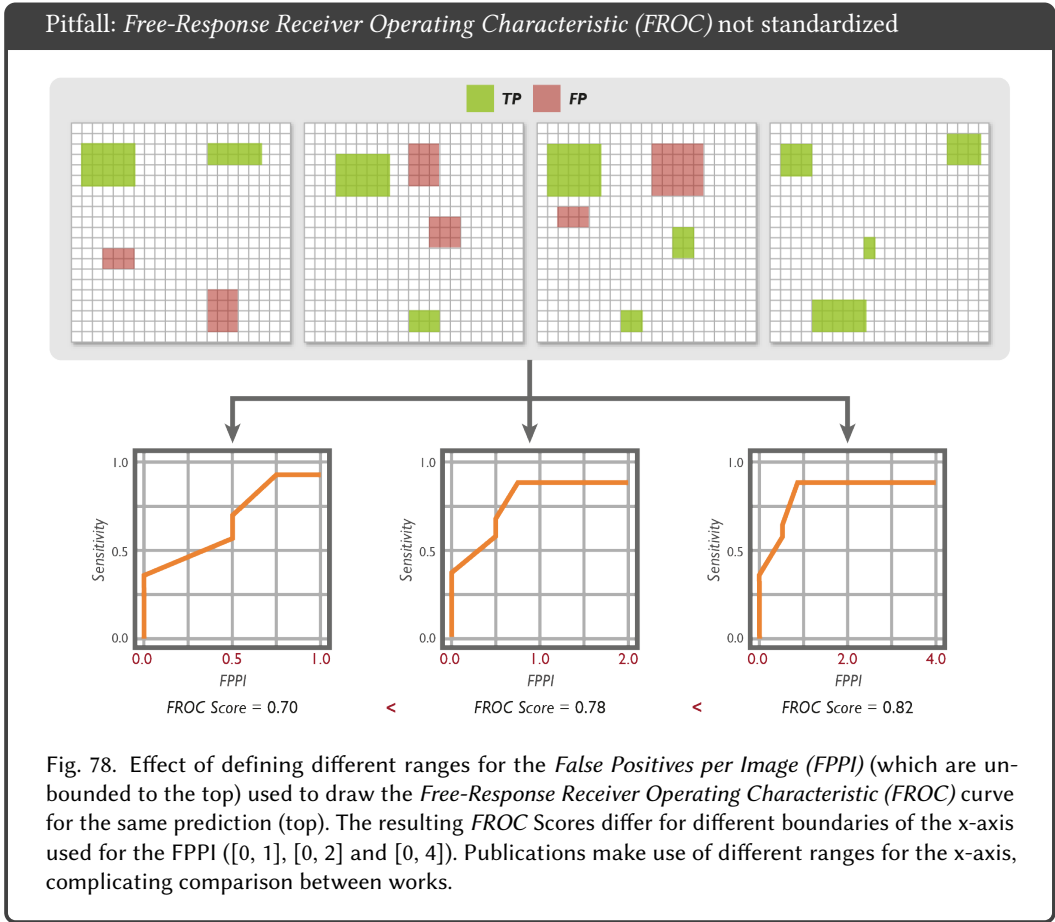
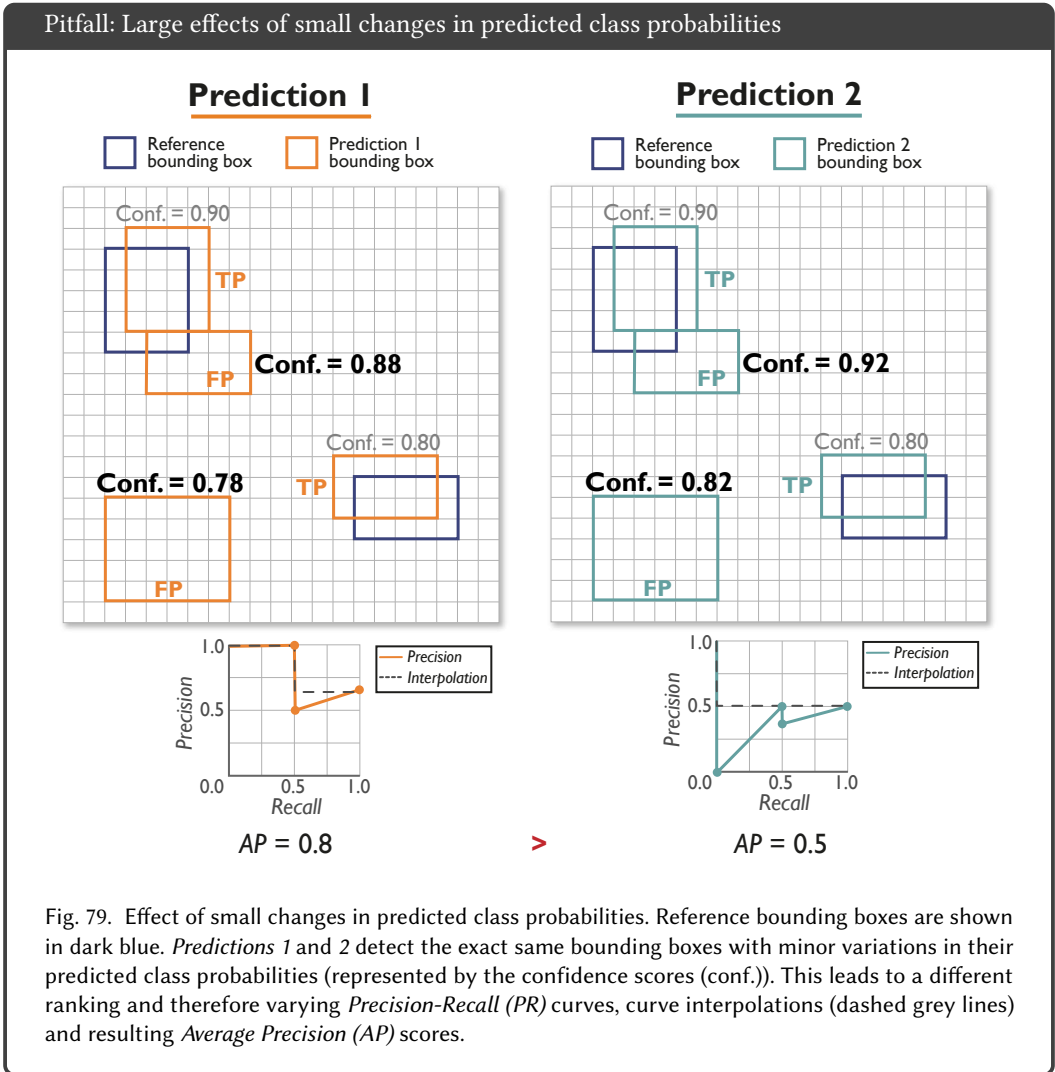
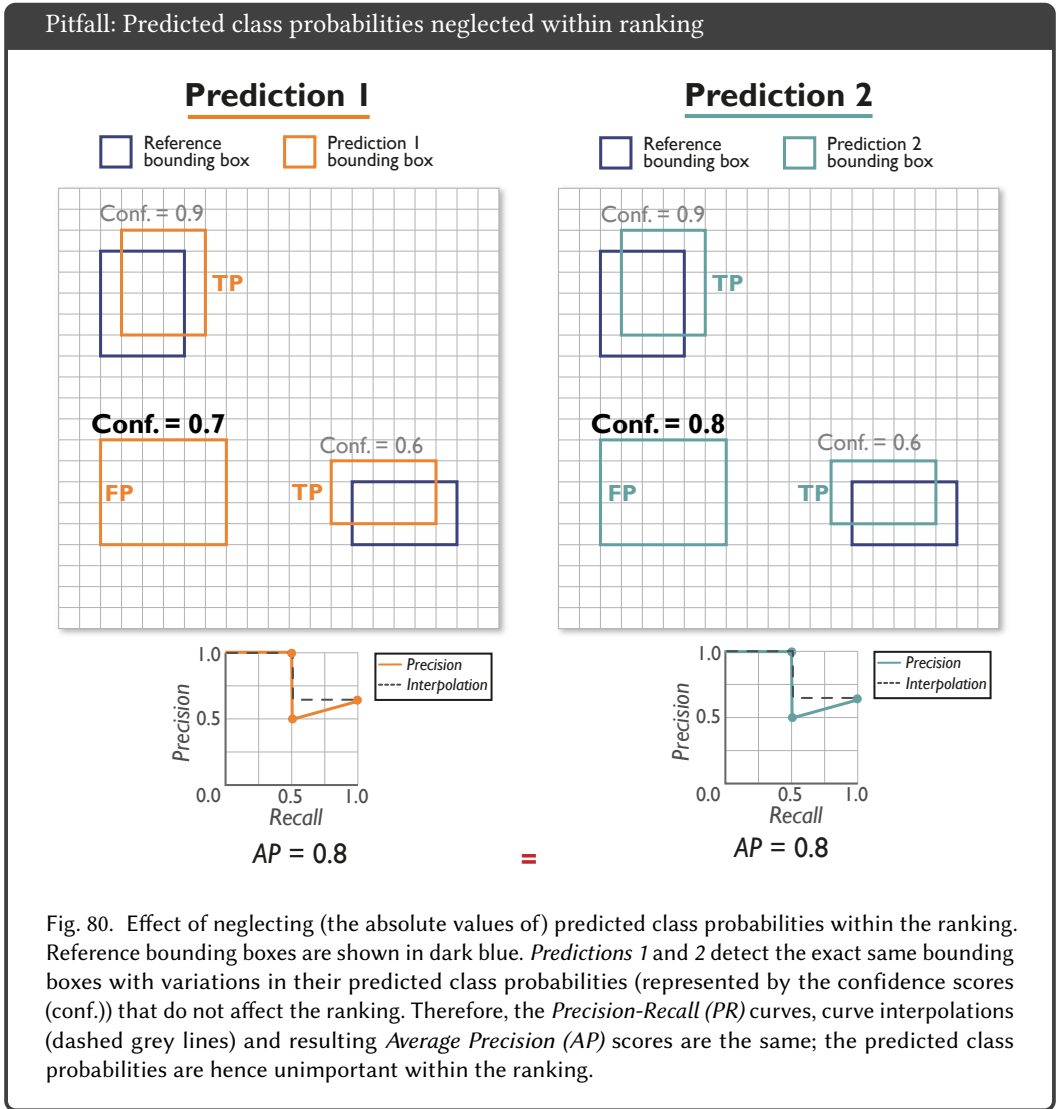


Fig. 78. Effect of defining different ranges for the *False Positives per Image (FPPI)* (which are unbounded to the top) used to draw the *Free-Response Receiver Operating Characteristic (FROC)* curve for the same prediction (top). The resulting *FROC Scores* differ for different boundaries of the x-axis used for the *FPPI* ([0, 1], [0, 2] and [0, 4]). Publications make use of different ranges for the x-axis, complicating comparison between works.

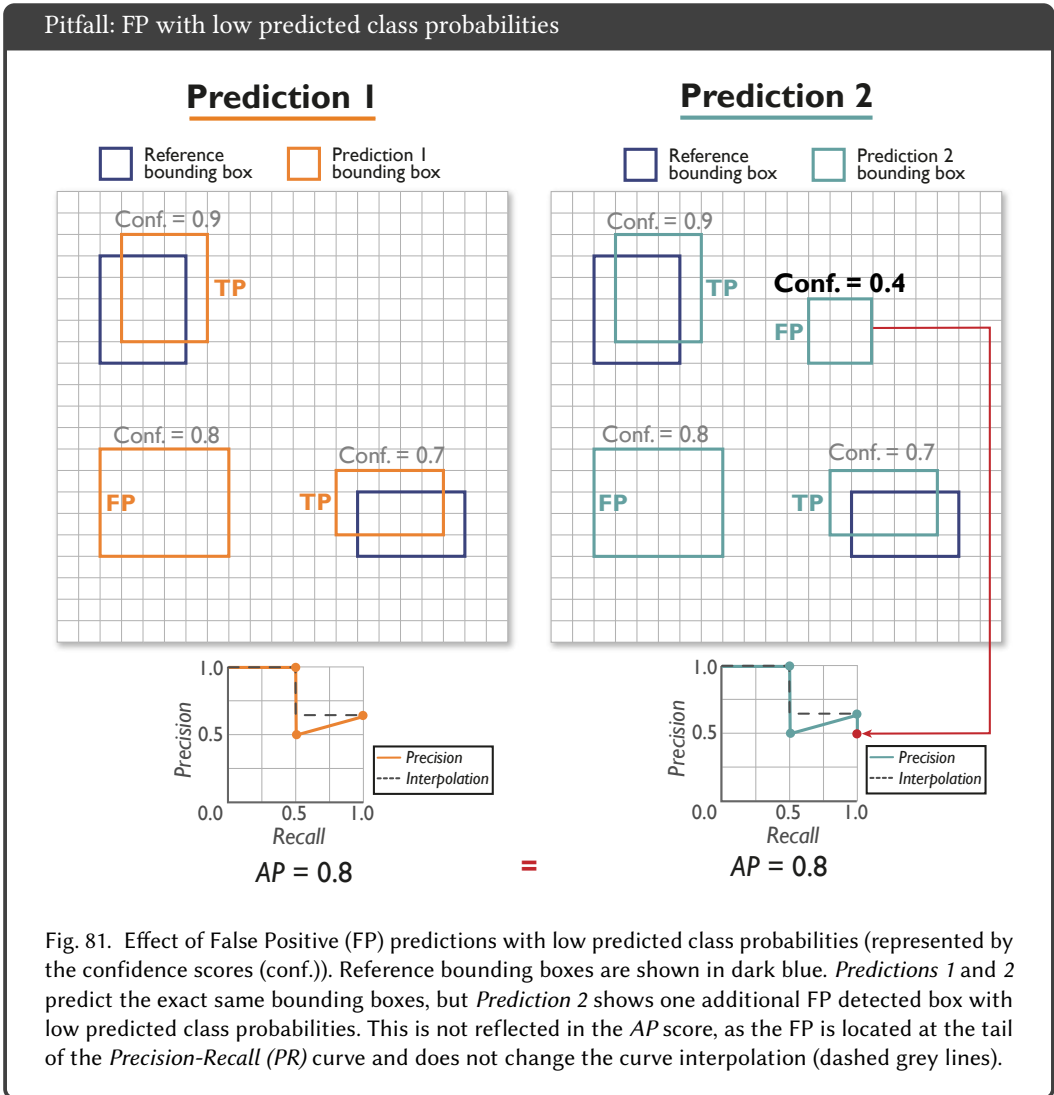
Multi-threshold metric-related properties. In the next paragraphs, we highlight some limitations of the multi-threshold metrics, exemplarily for the *AP* metric, which can be transferred to other multi-threshold metrics, such as the *AUROC* [68]. By definition, multi-threshold metrics are ranking metrics, which rank the predicted class probabilities or confidence scores (cf. Figure 15). They are not designed to reflect the calibration of confidence or class scores, as shown in the following examples. Please note that we disregard the concrete choice of the localization criterion here for simplicity.

Predicted class probabilities. The *PR* curve and the resulting metric score *AP* highly depend on the ranking of predictions, based on their predicted class probabilities or confidence scores. Small changes in the scores can therefore significantly change the metric value, as shown in Figure 79. On the other hand, as long as the ranking remains unchanged among predictions, the predicted class probabilities themselves are not important for the result, although they should be (see Figure 80).





FP with low predicted class probabilities. False positive predictions with lower predicted class probabilities than the last correctly predicted reference, corresponding to the end of the *PR* curve, do not affect the *AP* scores. Figure 81 shows two examples that are very similar, only differing in the number of wrongly predicted objects. *Prediction 2*, with two FP, performs worse than *Prediction 1* with only one FP. Nevertheless, the *AP* scores are the same for both models, given the low confidence of the second FP of *Prediction 2*. Thus, a prediction may contain numerous FP objects with low confidence scores, but still yield a deceptively high *AP* score, as this practice only increases the score but never decreases it by potentially hitting more reference objects.



Non-standardized metric definition. Standard metric implementations do not always cover corner cases or handle them differently. For example, for the creation of the PR-curve and the subsequent computation of the *AP* metric, predictions are typically ranked by their predicted class scores. Duplicate predicted class scores can either be computed in a single step per score or can all be treated together in a common step. Based on the chosen implementation, the PR-curve will differ in appearance, causing a sometimes substantial change in the *AP* scores. Figure 82a provides such an example, in which the final scores differ by 0.06 solely because of two predictions having the same score.

This difference in implementation is even more critical in the extreme case of all predictions having the same score (e.g., if no class scores are available; see Figure 82b). However, it should be noted that although this practice is not uncommon (e.g., [3, 21, 27, 37, 53]), multi-threshold metrics such as the *AP* should generally be avoided if no class scores are available. Moreover, some implementations force the PR-curve to start at the point (0, 1), i.e., to always start with a *PPV* value of 1 instead of the actual first *PPV* value that was computed. This may lead to a substantial overestimation if there are no confidence scores or if the number of instances is low.

Undefined corner cases yield variations in metric scores

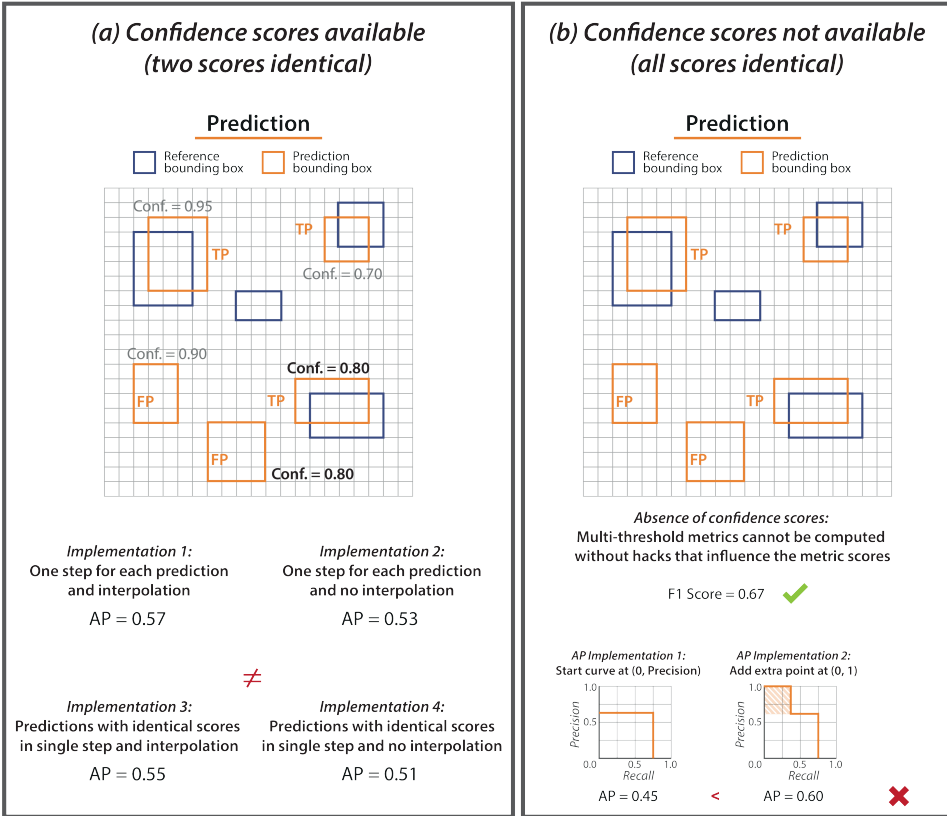


Fig. 82. (a) Non-standardized metric implementation. In the case of the *Average Precision (AP)* metric and the construction of the *Precision-Recall (PR)*-curve, the strategy of how identical scores (here: confidence score of 0.80 is present twice) are treated has a substantial impact on the metric scores. Microsoft Common Objects in Context (COCO) [54] and CityScapes [18] are used as examples. (b) Multi-threshold metrics should only be computed if predicted class scores are available, although an increasing body of work computes multi-threshold metrics such as *AP* in the absence of class scores (e.g. [3, 21, 27, 37, 53]). Otherwise, the strategy chosen for compensating the lack of class scores (here reflected by *Implementations 1* and *2*) leads to metric scores that are less well interpretable than those of established counting metrics working on a fixed confusion matrix (here: F_1 Score).

7 PITFALLS RELATED TO ANALYSES AND POST-PROCESSING

A data set typically contains several hundreds or thousands of images. When analyzing, aggregating and combining metric values, a number of factors need to be taken into account. Pitfalls in this step are primarily related to the following aspects:

- Uninformative visualization (Figure 83)
- Metric aggregation for invalid algorithm output (e.g. NaN) (Figures 84 - 85)
- Hierarchical data aggregation (Figure 86)
- Aggregation in the presence of multiple classes (Figure 87)
- Combination of related metrics (Figure 88)
- Ranking uncertainty (Fig 89)
- Insufficient biomedical relevance of metric score differences (Fig 90)
- Non-determinism of algorithms (Fig 91)
- Non-standardized metric implementation

Uninformative visualization. Relying on only reporting aggregated metric scores may result in missing essential information on algorithm performance. Therefore, raw metric values (e.g. per image) should always be shown, for example in the shape of boxplots, as depicted in the top left of Figure 83. However, boxplots will only provide information on some key descriptive statistics, like median or 1st and 3rd quartiles. Another choice can be violin plots, which further visualize the raw data distribution. The top right of Figure 83 illustrates the multimodal distribution of the underlying data, invisible in the boxplot. Furthermore, using a violin plot and/or plotting the raw metric values for each data point on top (Figure 83, top right and bottom left) will reveal the complete data distribution. In the example below, many values lie below the 3rd quartile, although the box looks tight. Nevertheless, even these two visualizations may hide important information. Assume a data set with metric values of four different videos. Color- or shape-coding the metric values by the video type (Figure 83 bottom right) reveals a huge cluster of extremely low *DSC* values only affecting Video 4 (pink), which would have been hidden by the other two types of visualization.

Pitfall: Uninformative visualization

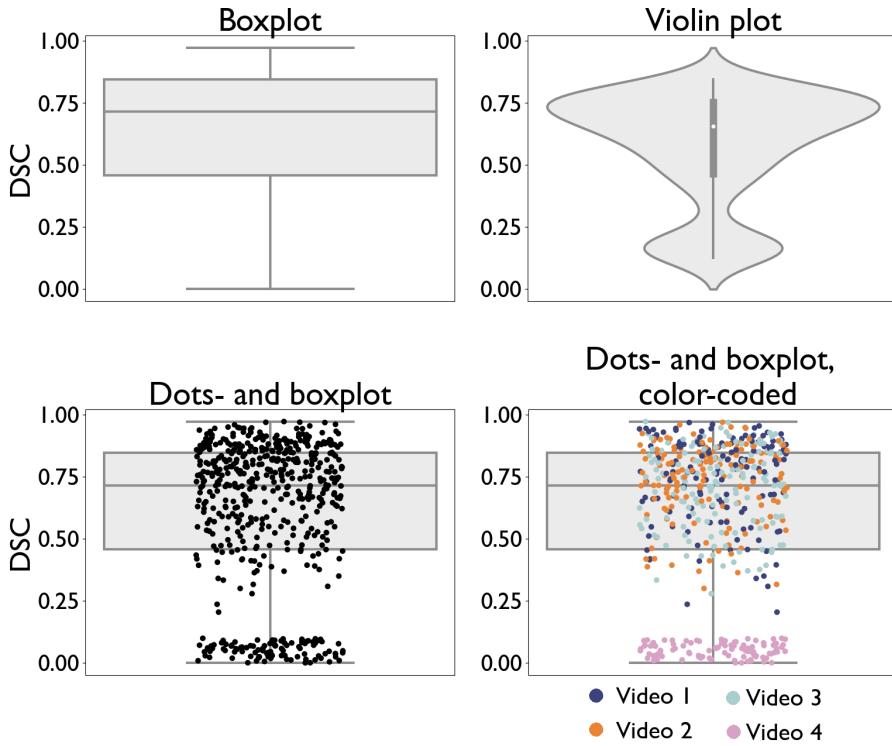
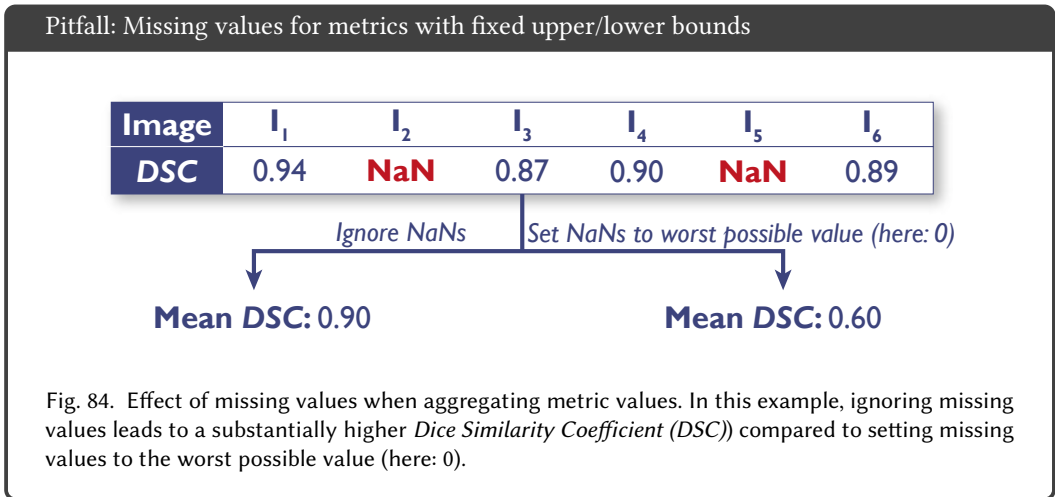


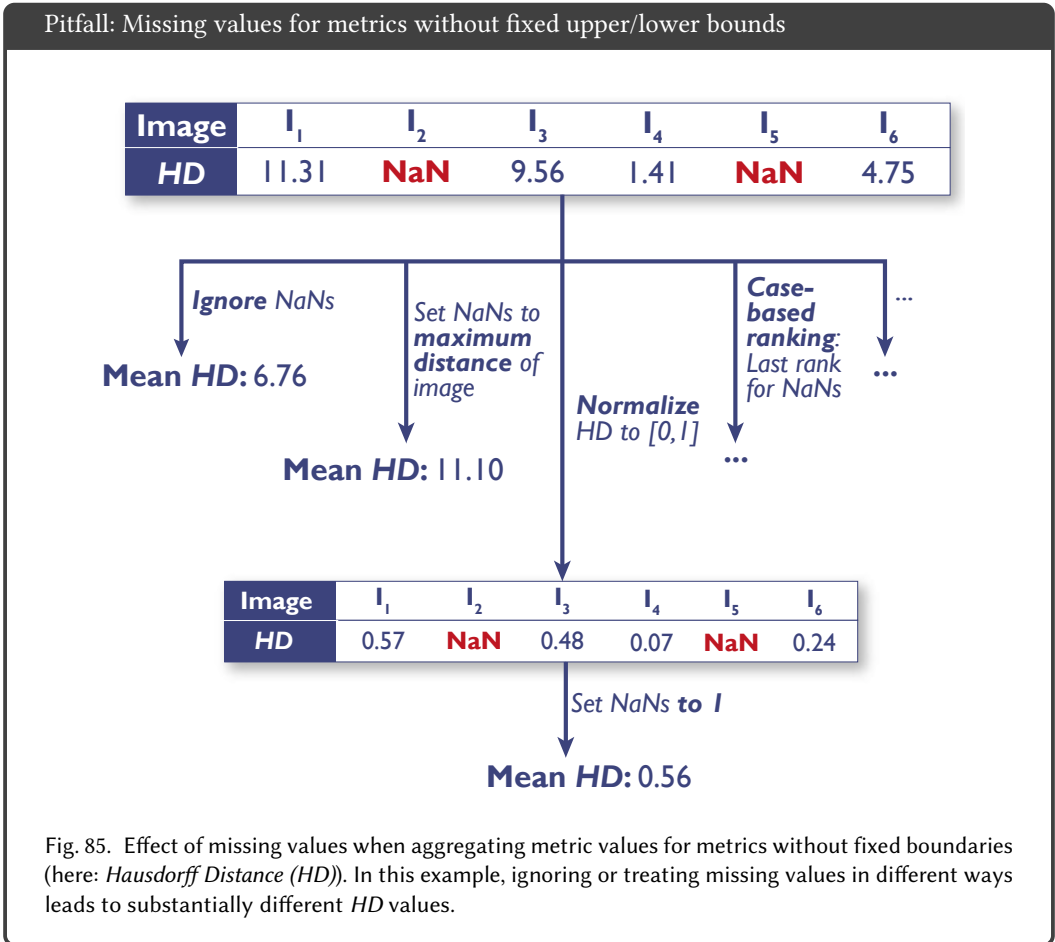
Fig. 83. Effect of different types of visualization. A single boxplot (top left) does not give sufficient information about the raw metric value distribution (here: *Dice Similarity Coefficient (DSC)*). Using a violin plot (top right) or adding the raw metric values as jittered dots on top (bottom left) adds important information. In the case of non-independent validation data, color/shape-coding helps reveal data clusters (bottom right).

Metric aggregation for invalid algorithm output (e.g. NaN). In challenges or benchmarking experiments, metric values are often aggregated over all test cases to produce a challenge ranking [56]. Missing data plays a crucial role when aggregating metric values and occurs primarily due to two reasons: invalid output of the algorithm or metric routine output resulting in NaN, and non-submission of single cases (by accident or even for cheating [71]). Figs. 84 and 85 illustrate why a strategy on how to handle missing values may be crucial.

In the case of metrics with fixed boundaries, such as the *DSC* or the *IoU*, missing values can easily be set to the worst possible value (here: 0). For spatial distance-based measures without lower/upper bounds, the strategy of how to treat missing values is not trivial. In the case of the *HD*, for example, one may choose the maximum distance of the image or normalize the metric values to [0, 1] and use the worst possible value (here: 1). Another possibility is to employ a case-based ranking scheme [56] and assign the last rank for every missing submission. Furthermore, aggregating with the mean may not be a good choice as results are unlikely to be normally distributed. Crucially, however, every choice will produce a different aggregated value (Figure 85), thus potentially affecting the ranking. Another way of handling missing values would lie in rejecting the entire submission in a challenge.

However, metric values may also be undefined (NaN) if either reference or prediction or both are empty. In the case of empty reference and prediction, an undefined metric value (e.g. *DSC*) may be a desirable outcome and should therefore not necessarily be penalized.





Hierarchical data aggregation. Nowadays, most data sets are inherently hierarchically structured, meaning that the test cases are not independent. Data may, for example, come from several centers or hospitals, and for every center or even within one, different devices may be used for image acquisition, and images may be drawn from different subjects or patients. This should be kept in mind when visualizing and aggregating data points, especially if the individual tree nodes end in a large variation in the size of images. Figure 86 shows an example of five patients with an unequal number of images associated with them. Just averaging all metric values for every image would result in a high average *DSC* of 0.8. Averaging metric values per patient reveals that the *DSC* values are much higher for *Patient 1*, overruling the other patients due to the high number of samples for this patient. Aggregating per patient first and averaging subsequently will resolve this issue.

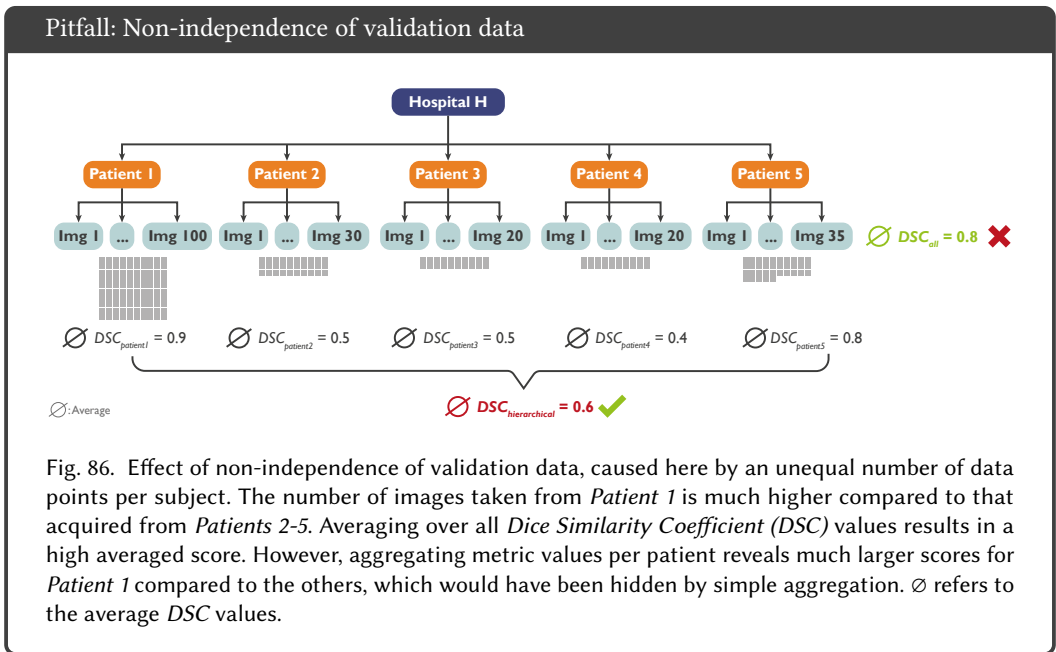
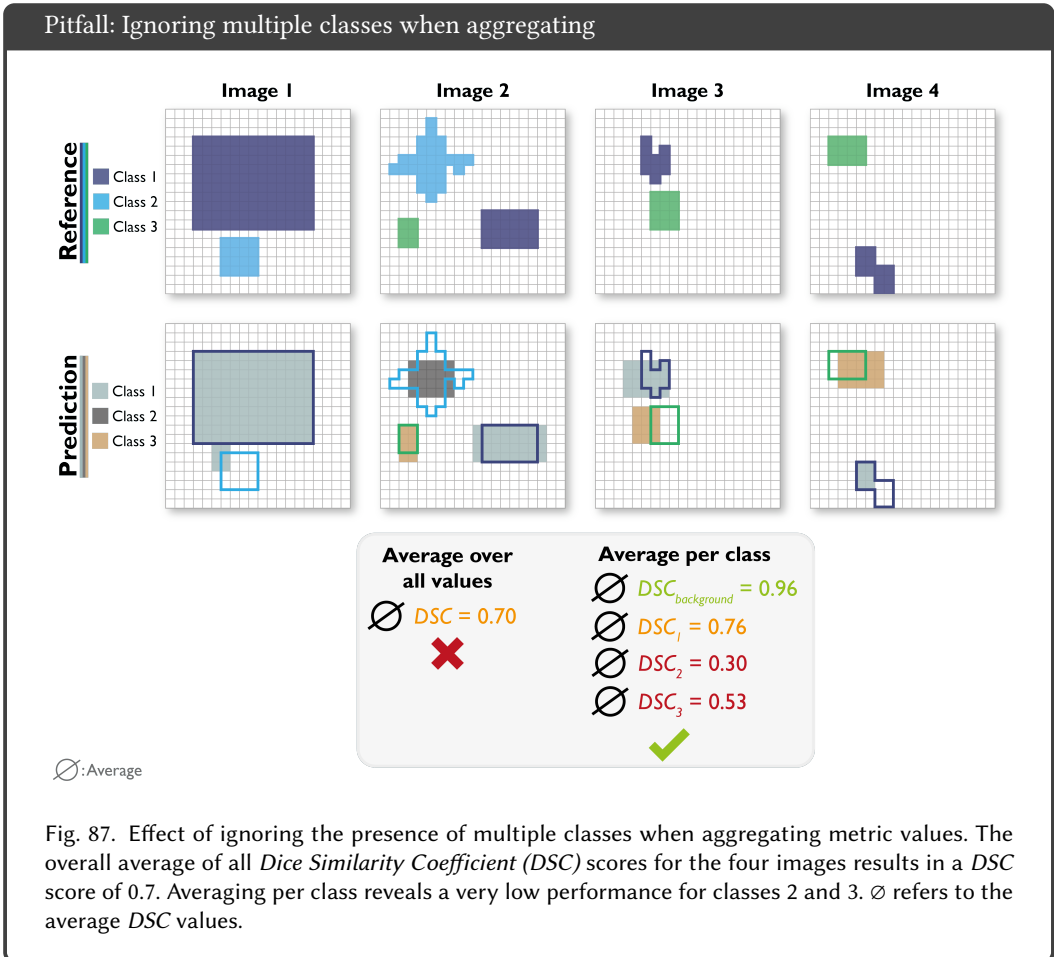


Fig. 86. Effect of non-independence of validation data, caused here by an unequal number of data points per subject. The number of images taken from *Patient 1* is much higher compared to that acquired from *Patients 2-5*. Averaging over all *Dice Similarity Coefficient (DSC)* values results in a high averaged score. However, aggregating metric values per patient reveals much larger scores for *Patient 1* compared to the others, which would have been hidden by simple aggregation. ∅ refers to the average *DSC* values.

Aggregation per class. Similar approaches should be chosen in the presence of multiple classes in a data set. The performance may differ significantly for the individual classes, as shown in Figure 87. The background class in particular will result in a nearly perfect averaged *DSC* value, whereas the average scores for classes 2 and 3 are much lower. Aggregating over all values, not considering the class, would hide this information. An alternative approach to the problem lies in the application of metrics that explicitly handle class balance, such as using the *Generalized DSC* [79].



Metric combination. A single metric typically does not reflect all aspects that are essential for algorithm validation. Hence, multiple metrics with different properties are often combined. However, the selection of metrics should be well-considered as some metrics are mathematically related to each other [81, 82]. A prominent example is the *IoU* – the most popular segmentation metric in computer vision – which highly correlates with the *DSC* – the most popular segmentation metric in medical image analysis. In fact, the *IoU* and the *DSC* are mathematically related (see Sec. 2.2) [81].

Combining metrics that are related will not provide additional information for a ranking. Figure 88 illustrates how the ranking can change when adding a metric that measures different properties.

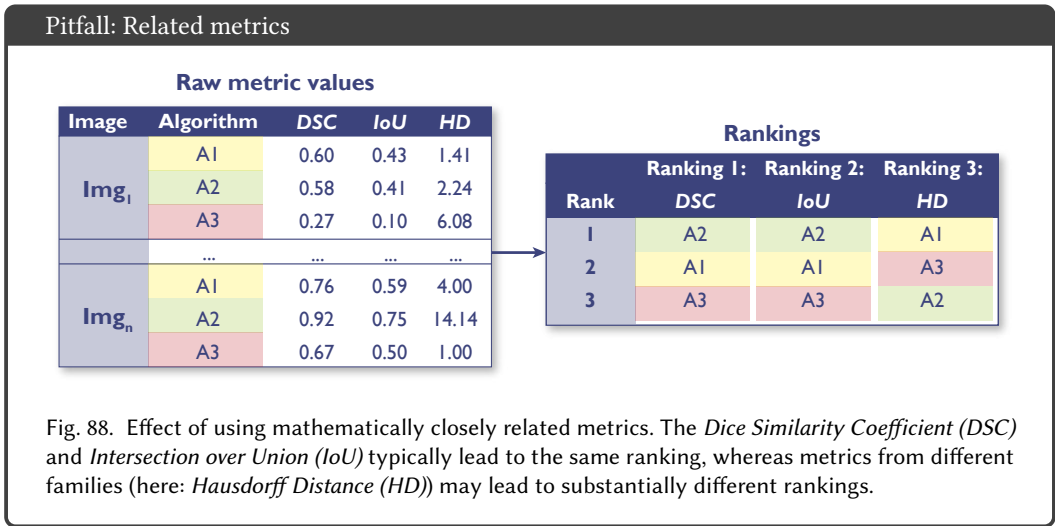
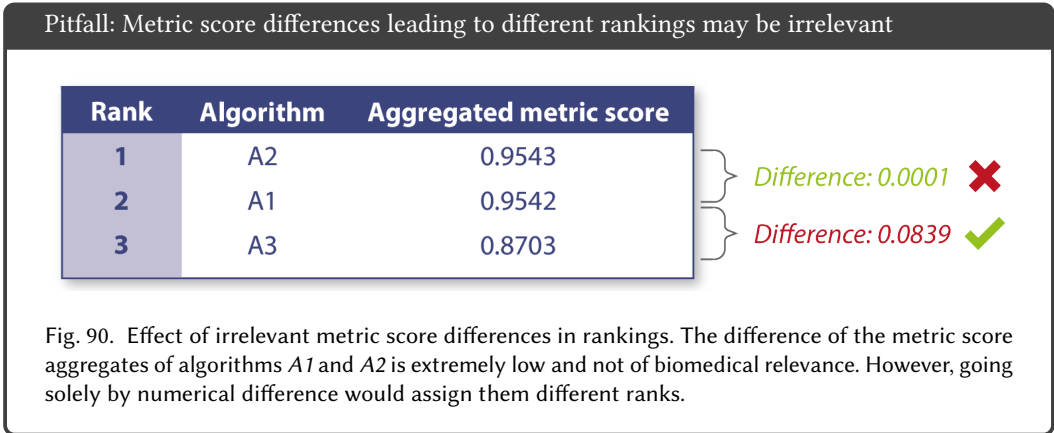


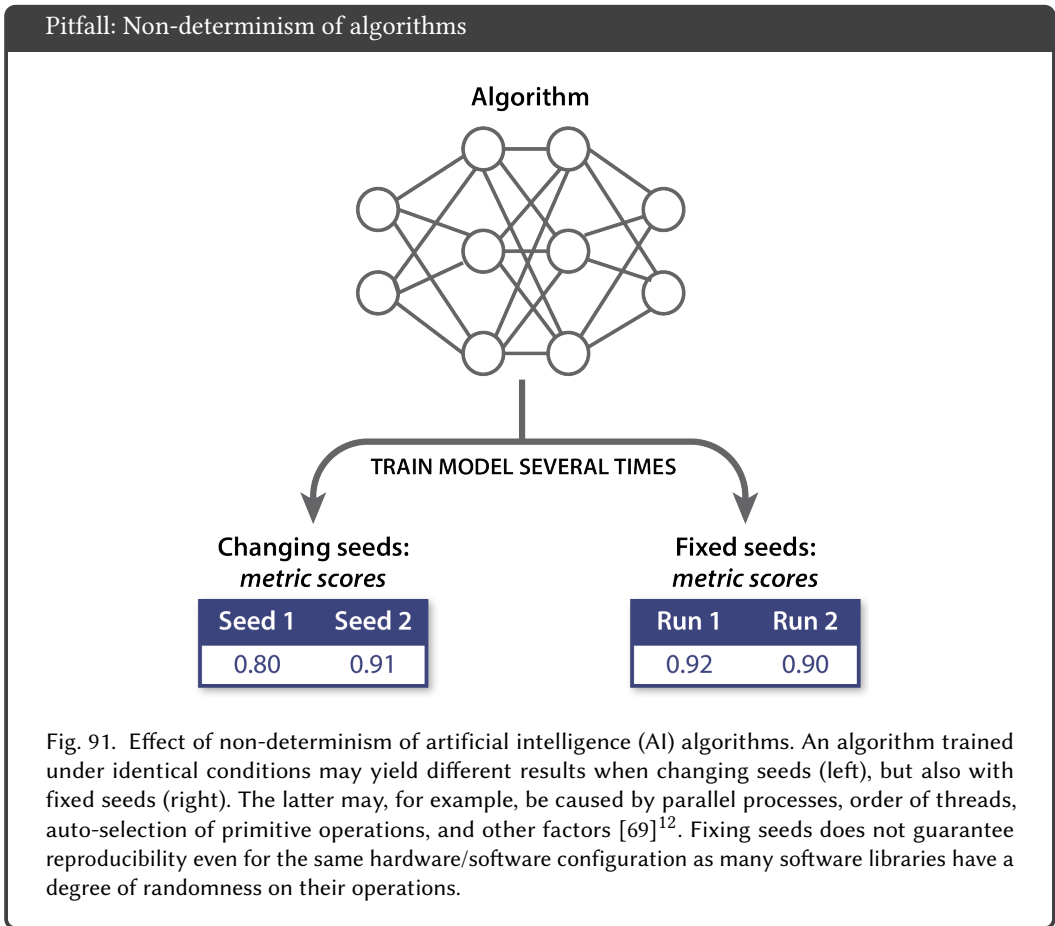
Fig. 88. Effect of using mathematically closely related metrics. The *Dice Similarity Coefficient (DSC)* and *Intersection over Union (IoU)* typically lead to the same ranking, whereas metrics from different families (here: *Hausdorff Distance (HD)*) may lead to substantially different rankings.

Ranking uncertainty. Rankings themselves may be unstable. [56] and [91] demonstrated that rankings are highly sensitive to altering the metric aggregation operators, the underlying data set, or the general ranking method. Disregarding the robustness of rankings may thus lead to the winning algorithm ranking first solely by chance rather than true superiority. Such a case is illustrated in Fig. 89. Here, the boxplots of two different benchmarking experiments are presented, one of which represents a very clear ranking, the other showing a similar performance of all five algorithms. However, both scenarios would yield the same ranking table. The common practice of solely presenting ranking tables without further visualization [91] may thus obscure important information.

Insufficient biomedical relevance of metric score differences. Rankings may be uninformative in the domain context. For example, algorithms *A1* and *A2* in Fig. 90 only differ by a very small amount (0.0001). While this difference would make one algorithm numerically superior, it may not be relevant for the actual application. Therefore, the algorithms should not receive different ranks, but rather share the same rank. On the other hand, algorithms *A2* and *A3* differ by a substantial amount, thus, ranking them differently is clinically relevant.



Non-determinism of algorithms. artificial intelligence (AI) algorithms are subject to non-determinism. When training an algorithm under identical conditions (e.g., the same libraries and architecture), results will be subject to sometimes substantial changes if the random seeds are exchanged, as shown in Fig. 91 (left). Although fixing random seeds will reduce the variability of results, there may still be differences in metric scores, for example caused by parallel processing [69] or usage of more than two Graphics Processing Units (GPUs).



Non-standardized metric implementation. Metric implementation is typically not standardized, as can for instance be seen in Figures 78 and 82. This was further highlighted in a study presented in [31], in which the authors analyzed the differences between how metric implementations differ and their implications. The authors found, for example, that seven out of thirteen distinct methods were used for sampling the surface for distance-based metrics such as *HD* or that the thirteen participants of the study used five different definitions for the symmetric average distance [31]. It was further shown that these differences result in a high variation in the final metric score, for instance of up to 9% in the *DSC* and of up to 40% for the *HD* metric [31].

¹²See for example: <https://pytorch.org/docs/stable/notes/randomness.html>

8 CONCLUSION

Choosing the right metric for a specific image processing task is a nontrivial undertaking. With this (dynamic) paper, we wish to raise awareness about some of the common flaws of the most frequently used reference-based validation metrics in the field of image processing and provide guidance of their use, encouraging researchers to reconsider common workflows.

9 ACKNOWLEDGEMENTS

This work was initiated by the Helmholtz Association of German Research Centers in the scope of the Helmholtz Imaging Incubator (HI), the MICCAI Special Interest Group on biomedical image analysis challenges and the benchmarking working group of the MONAI initiative. It received funding from the European Research Council (ERC) under the European Union's Horizon 2020 research and innovation programme (grant agreement No. [101002198], NEURAL SPICING). It was further supported in part by the Intramural Research Program of the National Institutes of Health (NIH) Clinical Center as well as by the National Cancer Institute (NCI) and the National Institute of Neurological Disorders and Stroke (NINDS) of the NIH, under award numbers NCI:U01CA242871 and NINDS:R01NS042645. The content of this publication is solely the responsibility of the authors and does not represent the official views of the NIH. T.A. acknowledges the Canada Institute for Advanced Research (CIFAR) AI Chairs program, the Natural Sciences and Engineering Research Council of Canada. F.B. was co-funded by the European Union (ERC, TAIPO, 101088594). Views and opinions expressed are however those of the authors only and do not necessarily reflect those of the European Union or the European Research Council. Neither the European Union nor the granting authority can be held responsible for them. V.C. acknowledges funding from NovoNordisk Foundation (NNF21OC0068816) and Independent Research Council Denmark (1134-00017B). B.A.C. was supported by NIH grant P41 GM135019 and grant 2020-225720 from the Chan Zuckerberg Initiative DAF, an advised fund of the Silicon Valley Community Foundation. G.S.C. was supported by Cancer Research UK (programme grant: C49297/A27294). M.M.H. is supported by the Natural Sciences and Engineering Research Council of Canada (RGPIN-2022-05134). A.Kara. is supported by French State Funds managed by the "Agence Nationale de la Recherche (ANR)" - "Investissements d'Avenir" (Investments for the Future), Grant ANR-10-IAHU-02 (IHU Strasbourg). M.K. was supported by the Ministry of Education, Youth and Sports of the Czech Republic (Project LM2018129). T.K. was supported in part by 4UH3-CA225021-03, 1U24CA180924-01A1, 3U24CA215109-02, and 1UG3-CA225-021-01 grants from the National Institutes of Health. G.L. receives research funding from the Dutch Research Council, the Dutch Cancer Association, HealthHolland, the European Research Council, the European Union, and the Innovative Medicine Initiative. S.M.R. wishes to acknowledge the Allen Institute for Cell Science founder Paul G. Allen for his vision, encouragement and support. C.H.S. is supported by an Alzheimer's Society Junior Fellowship (AS-JF-17-011). M.R. is supported by Innosuisse grant number 31274.1 and Swiss National Science Foundation Grant Number 205320_212939. R.M.S. is supported by the Intramural Research Program of the NIH Clinical Center. A.T. acknowledges support from Academy of Finland (Profi6 336449 funding program), University of Oulu strategic funding, Finnish Foundation for Cardiovascular Research, Wellbeing Services County of North Ostrobothnia (VTR project K62716), and Terttu foundation. S.A.T. acknowledges the support of Canon Medical and the Royal Academy of Engineering and the Research Chairs and Senior Research Fellowships scheme (grant RCSRF1819\8\25). B.V.C. was supported by Research Foundation Flanders (FWO grant G097322N) and Internal Funds KU Leuven (grant C24M/20/064).

We would like to thank Amine Yamlahi, Niklas Holzwarth, Marco Hübner, Amith Kamath, Dominik Michael, You Suhang, and Yannick Suter for proofreading the document and proposing pitfalls.

REFERENCES

- [1] Shadi AlZu'bi, Mohammed Shehab, Mahmoud Al-Ayyoub, Yaser Jararweh, and Brij Gupta. Parallel implementation for 3d medical volume fuzzy segmentation. *Pattern Recognition Letters*, 130:312–318, 2020.
- [2] Saeid Asgari Taghanaki, Kumar Abhishek, Joseph Paul Cohen, Julien Cohen-Adad, and Ghassan Hamarneh. Deep semantic segmentation of natural and medical images: a review. *Artificial Intelligence Review*, 54(1):137–178, 2021.
- [3] Min Bai and Raquel Urtasun. Deep watershed transform for instance segmentation. In *Proceedings of the IEEE conference on computer vision and pattern recognition*, pages 5221–5229, 2017.
- [4] D Bamira and MH Picard. Imaging: Echocardiology—assessment of cardiac structure and function. 2018.
- [5] Solon Barocas, Moritz Hardt, and Arvind Narayanan. Fairness in machine learning. *Nips tutorial*, 1:2, 2017.
- [6] Miroslav Beneš and Barbara Zitová. Performance evaluation of image segmentation algorithms on microscopic image data. *Journal of microscopy*, 257(1):65–85, 2015.
- [7] Glenn W Brier et al. Verification of forecasts expressed in terms of probability. *Monthly weather review*, 78(1):1–3, 1950.
- [8] Bernice B Brown. Delphi process: a methodology used for the elicitation of opinions of experts. Technical report, Rand Corp Santa Monica CA, 1968.
- [9] JB Brown. Classifiers and their metrics quantified. *Molecular informatics*, 37(1-2):1700127, 2018.
- [10] Neil G Burnet, Simon J Thomas, Kate E Burton, and Sarah J Jefferies. Defining the tumour and target volumes for radiotherapy. *Cancer Imaging*, 4(2):153, 2004.
- [11] Chang Cao, Davide Chicco, and Michael M Hoffman. The mcc-f1 curve: a performance evaluation technique for binary classification. *arXiv preprint arXiv:2006.11278*, 2020.
- [12] Aaron Carass, Snehashis Roy, Adrian Gherman, Jacob C Reinhold, Andrew Jesson, Tal Arbel, Oskar Maier, Heinz Handels, Mohsen Ghafoorian, Bram Platel, et al. Evaluating white matter lesion segmentations with refined sørensen-dice analysis. *Scientific reports*, 10(1):1–19, 2020.
- [13] Dev P Chakraborty and Xuetong Zhai. Analysis of data acquired using roc paradigm and its extensions, 2019.
- [14] Bowen Cheng, Ross Girshick, Piotr Dollár, Alexander C Berg, and Alexander Kirillov. Boundary iou: Improving object-centric image segmentation evaluation. In *Proceedings of the IEEE/CVF Conference on Computer Vision and Pattern Recognition*, pages 15334–15342, 2021.
- [15] Davide Chicco and Giuseppe Jurman. The advantages of the matthews correlation coefficient (mcc) over f1 score and accuracy in binary classification evaluation. *BMC genomics*, 21(1):1–13, 2020.
- [16] Davide Chicco, Niklas Tötsch, and Giuseppe Jurman. The matthews correlation coefficient (mcc) is more reliable than balanced accuracy, bookmaker informedness, and markedness in two-class confusion matrix evaluation. *BioData mining*, 14(1):1–22, 2021.
- [17] Nancy R Cook. Use and misuse of the receiver operating characteristic curve in risk prediction. *Circulation*, 115(7):928–935, 2007.
- [18] Marius Cordts, Mohamed Omran, Sebastian Ramos, Timo Scharwächter, Markus Enzweiler, Rodrigo Benenson, Uwe Franke, Stefan Roth, and Bernt Schiele. The cityscapes dataset. In *CVPR Workshop on The Future of Datasets in Vision*, 2015.
- [19] Paulo Correia and Fernando Pereira. Video object relevance metrics for overall segmentation quality evaluation. *EURASIP Journal on Advances in Signal Processing*, 2006:1–11, 2006.
- [20] Jesse Davis and Mark Goadrich. The relationship between precision-recall and roc curves. In *Proceedings of the 23rd international conference on Machine learning*, pages 233–240, 2006.
- [21] Bert De Brabandere, Davy Neven, and Luc Van Gool. Semantic instance segmentation with a discriminative loss function. *arXiv preprint arXiv:1708.02551*, 2017.
- [22] Jeffrey De Fauw, Joseph R Ledsam, Bernardino Romera-Paredes, Stanislav Nikolov, Nenad Tomasev, Sam Blackwell, Harry Askham, Xavier Glorot, Brendan O'Donoghue, Daniel Visentin, et al. Clinically applicable deep learning for diagnosis and referral in retinal disease. *Nature medicine*, 24(9):1342–1350, 2018.
- [23] Elizabeth R DeLong, David M DeLong, and Daniel L Clarke-Pearson. Comparing the areas under two or more correlated receiver operating characteristic curves: a nonparametric approach. *Biometrics*, pages 837–845, 1988.
- [24] Lee R Dice. Measures of the amount of ecologic association between species. *Ecology*, 26(3):297–302, 1945.
- [25] Bruno Dujardin, Jef Van den Ende, Alfons Van Gompel, Jean-Pierre Unger, and Patrick Van der Stuyft. Likelihood ratios: a real improvement for clinical decision making? *European journal of epidemiology*, 10(1):29–36, 1994.

- [26] Mark Everingham, SM Ali Eslami, Luc Van Gool, Christopher KI Williams, John Winn, and Andrew Zisserman. The pascal visual object classes challenge: A retrospective. *International journal of computer vision*, 111(1):98–136, 2015.
- [27] Naiyu Gao, Yanhu Shan, Yupei Wang, Xin Zhao, Yinan Yu, Ming Yang, and Kaiqi Huang. Ssap: Single-shot instance segmentation with affinity pyramid. In *Proceedings of the IEEE/CVF International Conference on Computer Vision*, pages 642–651, 2019.
- [28] Manuel Emilio Gegúndez-Arias, Arturo Aquino, José Manuel Bravo, and Diego Marín. A function for quality evaluation of retinal vessel segmentations. *IEEE transactions on medical imaging*, 31(2):231–239, 2011.
- [29] Tilmann Gneiting and Adrian E Raftery. Strictly proper scoring rules, prediction, and estimation. *Journal of the American statistical Association*, 102(477):359–378, 2007.
- [30] Mark J Gooding, Annamaria J Smith, Maira Tariq, Paul Aljabar, Devis Peressutti, Judith van der Stoep, Bart Reymen, Daisy Emans, Djoya Hattu, Judith van Loon, et al. Comparative evaluation of autocontouring in clinical practice: a practical method using the turing test. *Medical physics*, 45(11):5105–5115, 2018.
- [31] Mark J Gooding, Djamel Boukerroui, Eliana Vasquez Osorio, René Monshouwer, and Ellen Brunenberg. Multicenter comparison of measures for quantitative evaluation of contouring in radiotherapy. *Physics and Imaging in Radiation Oncology*, 24:152–158, 2022.
- [32] Margherita Grandini, Enrico Bagli, and Giorgio Visani. Metrics for multi-class classification: an overview. *arXiv preprint arXiv:2008.05756*, 2020.
- [33] Sebastian Gruber and Florian Buettner. Trustworthy deep learning via proper calibration errors: A unifying approach for quantifying the reliability of predictive uncertainty. *arXiv preprint arXiv:2203.07835*, 2022.
- [34] Chuan Guo, Geoff Pleiss, Yu Sun, and Kilian Q Weinberger. On calibration of modern neural networks. In *International conference on machine learning*, pages 1321–1330. PMLR, 2017.
- [35] Chuan Guo, Geoff Pleiss, Yu Sun, and Kilian Q Weinberger. On Calibration of Modern Neural Networks. *ICML*, page 10, 2017.
- [36] Steven Hicks, Inga Strüke, Vajira Thambawita, Malek Hammou, Pål Halvorsen, Michael Riegler, and Sravanthi Parasa. On evaluation metrics for medical applications of artificial intelligence. *medRxiv*, 2021.
- [37] Peter Hirsch, Lisa Mais, and Dagmar Kainmueller. Patchperpix for instance segmentation. *arXiv preprint arXiv:2001.07626*, 2020.
- [38] Katrin Honauer, Lena Maier-Hein, and Daniel Kondermann. The hci stereo metrics: Geometry-aware performance analysis of stereo algorithms. In *Proceedings of the IEEE International Conference on Computer Vision*, pages 2120–2128, 2015.
- [39] Mohammad Hossin and Md Nasir Sulaiman. A review on evaluation metrics for data classification evaluations. *International journal of data mining & knowledge management process*, 5(2):1, 2015.
- [40] Daniel P Huttenlocher, Gregory A Klanderma, and William J Rucklidge. Comparing images using the hausdorff distance. *IEEE Transactions on pattern analysis and machine intelligence*, 15(9):850–863, 1993.
- [41] Paul Jaccard. The distribution of the flora in the alpine zone. 1. *New phytologist*, 11(2):37–50, 1912.
- [42] Paul F Jaeger, Simon AA Kohl, Sebastian Bickelhaupt, Fabian Isensee, Tristan Anselm Kuder, Heinz-Peter Schlemmer, and Klaus H Maier-Hein. Retina u-net: Embarrassingly simple exploitation of segmentation supervision for medical object detection. In *Machine Learning for Health Workshop*, pages 171–183. PMLR, 2020.
- [43] Paul Ferdinand Jäger. *Challenges and Opportunities of End-to-End Learning in Medical Image Classification*. PhD thesis, Karlsruhe Institut für Technologie (KIT), 2020.
- [44] Leo Joskowicz, D Cohen, N Caplan, and J Sosna. Inter-observer variability of manual contour delineation of structures in ct. *European radiology*, 29(3):1391–1399, 2019.
- [45] Jens N Kaftan, Atilla P Kiraly, Annemarie Bakai, Marco Das, Carol L Novak, and Til Aach. Fuzzy pulmonary vessel segmentation in contrast enhanced ct data. In *Medical Imaging 2008: Image Processing*, volume 6914, page 69141Q. International Society for Optics and Photonics, 2008.
- [46] Alexander Kirillov, Kaifeng He, Ross Girshick, Carsten Rother, and Piotr Dollár. Panoptic segmentation. In *Proceedings of the IEEE/CVF Conference on Computer Vision and Pattern Recognition*, pages 9404–9413, 2019.
- [47] A Kleppe. Area under the curve may hide poor generalisation to external datasets. *ESMO open*, 7(2), 2022.
- [48] Andreas Kleppe, Ole-Johan Skrede, Sepp De Raedt, Knut Liestøl, David J Kerr, and Håvard E Danielsen. Designing deep learning studies in cancer diagnostics. *Nature Reviews Cancer*, 21(3):199–211, 2021.
- [49] Florian Kofler, Ivan Ezhov, Fabian Isensee, Christoph Berger, Maximilian Korner, Johannes Paetzold, Hongwei Li, Suprosanna Shit, Richard McKinley, Spyridon Bakas, et al. Are we using appropriate segmentation metrics? Identifying correlates of human expert perception for CNN training beyond rolling the DICE coefficient. *arXiv preprint arXiv:2103.06205v1*, 2021.
- [50] Ender Konukoglu, Ben Glocker, Dong Hye Ye, Antonio Criminisi, and Kilian M Pohl. Discriminative segmentation-based evaluation through shape dissimilarity. *IEEE transactions on medical imaging*, 31(12):2278–2289, 2012.

- [51] Jonathan Krause, Varun Gulshan, Ehsan Rahimy, Peter Karth, Kasumi Widner, Greg S Corrado, Lily Peng, and Dale R Webster. Grader variability and the importance of reference standards for evaluating machine learning models for diabetic retinopathy. *Ophthalmology*, 125(8):1264–1272, 2018.
- [52] Harold W Kuhn. The hungarian method for the assignment problem. *Naval research logistics quarterly*, 2(1-2):83–97, 1955.
- [53] Victor Kulikov and Victor Lempitsky. Instance segmentation of biological images using harmonic embeddings. In *Proceedings of the IEEE/CVF Conference on Computer Vision and Pattern Recognition*, pages 3843–3851, 2020.
- [54] Tsung-Yi Lin, Michael Maire, Serge Belongie, James Hays, Pietro Perona, Deva Ramanan, Piotr Dollár, and C Lawrence Zitnick. Microsoft coco: Common objects in context. In *European conference on computer vision*, pages 740–755. Springer, 2014.
- [55] Hua Ma, Andriy I Bandos, Howard E Rockette, and David Gur. On use of partial area under the roc curve for evaluation of diagnostic performance. *Statistics in medicine*, 32(20):3449–3458, 2013.
- [56] Lena Maier-Hein, Matthias Eisenmann, Annika Reinke, Sinan Onogur, Marko Stankovic, Patrick Scholz, Tal Arbel, Hrvoje Bogunovic, Andrew P Bradley, Aaron Carass, et al. Why rankings of biomedical image analysis competitions should be interpreted with care. *Nature communications*, 9(1):1–13, 2018.
- [57] Lena Maier-Hein, Annika Reinke, Evangelia Christodoulou, Ben Glocker, Patrick Godau, Fabian Isensee, Jens Kleesiek, Michal Kozubek, Mauricio Reyes, Michael A Riegler, et al. Metrics reloaded: Pitfalls and recommendations for image analysis validation. *arXiv preprint arXiv:2206.01653*, 2022.
- [58] Ran Margolin, Lihi Zelnik-Manor, and Ayellet Tal. How to evaluate foreground maps? In *Proceedings of the IEEE conference on computer vision and pattern recognition*, pages 248–255, 2014.
- [59] Pavel Matula, Martin Maška, Dmitry V Sorokin, Petr Matula, Carlos Ortiz-de Solórzano, and Michal Kozubek. Cell tracking accuracy measurement based on comparison of acyclic oriented graphs. *PLoS one*, 10(12):e0144959, 2015.
- [60] Bjoern H Menze, Andras Jakab, Stefan Bauer, Jayashree Kalpathy-Cramer, Keyvan Farahani, Justin Kirby, Yuliya Burren, Nicole Porz, Johannes Slotboom, Roland Wiest, et al. The multimodal brain tumor image segmentation benchmark (brats). *IEEE transactions on medical imaging*, 34(10):1993–2024, 2014.
- [61] Pawel Mlynarski, Hervé Delingette, Hamza Alghamdi, Pierre-Yves Bondiau, and Nicholas Ayache. Anatomically consistent cnn-based segmentation of organs-at-risk in cranial radiotherapy. *Journal of Medical Imaging*, 7(1):014502, 2020.
- [62] Annette M Molinaro. Diagnostic tests: how to estimate the positive predictive value. *Neuro-Oncology Practice*, 2(4):162–166, 2015.
- [63] Mahdi Pakdaman Naeini, Gregory Cooper, and Milos Hauskrecht. Obtaining well calibrated probabilities using bayesian binning. In *Twenty-Ninth AAAI Conference on Artificial Intelligence*, 2015.
- [64] Ying-Hwey Nai, Bernice W Teo, Nadya L Tan, Sophie O’Doherty, Mary C Stephenson, Yee Liang Thian, Edmund Chiong, and Anthonin Reilhac. Comparison of metrics for the evaluation of medical segmentations using prostate mri dataset. *Computers in Biology and Medicine*, 134:104497, 2021.
- [65] Tanya Nair. *Exploring uncertainty measures in deep networks for multiple sclerosis lesion detection and segmentation*. PhD thesis, McGill University, 2018.
- [66] Nudrat Nida, Aun Irtaza, Ali Javed, Muhammad Haroon Yousaf, and Muhammad Tariq Mahmood. Melanoma lesion detection and segmentation using deep region based convolutional neural network and fuzzy c-means clustering. *International journal of medical informatics*, 124:37–48, 2019.
- [67] Stanislav Nikolov, Sam Blackwell, Alexei Zverovitch, Ruheena Mendes, Michelle Livne, Jeffrey De Fauw, Yojan Patel, Clemens Meyer, Harry Askham, Bernadino Romera-Paredes, et al. Clinically applicable segmentation of head and neck anatomy for radiotherapy: deep learning algorithm development and validation study. *Journal of Medical Internet Research*, 23(7):e26151, 2021.
- [68] Kemal Oksuz, Baris Can Cam, Emre Akbas, and Sinan Kalkan. Localization recall precision (lrp): A new performance metric for object detection. In *Proceedings of the European Conference on Computer Vision (ECCV)*, pages 504–519, 2018.
- [69] Hung Viet Pham, Shangshu Qian, Jiannan Wang, Thibaud Lutellier, Jonathan Rosenthal, Lin Tan, Yaoliang Yu, and Nachiappan Nagappan. Problems and opportunities in training deep learning software systems: An analysis of variance. In *Proceedings of the 35th IEEE/ACM international conference on automated software engineering*, pages 771–783, 2020.
- [70] David MW Powers. Evaluation: from precision, recall and f-measure to roc, informedness, markedness and correlation. *arXiv preprint arXiv:2010.16061*, 2020.
- [71] Annika Reinke, Matthias Eisenmann, Sinan Onogur, Marko Stankovic, Patrick Scholz, Peter M Full, Hrvoje Bogunovic, Bennett A Landman, Oskar Maier, Bjoern Menze, et al. How to exploit weaknesses in biomedical challenge design and organization. In *International Conference on Medical Image Computing and Computer-Assisted Intervention*, pages 388–395. Springer, 2018.
- [72] Azriel Rosenfeld and John L Pfaltz. Sequential operations in digital picture processing. *Journal of the ACM (JACM)*, 13(4):471–494, 1966.

- [73] Tobias Roß, Annika Reinke, Peter M Full, Martin Wagner, Hannes Kenngott, Martin Apitz, Hellena Hempe, Diana Mindroc-Filimon, Patrick Scholz, Thuy Nuong Tran, et al. Comparative validation of multi-instance instrument segmentation in endoscopy: results of the robust-mis 2019 challenge. *Medical image analysis*, 70:101920, 2021.
- [74] Anindo Saha, Joeran Bosma, Jasper Linmans, Matin Hosseinzadeh, and Henkjan Huisman. Anatomical and diagnostic bayesian segmentation in prostate mri – should different clinical objectives mandate different loss functions? *arXiv preprint arXiv:2110.12889*, 2021.
- [75] Suprosanna Shit, Johannes C Paetzold, Anjany Sekuboyina, Ivan Ezhov, Alexander Unger, Andrey Zhyhka, Josien PW Pluim, Ulrich Bauer, and Bjoern H Menze. cldice-a novel topology-preserving loss function for tubular structure segmentation. In *Proceedings of the IEEE/CVF Conference on Computer Vision and Pattern Recognition*, pages 16560–16569, 2021.
- [76] Jacob Shreffler and Martin R Huecker. Diagnostic testing accuracy: Sensitivity, specificity, predictive values and likelihood ratios. 2020.
- [77] Ana-Maria Šimundić. Measures of diagnostic accuracy: basic definitions. *ejifcc*, 19(4):203, 2009.
- [78] Ewout W Steyerberg, Andrew J Vickers, Nancy R Cook, Thomas Gerds, Mithat Gonen, Nancy Obuchowski, Michael J Pencina, and Michael W Kattan. Assessing the performance of prediction models: a framework for some traditional and novel measures. *Epidemiology (Cambridge, Mass.)*, 21(1):128, 2010.
- [79] Carole H Sudre, Wenqi Li, Tom Vercauteren, Sebastien Ourselin, and M Jorge Cardoso. Generalised dice overlap as a deep learning loss function for highly unbalanced segmentations. In *Deep learning in medical image analysis and multimodal learning for clinical decision support*, pages 240–248. Springer, 2017.
- [80] Yanmin Sun, Andrew K. C. Wong, and Mohamed S. Kamel. Classification of imbalanced data: a review. *Int. J. Pattern Recognit. Artif. Intell.*, 23:687–719, 2009.
- [81] Abdel Aziz Taha and Allan Hanbury. Metrics for evaluating 3d medical image segmentation: analysis, selection, and tool. *BMC medical imaging*, 15(1):1–28, 2015.
- [82] Abdel Aziz Taha, Allan Hanbury, and Oscar A Jimenez del Toro. A formal method for selecting evaluation metrics for image segmentation. In *2014 IEEE international conference on image processing (ICIP)*, pages 932–936. IEEE, 2014.
- [83] Uchila N Umesh, Robert A Peterson, and Matthew H Sauber. Interjudge agreement and the maximum value of kappa. *Educational and Psychological Measurement*, 49(4):835–850, 1989.
- [84] Femke Vaassen, Colien Hazelaar, Ana Vaniqui, Mark Goding, Brent van der Heyden, Richard Canters, and Wouter van Elmpt. Evaluation of measures for assessing time-saving of automatic organ-at-risk segmentation in radiotherapy. *Physics and Imaging in Radiation Oncology*, 13:1–6, 2020.
- [85] Juozas Vaicenavicius, David Widmann, Carl Andersson, Fredrik Lindsten, Jacob Roll, and Thomas Schön. Evaluating model calibration in classification. In *The 22nd International Conference on Artificial Intelligence and Statistics*, pages 3459–3467. PMLR, 2019.
- [86] Bram Van Ginneken, Tobias Heimann, and Martin Styner. 3d segmentation in the clinic: A grand challenge. In *MICCAI Workshop on 3D Segmentation in the Clinic: A Grand Challenge*, volume 1, pages 7–15, 2007.
- [87] Bram Van Ginneken, Samuel G Armato III, Bartjan de Hoop, Saskia van Amelsvoort-van de Vorst, Thomas Duindam, Meindert Niemeijer, Keelin Murphy, Arnold Schilham, Alessandra Retico, Maria Evelina Fantacci, et al. Comparing and combining algorithms for computer-aided detection of pulmonary nodules in computed tomography scans: the anode09 study. *Medical image analysis*, 14(6):707–722, 2010.
- [88] Andrew J Vickers, Ben Van Calster, and Ewout W Steyerberg. Net benefit approaches to the evaluation of prediction models, molecular markers, and diagnostic tests. *bmj*, 352, 2016.
- [89] Pauli Virtanen, Ralf Gommers, Travis E Oliphant, Matt Haberland, Tyler Reddy, David Cournapeau, Evgeni Burovski, Pearu Peterson, Warren Weckesser, Jonathan Bright, et al. Scipy 1.0: fundamental algorithms for scientific computing in python. *Nature methods*, 17(3):261–272, 2020.
- [90] NJ Wald and JP Bestwick. Is the area under an roc curve a valid measure of the performance of a screening or diagnostic test? *Journal of medical screening*, 21(1):51–56, 2014.
- [91] Manuel Wiesenfarth, Annika Reinke, Bennett A Landman, Matthias Eisenmann, Laura Aguilera Saiz, M Jorge Cardoso, Lena Maier-Hein, and Annette Kopp-Schneider. Methods and open-source toolkit for analyzing and visualizing challenge results. *Scientific Reports*, 11(1):1–15, 2021.
- [92] Varduhi Yeghiazaryan and Irina D Voiculescu. Family of boundary overlap metrics for the evaluation of medical image segmentation. *Journal of Medical Imaging*, 5(1):015006, 2018.
- [93] Aston Zhang, Zachary C Lipton, Mu Li, and Alexander J Smola. Dive into deep learning. *arXiv preprint arXiv:2106.11342*, 2021.

APPENDIX**A ACRONYMS**

AI artificial intelligence
AP Average Precision
ASSD Average Symmetric Surface Distance
AUC Area under the curve
AUROC Area under the Receiver Operating Characteristic curve
BA Balanced Accuracy
BM Bookmaker Informedness
BS Brier Score
CE Calibration Error
cDice Centerline Dice Similarity Coefficient
CI Confidence Interval
COCO Common Objects in Context
DSC Dice Similarity Coefficient
EC Expected Cost
ECE Expected Calibration Error
FN False Negative
FP False Positive
FPPI False Positives per Image
FPR False Positive Rate
FROC Free-Response Receiver Operating Characteristic
GPU Graphics Processing Unit
HD Hausdorff Distance
HD95 Hausdorff Distance 95% Percentile
IoU Intersection over Union
IoR Intersection over Reference
LR+ Positive Likelihood Ratio
mAP mean Average Precision
MASD Mean Average Surface Distance
MCC Matthews Correlation Coefficient
MCE Maximum Calibration Error
NaN Not A Number
NB Net Benefit
NPV Negative Predictive Value
NSD Normalized Surface Distance
PPV Positive Predictive Value
PR Precision-Recall
PQ Panoptic Quality
ROC Receiver Operating Characteristic
TN True Negative
TNR True Negative Rate
TP True Positive
TPR True Positive Rate